

Università degli studi di Padova
Dipartimento di Fisica e Astronomia

Tesi di Dottorato

Search for heavy resonances decaying into a Z boson and a vector boson in the $\nu\bar{\nu} q\bar{q}$ final state at CMS

Supervisor: Prof. Franco Simonetto
Candidate: Lisa Benato

Scuola di Dottorato di Ricerca, XXX ciclo

"I have no special talent. I am only passionately curious."

(A. Einstein)

Contents

1	Introduction	1
2	Theoretical motivation	3
2.1	Beyond Standard Model theories	3
2.2	Heavy Vector Triplet	5
2.2.1	Simplified Lagrangian	5
2.2.2	Mass eigenstates, mixing parameters and decay widths	6
2.2.2.1	Decay widths into fermions	8
2.2.2.2	Decay widths into bosons	8
2.2.2.3	Decays in fermions and bosons: concluding remarks	9
2.2.3	HVT production	9
2.2.4	Benchmark model A: weak coupling scenario	11
2.2.5	Benchmark model B: strong coupling scenario	12
2.2.6	Search for HVT resonances at LHC	12
2.3	Warped extra dimension	16
2.3.1	Randall-Sundrum original model (RS1)	16
2.3.2	Bulk extension of RS1: graviton production and decays	19
2.3.3	Search for KK bulk gravitons at LHC	22
3	The Large Hadron Collider and the CMS experiment	25
3.1	The Large Hadron Collider	25
3.1.1	Proton-proton interactions	27
3.2	CMS detector	29
3.2.1	The coordinate system	30
3.2.2	The magnet	31
3.2.3	The tracking system	32
3.2.3.1	The pixel detector	33
3.2.3.2	The strip detector	33
3.2.4	The electromagnetic calorimeter	33
3.2.5	The hadronic calorimeter	34
3.2.6	The muon system	35
3.2.6.1	The Drift Tubes	35
3.2.6.2	The Cathode Strip Chambers	36

3.2.6.3	The Resistive Plate Chambers	36
3.2.7	The trigger system and data acquisition	37
3.2.7.1	The Level-1 trigger	37
3.2.7.2	The High Level Trigger	37
3.2.7.3	Data acquisition, computing and storage	37
3.2.8	Particle Flow event reconstruction	38
3.2.9	Physics objects	38
3.2.9.1	Track reconstruction	38
3.2.9.2	Vertices reconstruction	39
3.2.9.3	Electrons and photons reconstruction	39
3.2.9.4	Muon reconstruction	40
3.2.9.5	Jet reconstruction	40
3.2.9.6	Tau reconstruction	42
3.2.9.7	b-jets tagging	43
3.2.9.8	Missing transverse energy reconstruction	45
3.3	ATLAS, ALICE, LHCb detectors	48
3.3.1	ATLAS	48
3.3.2	ALICE	49
3.3.3	LHCb	49
4	Search for diboson resonances in the $ZV \rightarrow \nu\bar{\nu}q\bar{q}$ final state	51
4.1	Data and Monte Carlo samples	52
4.2	Event selection	53
4.2.1	Vertex and Pile-up	53
4.2.2	Electrons	53
4.2.3	Muons	54
4.2.4	Taus	55
4.2.5	Photons	56
4.2.6	Jets	57
4.2.7	Jet mass	59
4.2.8	Jet substructure	60
4.2.9	b-tagging	60
4.2.10	Missing Energy	61
4.3	Diboson candidate reconstruction	63
4.4	Background estimation	64
4.5	Systematic uncertainties	65
4.6	Results	66
5	Combination of diboson searches in semileptonic final states	67
6	Conclusions	69

1

Abstract

2

3

CONTENTS

Introduction

7 This analysis searches for signal of heavy resonances decaying into a pair of heavy vector bosons.
8 One Z boson is identified through its invisible decay ($\nu\nu$), while the other is required to decay hadron-
9 ically into a pair of quarks. The final states probed by this analysis therefore consists in two quarks
10 and two neutrinos, reconstructed as missing transverse energy (met). The hadronically decaying
11 boson (Z, W) is reconstructed as a fat jet, whose mass is used to define the signal region. Two purity
12 categories are exploited, based on the n-subjettiness of the fat jet.

13 The search is performed by examining the distribution of the diboson reconstructed transverse
14 mass of the resonance VZ (mtVZ) for a localized excess. The shape and normalization of the main
15 background of the analysis (V+jets) are estimated with an hybrid approach using the distribution
16 of data in the sidebands, corrected for a function accounting for potential differences between the
17 signal region and the sidebands, while the minor background sources are taken from simulations.

Theoretical motivation

21 The standard model (SM) of particles represents, so far, the best available description of the parti-
 22 cles and their interactions. It is the summation of two gauge theories: the electroweak interaction,
 23 that portrays the weak and electromagnetic interactions together, and the strong interaction, or
 24 Quantum Chromodynamics (QCD). Particles, namely quarks and leptons, are described as spin 1/2
 25 fermions, whilst interactions are represented by spin 1 bosons. The symmetry group of the standard
 26 model is:

$$SU_C(3) \times SU_L(2) \times U_Y(1), \quad (2.1)$$

27 where the first factor is related to strong interactions, whose mediators are eight gluons, while
 28 $SU_L(2) \times U_Y(1)$ is the electroweak symmetry group, whose mediators are photons and Z - W^\pm bosons.
 29 In renormalizable theories, with no anomalies, all gauge bosons are expected to be massless, in con-
 30 trast with our experimental knowledge. This inconsistency is solved by introducing a new scalar
 31 particle, the Higgs boson, that can give mass to weak bosons and fermions via the spontaneous
 32 symmetry breaking mechanism.

33
 34 In the last decades, Standard Model has been accurately probed by many experimental facilities
 35 (LEP, Tevatron, LHC), and the results lead to an impressive agreement between theoretical pre-
 36 dictions and experiments. The discovery of the Higgs boson at the CERN Large Hadron Collider,
 37 measured by both CMS and ATLAS collaborations [1–7], represents not only an extraordinary con-
 38 firmation of the model, but also the latest biggest achievement in particle physics as a whole.

39 2.1 Beyond Standard Model theories

- 40 Even though the Standard Model is the most complete picture of the universe of the particles, many
 41 questions are still left open. From a phenomenological point of view, some experimental observa-
 42 tions are not included in the theory:
- 43 • in SM, neutrinos are massless (whilst experimentally their masses are confirmed to be non-
 44 zero, i.e. by the neutrino oscillations);
 - 45 • no candidates for dark matter are predicted;
 - 46 • no one of the fields included in the SM can explain the cosmological inflation;

- 47 • SM can not justify the matter-antimatter asymmetry.
- 48 From a purely theoretical perspective, some issues are still relevant in the formulation of the model:
- 49 • *Flavour problem.*
- 50 The Standard Model has 18 free parameters: 9 fermionic masses; 3 angular parameters in
51 Cabibbo-Kobayashi-Maskawa matrix, plus 1 phase parameter; electromagnetic coupling α ;
52 strong coupling α_{strong} ; weak coupling α_{weak} ; Z mass; the mass of the Higgs boson. Such a
53 huge number of degrees of freedom marks the SM as weakly predictive in the flavour sector.
- 54 • *Unification.*
- 55 There is not a “complete” unification of strong, weak and electromagnetic interactions, since
56 each one has its own coupling constant, behaving differently at different energy scales; not to
57 mention the fact that gravitational interaction is completely excluded from the SM.
- 58 • *Hierarchy problem.*
- 59 From Quantum Field Theory, it is known that perturbative corrections to the mass of the scalar
60 bosons included in the theory tend to make it increase towards the energy scale at which the
61 considered theory still holds [8]. If the Standard Model is seen as a low-mass approximation of
62 a more general theory valid up to the Planck mass scale (*i.e.*, $\sim 1.2 \times 10^{19}$ GeV), a fine-tuning
63 cancellation of the order of 1 over 10^{34} is needed in order to protect the Higgs mass at the
64 electroweak scale (~ 100 GeV). Such an astonishing correction is perceived as very unnatural.
- 65 Numerous Beyond Standard Model theories (BSM) have been proposed in order to overcome
66 the limits of the Standard Model.
- 67 Grand Unified Theories (GUT) aim at extending the symmetry group of the SM (eq. 2) into largest
68 candidates, such as $SO(10)$, $SU(5)$ and $E(6)$. At GUT scale, approximately at 10^{16} GeV, non-gravitational
69 interactions are expected to be ruled by only one coupling constant, α_{GUT} .
- 70 Super Symmetry (SUSY) models state that every fermion (boson) of the Standard Model has a
71 bosonic (fermionic) superpartner, with exactly the same quantum numbers, except the spin. If
72 SUSY is not broken, each couple of partners and superpartners should have the same masses, hy-
73 pothesis excluded by the non-observation of the s-electron. Super Symmetry represents a very ele-
74 gant solution of the hierarchy problem of the Higgs boson mass, since the perturbative corrections
75 brought by new SUSY particles exactly cancel out the divergences caused by SM particles correc-
76 tions. A particular sub-class of SUSY models, Minimal Super Symmetric Standard Models, is char-
77 acterized by the introduction of a new symmetry, the R-parity, that guarantees the proton stability
78 and also the stability of the lightest SUSY particle, a possible good candidate for dark matter.
- 79
- 80 Two other possible theoretical pictures are extensively described in sec. 2.2-2.3.

2.2 Heavy Vector Triplet

81 2.2 Heavy Vector Triplet

82 The heavy vector triplet model [9] provides a general framework aimed at studying new physics be-
83 yond the standard model, that can manifest into the appearance of new resonances.
84 The adopted approach is that of the simplified model, in which an effective Lagrangian is intro-
85 duced, in order to describe the properties and interactions of new particles (in this case, a triplet of
86 spin-1 bosons) by using a limited set of parameters, that can be easily linked to the physical observ-
87 ables at the LHC experiments. These parameters can describe many physical motivated theories
88 (such as sequential extensions of the SM [10, 11] or Composite Higgs [12, 13]).
89 Since a simplified model is not a complete theory, its validity is restricted to the on-shell quanti-
90 ties related to the production and decay mechanisms of the new resonances, that is how most of
91 the LHC BSM searches are performed. Given these conditions, experimental results in the resonant
92 region are sensitive to a limited number of the phenomenological Lagrangian parameters (or to a
93 combination of those), whilst the remaining parameters tend to influence the tail of the distribu-
94 tions.
95 Limits on production cross-section times branching ratio ($\sigma \mathcal{B}$), as a function of the invariant mass
96 spectrum of the probed resonance, can be extracted from experimental data. Given that $\sigma \mathcal{B}$ are
97 functions of the simplified model parameters and of the parton luminosities, it is then possible to
98 interpret the observed limits in the parameter space.

99 2.2.1 Simplified Lagrangian

100 The heavy vector triplet framework assumes the existence of an additional vector triplet, V_μ^a , $a =$
101 1, 2, 3, in which two spin-1 particles are charged and one is neutral:

$$V_\mu^\pm = \frac{V_\mu^1 \mp i V_\mu^2}{\sqrt{2}}; \quad (2.2)$$
$$V_\mu^0 = V_\mu^3.$$

102
103 The triplet interactions are described by a simplified Lagrangian, that is invariant under SM gauge
104 and CP symmetry, and accidentally invariant under the custodial symmetry $SU(2)_L \times SU(2)_R$:

$$\begin{aligned} \mathcal{L}_V = & -\frac{1}{4} (D_\mu V_\nu^a - D_\nu V_\mu^a) (D^\mu V^\nu{}^a - D^\nu V^\mu{}^a) + \frac{m_V^2}{2} V_\mu^a V^\mu{}^a \\ & + i g_V c_H V_\mu^a (H^\dagger \tau^a D^\mu H - D^\mu H^\dagger \tau^a H) + \frac{g^2}{g_V} c_F V_\mu^a \sum_f \bar{f}_L \gamma^\mu \tau^a f_L \\ & + \frac{g_V}{2} c_{VVV} \epsilon_{abc} V_\mu^a V_\nu^b (D^\mu V^\nu{}^c - D^\nu V^\mu{}^c) + g_V^2 c_{VHH} V_\mu^a V^\mu{}^a H^\dagger H - \frac{g}{2} c_{VWW} \epsilon_{abc} W^{\mu\nu}{}^a V_\mu^b V_\nu^c. \end{aligned} \quad (2.3)$$

105
106 In the first line of the formula 2.3, V mass and kinematic terms are included, described with the co-
107 variant derivative $D_\mu V_\nu^a = \partial_\mu V_\nu^a + g \epsilon^{abc} W_\mu^b V_\nu^c$, where W_μ^a are the fields of the weak interaction and
108 g is the weak gauge coupling. V_μ^a are not mass eigenstates, since they mix with the electroweak fields
109 after the spontaneous symmetry breaking, therefore m_V isn't the physical mass of the V bosons.
110 The second line describes the interaction of the triplet with the Higgs field and the SM left-handed
111 fermions; c_H describes the vertices with the physical Higgs and the three unphysical Goldstone
112 bosons that, for the Goldstone equivalence theorem, are equivalent to the longitudinal polarization
113 of W and Z bosons at high-energy; hence, c_H is related to the bosonic decays of the resonances. c_F

114 is the analogous parameter describing the V interaction with fermions, that can be generalized as a
 115 flavour dependent coefficient, once defined $J_F^{\mu a} = \sum_f \bar{f}_L \gamma^\mu \tau^a f_L$: $c_F V_\mu^a J_F^{\mu a} = c_\ell V_\mu^a J_\ell^{\mu a} + c_q V_\mu^a J_q^{\mu a} +$
 116 $c_3 V_\mu^a J_3^{\mu a}$.

117 The last part of the equation includes terms that are relevant only in strongly coupled scenarios (see
 118 sec. 2.2.2.2) through the V - W mixing, but it does not include vertices of V with light SM fields, hence
 119 it can be neglected while describing the majority of the LHC phenomenology, under the assump-
 120 tions previously stated. Additional dimension four quadrilinear V interactions are non relevant for
 121 the processes discussed, otherwise their effects would be appreciated in electroweak precision tests
 122 and precise Higgs coupling measurements [14].

123
 124 The parameters in the Lagrangian can be interpreted as follows: g_V describes the strength of
 125 the interaction, that is weighted by c parameters. g_V ranges from $g_V \sim 1$ when the coupling is
 126 weak (sec. 2.2.4), to $g_V \sim 4\pi$ when the coupling is strong (sec. 2.2.5). c parameters are expected
 127 to be $c \sim 1$, except to c_H , that can be smaller for weak couplings. The combinations describing the
 128 vertices, $g_V c_H$ and $g^2/g_V c_F$, can be considered as the fundamental parameters, used to interpret
 129 the experimental results.

130 2.2.2 Mass eigenstates, mixing parameters and decay widths

131 The newly introduced $SU(2)_L$ triplet is expected to mix with the weak SM fields. The $U(1)_{em}$ sym-
 132 metry is left unbroken by the new interaction, hence the massless combination of the electroweak
 133 fields, namely the photon, is the same as the SM:

$$A_\mu = B_\mu \cos \theta_W + W_\mu^3 \sin \theta_W, \quad (2.4)$$

134 with the usual definitions of the electroweak parameters:

$$\begin{aligned} \tan \theta_W &= \frac{g'}{g} \\ e &= \frac{gg'}{\sqrt{g^2 + g'^2}} \\ g &= e / \sin \theta_w \\ g' &= e / \cos \theta_w. \end{aligned} \quad (2.5)$$

135 The Z boson, on the other hand, mixes with the neutral component of the triplet, V^0 , with a
 136 rotation parametrized with the angle θ_N :

$$\begin{pmatrix} \cos \theta_N & \sin \theta_N \\ -\sin \theta_N & \cos \theta_N d \end{pmatrix} \begin{pmatrix} Z \\ V^0 \end{pmatrix}. \quad (2.6)$$

137 The mass matrix of the rotated system is given by:

$$\mathbb{M}_N^2 = \begin{pmatrix} \hat{m}_Z^2 & c_H \zeta \hat{m}_Z \hat{m}_V \\ c_H \zeta \hat{m}_Z \hat{m}_V & \hat{m}_V^2 \end{pmatrix}, \quad (2.7)$$

138 where the parameters are defined as:

$$\left\{ \begin{array}{l} \hat{m}_Z = \frac{e}{2 \sin \theta_W \cos \theta_W} \hat{v} \\ \hat{m}_V^2 = m_V^2 + g_V^2 c_{VVHH} \hat{v}^2 \\ \zeta = \frac{g_V \hat{v}}{2 \hat{m}_V} \\ \frac{\hat{v}^2}{2} = \langle H^\dagger H \rangle \end{array} \right., \quad (2.8)$$

2.2 Heavy Vector Triplet

- ¹³⁹ and \hat{v} , the vacuum expectation value of the Higgs field, can be different from the SM $v = 246$ GeV.
¹⁴⁰ The physical masses of Z and V^0 , m_Z and M_0 , and θ_N come from the matrix relations:

$$\begin{aligned}\text{Tr}(\mathbb{M}_N^2) &= \hat{m}_Z^2 + \hat{m}_V^2 = m_Z^2 + M_0^2 \\ \|\mathbb{M}_N^2\| &= \hat{m}_Z^2 + \hat{m}_V^2 (1 - c_H^2 \zeta^2) = m_Z^2 M_0^2 \\ \tan 2\theta_N &= \frac{2c_H \zeta \hat{m}_Z \hat{m}_V}{\hat{m}_V^2 - \hat{m}_Z^2}.\end{aligned}\quad (2.9)$$

- ¹⁴¹ The W^\pm bosons mix with the charged components of the triplet, V^\pm , leading to a mass matrix
¹⁴² analogous to eq. 2.10:

$$\mathbb{M}_C^2 = \begin{pmatrix} \hat{m}_W^2 & c_H \zeta \hat{m}_W \hat{m}_V \\ c_H \zeta \hat{m}_W \hat{m}_V & \hat{m}_V^2 \end{pmatrix}, \quad (2.10)$$

- ¹⁴³ where \hat{m}_W is defined as:

$$\left\{ \begin{array}{l} \hat{m}_W = \frac{e}{2 \sin \theta_W} \hat{v} = \hat{m}_Z \cos \theta_W \\ \end{array} \right. ; \quad (2.11)$$

- ¹⁴⁴ the physical masses of W and V^\pm , m_W and M_\pm , and the angle θ_C parametrizing the rotation of the
¹⁴⁵ charged sector are described by:

$$\begin{aligned}\text{Tr}(\mathbb{M}_C^2) &= \hat{m}_W^2 + \hat{m}_V^2 = m_W^2 + M_\pm^2 \\ \|\mathbb{M}_C^2\| &= \hat{m}_W^2 + \hat{m}_V^2 (1 - c_H^2 \zeta^2) = m_W^2 M_\pm^2 \\ \tan 2\theta_C &= \frac{2c_H \zeta \hat{m}_W \hat{m}_V}{\hat{m}_V^2 - \hat{m}_W^2}.\end{aligned}\quad (2.12)$$

- ¹⁴⁶ The custodial symmetry of eq. 2.3 guarantees that:

$$\mathbb{M}_C^2 = \begin{pmatrix} \cos \theta_W & 0 \\ 0 & 1 \end{pmatrix} \mathbb{M}_N^2 \begin{pmatrix} \cos \theta_W & 0 \\ 0 & 1 \end{pmatrix}. \quad (2.13)$$

- ¹⁴⁷
- ¹⁴⁸ By taking the determinant of these matrices, a custodial relation among the masses can be extracted:
¹⁴⁹

$$m_W^2 M_\pm^2 = \cos \theta_W m_Z^2 M_0^2, \quad (2.14)$$

- ¹⁵⁰ that has some very important consequences.
¹⁵¹ Given that this model aims at searching new particles in the TeV scale and that the scale of the elec-
¹⁵² troweak interactions must lay at ~ 100 GeV, a hierarchy of the physical masses seems very natural:
¹⁵³

$$\frac{\hat{m}_{(W,Z)}}{\hat{m}_V} \sim \frac{m_{(W,Z)}}{M_{(\pm,0)}} \ll 1; \quad (2.15)$$

- ¹⁵⁴ ζ parameter can be $\zeta \ll 1$ (weakly coupled scenario) or $\zeta \sim 1$ (strongly coupled scenario). When
¹⁵⁵ eq. 2.15 applies, the second lines in eq. 2.9 and eq. 2.12 can be approximated as follows:

$$\begin{aligned}m_Z^2 &= \hat{m}_Z^2 (1 - c_H^2 \zeta^2) (1 + \mathcal{O}(\hat{m}_Z^2 / \hat{m}_V^2)) \\ m_W^2 &= \hat{m}_W^2 (1 - c_H^2 \zeta^2) (1 + \mathcal{O}(\hat{m}_W^2 / \hat{m}_V^2)).\end{aligned}\quad (2.16)$$

- ¹⁵⁶
- ¹⁵⁷ From eq. 2.11, the ratio of the physical masses of the charged and neutral electroweak bosons can
¹⁵⁸ be approximated as:

$$\frac{m_W^2}{m_Z^2} \approx \cos \theta_W^2, \quad (2.17)$$

159 that satisfies the SM tree-level relation $\rho = 1$ if $\cos \theta_W^2 \approx 1. - 0.23$. Adding this approximation into
 160 eq. 2.14, the V bosons are expected to have the same masses, hence the same production rates:

$$M_{\pm}^2 = M_0^2 (1 + \mathcal{O}(\%)). \quad (2.18)$$

161 The degenerate mass of the triplet will be called $M_V \approx M_{\pm} \approx M_0$; given 2.15, $M_V = \hat{m}_V$.
 162 Another consequence of the mass hierarchy (2.15) is that the mixing angles $\theta_{(N,C)}$ between the elec-
 163 troweak fields and the triplet are small:

$$\theta_{(N,C)} \approx c_H \zeta \frac{\hat{m}_{(W,Z)}}{\hat{m}_V} \ll 1, \quad (2.19)$$

164 hence the couplings among SM particles are very close to the couplings predicted by the SM.

165 2.2.2.1 Decay widths into fermions

166 The couplings among the triplet and SM fermions are expressed as a function of the rotation angles
 167 $\theta_{(C,N)}$ and SM couplings (omitting the CKM matrix elements for quarks):

$$\begin{cases} g_L^N = \frac{g^2}{g_V} \frac{c_F}{2} \cos \theta_N + (g_L^Z)_{SM} \sin \theta_N \approx \frac{g^2}{g_V} \frac{c_F}{2}, \\ g_R^N = (g_R^Z)_{SM} \sin \theta_N \approx 0 \end{cases},$$

$$\begin{cases} g_L^C = \frac{g^2}{g_V} \frac{c_F}{2} \cos \theta_C + (g_L^W)_{SM} \sin \theta_N \approx \frac{g^2}{g_V} \frac{c_F}{2}, \\ g_R^C = 0 \end{cases}, \quad (2.20)$$

168 where $g_L^W = g/\sqrt{2}$; $g_{L,R}^{W,Z}$ are those predicted by the standard model. The V bosons interact with SM
 169 left fermions, and the strength of the couplings with fermions is determined by $g^2/g_V c_F$, as stated
 170 in sec. 2.2.1. The decay width into fermions is then given by:

$$\Gamma_{V^{\pm} \rightarrow f \bar{f}} \approx 2\Gamma_{V^0 \rightarrow f \bar{f}} \approx N_c \left(\frac{g^2 c_F}{g_V} \right)^2 \frac{M_V}{48\pi}, \quad (2.21)$$

171 where N_c is the number of colours (3 for quarks, 1 for leptons).

172 2.2.2.2 Decay widths into bosons

173 As a starting point, a proper choice of the gauge makes the derivation of the approximate decay
 174 widths easier. While the unitary gauge is very convenient in discussing the electroweak symmetry
 175 breaking mechanism, since it provides a basis in which the Goldstone components of the scalar
 176 fields of the theory are set to zero, it does not properly describe the longitudinally polarized bosons
 177 in high-energy regimes, since it introduces a dependence of the type E/m in the longitudinal po-
 178 larization vector, not corresponding to the experimental results. This pathological behaviour can
 179 be overcome profiting of the equivalence theorem: while calculating the scattering amplitude of
 180 an high-energy process, the longitudinally polarized vectors are equivalent to their corresponding
 181 Goldstone scalars. The scattering amplitude can therefore be calculated with Goldstone diagrams.
 182 In the so-called equivalent gauge [15], the Higgs doublet is then parametrized as:

$$H = \begin{pmatrix} i\pi_+ \\ \frac{\hat{h} + h - i\pi_0}{\sqrt{2}} \end{pmatrix}, \quad (2.22)$$

2.2 Heavy Vector Triplet

and the Goldstones π_0 and π_+ describe respectively W and Z longitudinal bosons; h is the physical Higgs boson. Rewriting the simplified Lagrangian 2.3 with 2.22 parametrization, two terms hold the information of the interaction of the V s with the Goldstones:

$$\mathcal{L}_\pi = \dots + c_H \zeta \hat{m}_V V_\mu^a \partial^\mu \pi^a + \frac{g_V c_H}{2} V_\mu^a (\partial^\mu h \pi^a - h \partial^\mu \pi^a + \epsilon^{abc} \pi^b \partial^\mu \pi^c) + \dots, \quad (2.23)$$

that are ruled by the $c_H g_V$ parameters combination. When ζ parameter is $\zeta \approx 1$, the first term in eq. 2.23 becomes important, and it is absorbed by a redefinition of the V_μ^a and π^a fields,

$$\begin{aligned} V_\mu^a &\rightarrow V_\mu^a + \frac{c_H \zeta}{\hat{m}_V} \partial_\mu \pi^a \\ \pi^a &\rightarrow \frac{1}{\sqrt{1 - c_H^2 \zeta^2}} \pi^a; \quad c_H^2 \zeta^2 < 1 \end{aligned} \quad (2.24)$$

By properly taking into account all the terms of the simplified lagrangian in the equivalent gauge, the partial widths of the dibosonic decays are ($\hat{m}_V = M_V$):

$$\begin{aligned} \Gamma_{V^0 \rightarrow W_L^+ W_L^-} &\approx \Gamma_{V^\pm \rightarrow W_L^\pm Z_L} \approx \frac{g_V^2 c_H^2 M_V}{192\pi} \frac{(1 + c_H c_{VVV} \zeta^2)^2}{(1 - c_H^2 \zeta^2)^2} = \frac{g_V^2 c_H^2 M_V}{192\pi} (1 + \mathcal{O}(\zeta^2)) \\ \Gamma_{V^0 \rightarrow Z_L h} &\approx \Gamma_{V^\pm \rightarrow W_L^\pm h} \approx \frac{g_V^2 c_H^2 M_V}{192\pi} \frac{(1 - 4 c_H c_{VVV} \zeta^2)^2}{(1 - c_H^2 \zeta^2)^2} = \frac{g_V^2 c_H^2 M_V}{192\pi} (1 + \mathcal{O}(\zeta^2)). \end{aligned} \quad (2.25)$$

2.2.2.3 Decays in fermions and bosons: concluding remarks

From eq. 2.21-2.25, some important conclusions can be extracted.

- When ζ parameter is small, all the triplet decays (both in fermions and in dibosons), branching fractions and productions are completely determined by $g^2 c_F/g_V$, $g_V c_H$, and the degenerate mass of the triplet M_V ,
- c_{VVV} , c_{VVHH} , c_{VWW} can be neglected, as long as the interest is focused in narrow resonances.

2.2.3 HVT production

Given the mass scale of the resonances, the production mechanisms expected to be relevant are Drell-Yan (fig. 2.1) and Vector Boson Fusion (VBF) (fig. 2.2).

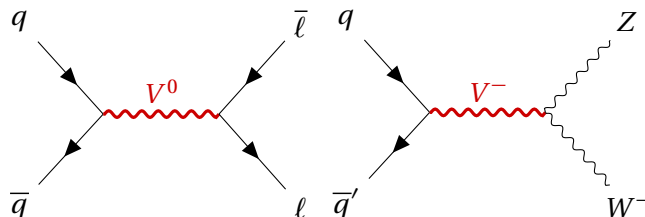


Figure 2.1: Examples of Drell-Yan production mechanism of a heavy V HVT boson: $q - \bar{q}$ quark scattering producing a neutral V^0 that decays leptonically (left); $q - \bar{q}'$ scattering producing a charged V^- that decays in a W and Z bosons (right).

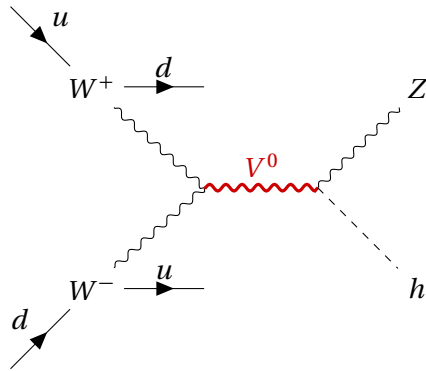


Figure 2.2: Example of VBF production mechanism of a heavy V HVT boson: a neutral V^0 boson is produced by a couple of W bosons, as a result of electroweak interactions of initial state u and d quarks. V^0 decays in a Z boson and a Higgs boson. The final state signature includes the presence of a pair of quarks, due to the primary interactions.

199 The cross-section of the production mechanisms is given by:

$$\sigma(pp \rightarrow V + X) = \sum_{i,j \in p} \frac{\Gamma_{V \rightarrow ij}}{M_V} f(J, S_i, S_j) g(C_i, C_j) \left. \frac{dL_{ij}}{ds} \right|_{s=M_V^2}, \quad (2.26)$$

200 where i, j are the partons involved in the hard interaction, Γ_{ij} is the partial width of the process
 201 $V \rightarrow ij$, $f(J, S_i, S_j)$ is a function of the spin of the resonance and of the partons, $g(C_i, C_j)$ is a func-
 202 tion of the colour factors of each parton, s is the center-of-mass energy and $\frac{dL_{ij}}{ds}$ are the parton
 203 luminosities, that are independent from HVT model (that enters only in Γ_{ij}).

204 Parton luminosities, calculated for a center-of-mass energy of 14 TeV starting from quark and anti-
 205 quark parton distribution functions (PDF), are displayed in fig. 2.3 (Drell-Yan mechanism) and 2.4
 206 (VBF mechanism). VBF luminosities are suppressed by the α_{EW} factor, therefore the process is rel-
 evant only when the bosonic decays of the triplet are dominant (strongly coupled scenario).

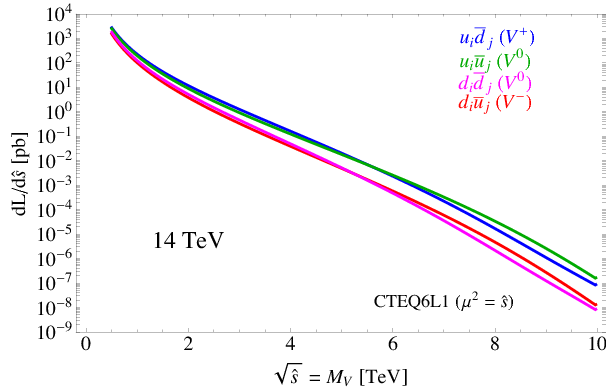


Figure 2.3: Parton luminosities for Drell-Yan process between i and j partons, as a function of the parton center-of-mass energy, for the LHC proton-proton collisions performed at 14 TeV.

2.2 Heavy Vector Triplet

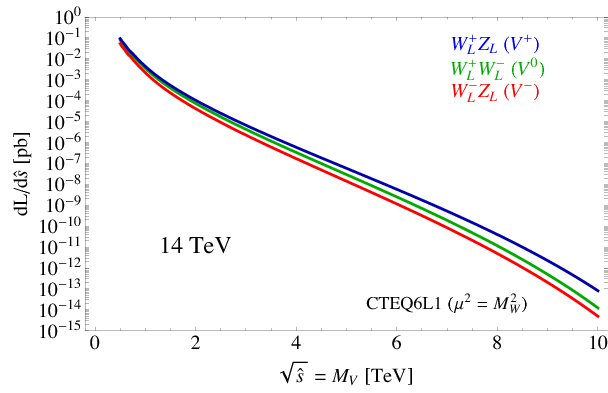


Figure 2.4: Parton luminosities for VBF process between i and j partons, as a function of the parton center-of-mass energy, for the LHC proton-proton collisions performed at 14 TeV.

2.2.4 Benchmark model A: weak coupling scenario

Model A scenario aims at reproducing a simple generalization of the SM [10], obtained by extending the gauge symmetry group with an additional $SU(2)'$. The low-energy phenomena are expected to be dominated by the SM, while the high-energy processes are relevant for the additional symmetry, bringing additional light vector bosons in play.

It can be shown that this kind of picture is portrayed by HVT when $c_H \sim -g^2/g_V^2$ and $c_F \sim 1$. This implies that:

$$\begin{aligned} g_V c_H &\approx g^2/g_V \\ g^2 c_F/g_V &\approx g^2/g_V, \end{aligned} \tag{2.27}$$

hence the partial decay widths into fermions (eq. 2.21) and bosons (eq. 2.25) differ only by a factor 2 and the colour factor (N_c). Branching fractions for the model A benchmark scenario ($g_V = 1$) are shown in fig. 2.5 (left); total widths are reported in fig. 2.5 (right) for different coupling parameters g_V .

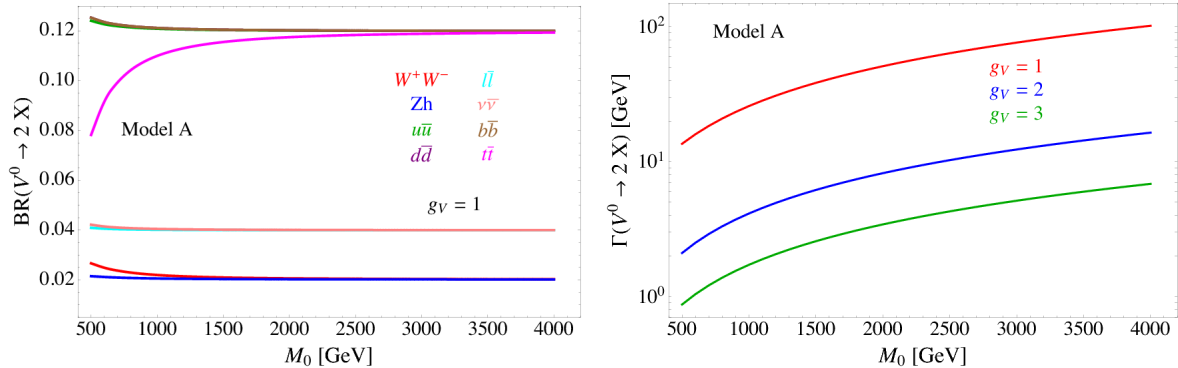


Figure 2.5: HVT model A scenario: branching fractions for fermionic and bosonic decays when $g_V = 1$ (left) as a function of the mass of the resonance M_0 ; total width of the resonance, as a function of its mass, considering different values of the parameter g_V (right).

219 **2.2.5 Benchmark model B: strong coupling scenario**

220 In composite Higgs models [12], the Higgs boson is the result of the spontaneous symmetry breaking
 221 of an $SO(5)$ symmetry to a $SO(4)$ group. New vector bosons are expected to appear, and the lightest
 222 ones can be represented by HVT model B when $c_H \sim c_F \sim 1$.

223 In this case:

$$g_V c_H \approx -g_V \\ g^2 c_F / g_V \approx g^2 / g_V, \quad (2.28)$$

224 hence the decay into bosons is not suppressed by g_V parameter. In the benchmark scenario $g_V = 3$,
 225 decays into dibosons are largely dominant, as it can be seen in fig. 2.6 (left); the total decay width
 226 increases for larger g_V (fig. 2.6, right). When the resonances start to be very broad, *i.e.* $\Gamma/M_V \gg$
 227 0.1, the assumptions leading to the simplified model are no longer valid, hence higher order, non-
 228 resonant effects must be taken into account.

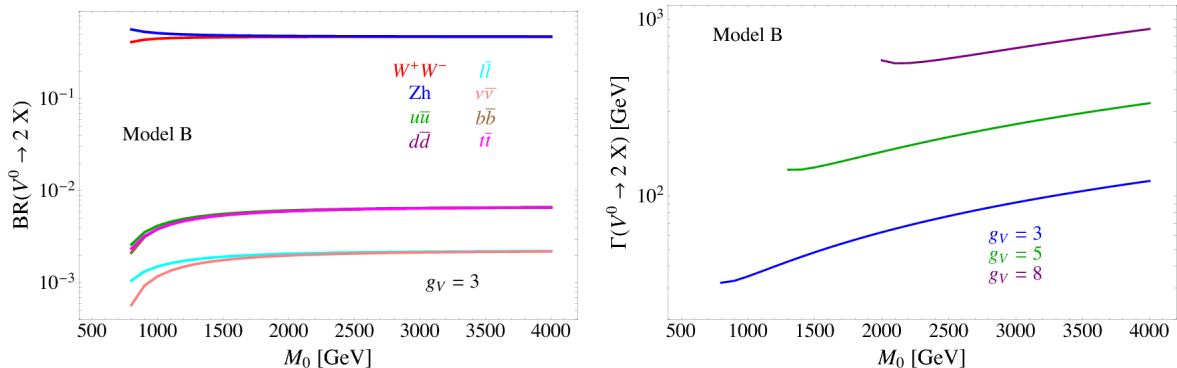


Figure 2.6: HVT model B scenario: branching fractions for fermionic and bosonic decays when $g_V = 3$ (left) as a function of the mass of the resonance M_0 ; total width of the resonance, as a function of its mass, considering different values of the parameter g_V (right).

229 **2.2.6 Search for HVT resonances at LHC**

230 No evidence of HVT resonances has been observed so far at LHC experiments. Data collected by
 231 ATLAS and CMS detectors are used to set limits on the HVT resonance masses and coupling param-
 232 eters. Experimental results from proton-proton collisions performed at a center-of-mass energy of
 233 8 TeV (Run 1 era) at LHC brought to the following conclusions. A weakly coupled resonance, in the
 234 context of benchmark model A ($g_V = 1$) was excluded up to 3 TeV by Run 1 data. By looking at parton
 235 luminosities in fig.2.3, in data produced by LHC proton-proton collision at 14 TeV, collected for an
 236 integrated luminosity of 300 fb^{-1} , the sensitivity is expected to increase up to $m_V \approx 6 \text{ TeV}$. A strongly
 237 coupled resonance, in the context of benchmark model B ($g_V = 3$) is excluded up to 2 TeV by Run 1
 238 data. Data produced by LHC at 14 TeV should increase the sensitivity up to $m_V \approx 3 - 4 \text{ TeV}$.
 239 The most stringent limits are provided by the latest data produced by LHC at a center-of-mass en-
 240 ergy of 13 TeV (Run 2 era).

241 Numerous searches for HVT triplet have been performed at CMS experiment in different final
 242 states: the most sensitive ones were those in all-hadronic topology. [16, 17] (search for WW , WZ ,
 243 ZZ resonances in the $q\bar{q}q\bar{q}$ final state) excludes a W' with mass below 3.6 and a Z' with mass below

2.2 Heavy Vector Triplet

244 2.7 TeV in the model B scenario (fig. 2.7). [18, 19] (search for WH , ZH resonances in the $q\bar{q}b\bar{b}$ final
 245 state) excludes a W' lighter than 2.97 (3.15) TeV in the HVT model A (model B), and a Z' up to 1.67
 246 (2.26) TeV in HVT model A (model B) (fig. 2.8). In fig. 2.9, results of [16, 17] (left) and [18, 19] (right)
 247 searches are interpreted as exclusion contours in the coupling parameter plane of the HVT model
 248 ($g_V c_H$ and $g^2 c_F/g_V$). In the grey shaded area, the narrow width approximation fails. The colored
 249 curves display the parameter exclusion for different mass hypotheses of the triplet. Colored dots
 250 show the model A and B benchmark scenarios.

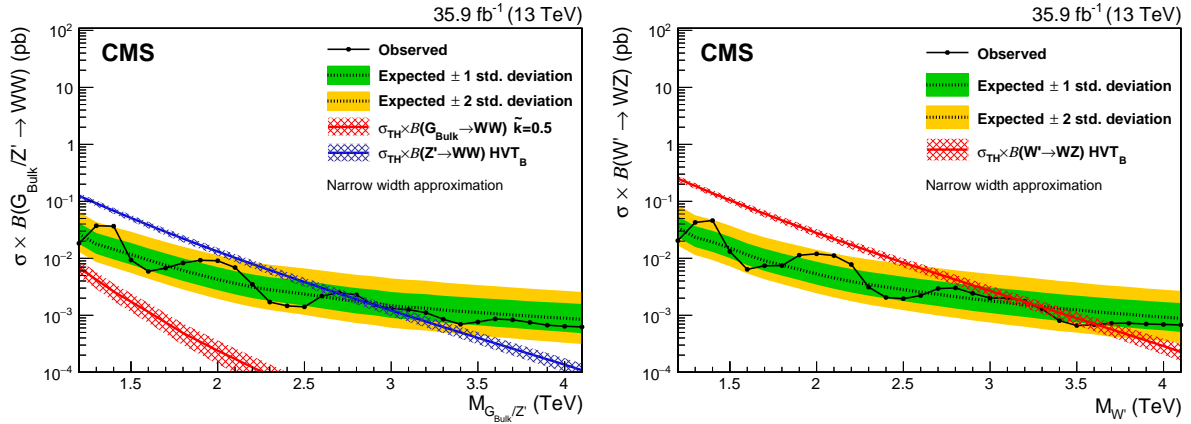


Figure 2.7: The observed and expected limits, with 68% and 95% uncertainty bands, on the product of the cross section and branching fraction $\sigma \mathcal{B}(Z' \rightarrow WW)$ for a spin-1 Z' (left) and $\sigma \mathcal{B}(W' \rightarrow WZ)$ for a spin-1 W' (right), as a function of the reconstructed mass of the diboson resonance. The colored lines show the theoretical predictions for the HVT model B.

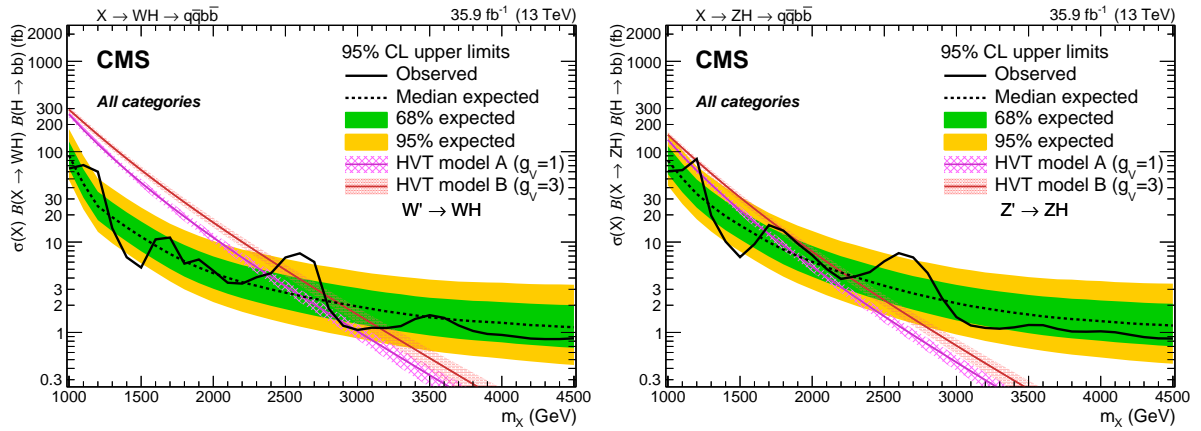


Figure 2.8: The observed and expected limits, with 68% and 95% uncertainty bands, on the product of the cross section and branching fraction $\sigma \mathcal{B}(W' \rightarrow WH)$ for a spin-1 W' (left) and $\sigma \mathcal{B}(Z' \rightarrow ZH)$ for a spin-1 Z' (right), as a function of the reconstructed mass of the diboson resonance. The colored lines show the theoretical predictions for the HVT model A and B.

251 Many other final states have been exploited at CMS: $ZW, ZZ \rightarrow \ell\bar{\ell}q\bar{q}$ [20]; $WH, ZH \rightarrow (\ell\bar{\ell}, \ell\nu, \nu\bar{\nu})b\bar{b}$ [21];
 252 $WZ, WW \rightarrow \ell\nu q\bar{q}$ [22]. Finally, $ZW, ZZ \rightarrow \nu\bar{\nu}q\bar{q}$ [23] results will be extensively described in this
 253 thesis.

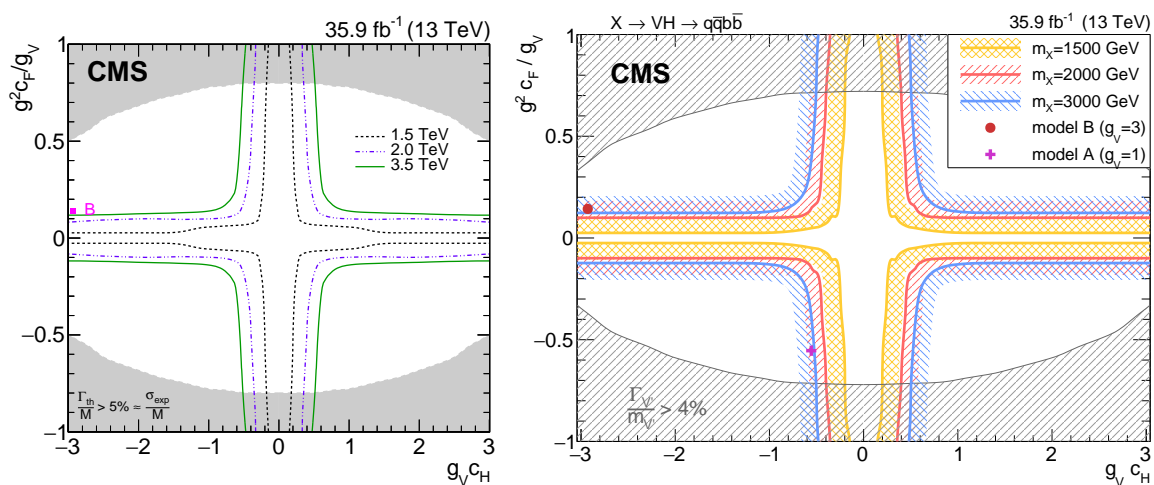


Figure 2.9: Exclusion contours in the coupling parameter plane of the HVT model ($g_V c_H$ and $g^2 c_F / g_V$).

2.2 Heavy Vector Triplet

254 Searches for HVT model B resonances have been performed at ATLAS experiment as well. Re-
 255 sults for a $W' \rightarrow WZ$ reported in fig. 2.10 include the searches performed in $WW, WZ, ZZ \rightarrow q\bar{q}q\bar{q}$
 256 final state [24]; $WZ, WW \rightarrow \ell\nu q\bar{q}$ final state [25]; $ZW, ZZ \rightarrow (\ell\bar{\ell}, \ell\nu, \nu\bar{\nu})q\bar{q}$ final state [26]. The all-
 257 hadronic final state has the best sensitivity and it excludes a W' resonance up to 3.3 TeV (model B
 258 scenario). Results for a $W' \rightarrow WH$ and for a $Z' \rightarrow ZH$ are displayed in fig. 2.11 (left and right respec-
 259 tively), and they include searches performed in $WH, ZH \rightarrow q\bar{q}b\bar{b}$ final state [27], and $WH, ZH \rightarrow$
 260 $\ell\bar{\ell}, \ell\nu, \nu\bar{\nu} b\bar{b}$ [28]. A W' is excluded up to 2.9 TeV and a Z' is excluded up to 2.8 TeV (in the model B
 261 scenario).

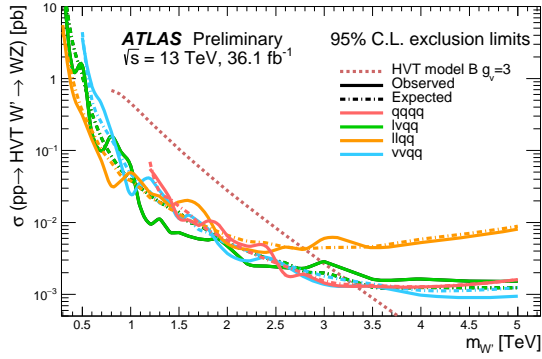


Figure 2.10: The observed and expected limits on the product of the cross section and branching fraction $\sigma \mathcal{B}(W' \rightarrow WZ)$ for a spin-1 W' , as a function of the reconstructed mass of the diboson resonance. The dotted line shows the theoretical predictions for the HVT model B.

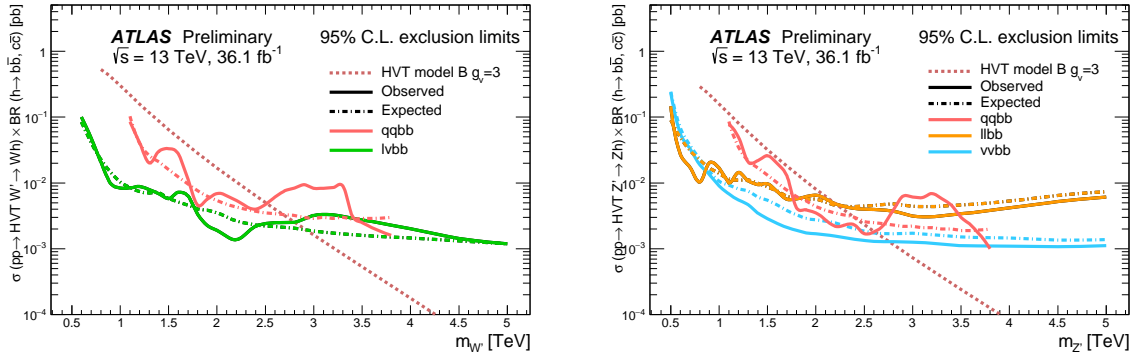


Figure 2.11: The observed and expected limits on the product of the cross section and branching fraction $\sigma \mathcal{B}(W' \rightarrow WH)$ for a spin-1 W' (left) and $\sigma \mathcal{B}(Z' \rightarrow ZH)$ for a spin-1 Z' (right), as a function of the reconstructed mass of the diboson resonance. The colored lines show the theoretical predictions for the HVT model B.

²⁶² **2.3 Warped extra dimension**

²⁶³ The Randall-Sundrum model [29, 30] (RS1) proposes the introduction of one additional warped di-
 264 mension in order to solve the hierarchy problem. The metric of the 5-dimensional space (a slice of
 265 AdS_5) generates an exponential hierarchy between the electroweak and Planck scales, associated re-
 266 spectively to the TeV three-brane, where the SM particles are confined, and the Planck three-brane.
 267 As a consequence of the new geometry, spin-2 massive gravitons are predicted to exist.
 268 The bulk extension of the Randall-Sundrum model [31, 32] states that the SM fields can propagate in
 269 the extra dimension. Light fermions are near the Planck brane, heavy fermions are close to the TeV
 270 brane, while the Higgs sector is confined in the TeV brane. Higgs couplings to the heavy fermions
 271 are therefore expected to be stronger: this naturally arising hierarchy of the masses of the SM fields
 272 gives a solution to the flavour problem. In this scenario, the fermionic decays of the bulk gravitons
 273 are suppressed, while the bosonic decays are preferred.

²⁷⁴ **2.3.1 Randall-Sundrum original model (RS1)**

²⁷⁵ The existence of additional n -dimensions implies that the effective Planck scale observed in 4-
 276 dimensions, $M_{PL} = 1.220910^{19}$ GeV, is related to the fundamental $4+n$ -dimensional Planck scale,
 277 M , via the geometry. M is expected to be of the order of the reduced $\overline{M}_{PL} = M_{PL}/2\pi$. If the 4-
 278 dimensional and the n additional metrics are factorizable, \overline{M}_{PL} is the product of M and the volume
 279 of the compact space V_n :

$$\overline{M}_{PL}^2 = V_n M^{2+n}. \quad (2.29)$$

²⁸⁰ If $M \sim$ TeV, this implies that V_n must be very large, hence the compactification scale $\mu \sim 1/V_n^{1/n}$
 281 is small (eV – MeV for $n=2 - 7$). Given the smallness of μ when compared to the electroweak scale,
 282 the effects of the extra dimensions should be evident in SM processes. Since they are not observed,
 283 SM particles are assumed to be confined in a 4-dimensional space, the TeV three-brane, while only
 284 gravity is allowed to propagate into the $4+n$ -dimensional space, the bulk. This mechanism solves
 285 the hierarchy of the Higgs scale but introduces a new hierarchy between μ and M .
 286 In the Randall-Sundrum model [29, 30], only one additional dimension is added. The geometry of
 287 the 5-dimensional bulk is non-factorizable, and it is a slice of AdS_5 spacetime.¹ The 4-dimensional
 288 metric is multiplied by an exponential function of the fifth dimension (the "warp" factor):

$$ds^2 = e^{-2kr_c\phi} \eta_{\mu\nu} dx^\mu dx^\nu + r_c^2 d\phi^2; \quad (2.30)$$

²⁸⁹ x^μ are the usual 4-dimensional coordinates, $\eta_{\mu\nu} = diag(-1, 1, 1, 1)$ is the Minkowski metric, k is a
 290 scale of order of \overline{M}_{PL} , ϕ is the coordinate of the extra dimension, $0 < |\phi| < \pi$, and r_c is the com-
 291 pactification radius of this finite interval. 4-dimensional mass scales are obtained by multiplying
 292 the bulk masses by $e^{-2kr_c\phi}$: given the exponential form of the warp factor, a small r_c suffices for
 293 generating a large hierarchy between Planck and Higgs scales.

²⁹⁴ Two 4-dimensional three-branes are located at the boundaries of the fifth dimension: the visible
 295 brane at $\phi = \pi$; the hidden brane at $\phi = 0$, and their metrics are obtained starting from the bulk
 296 5-dimensional metric G_{MN} , where $M, N = \mu, \phi$:

$$\begin{aligned} g_{\mu\nu}^{\text{vis}}(x^\mu) &= G_{\mu\nu}(x^\mu, \phi = \pi) \\ g_{\mu\nu}^{\text{hid}}(x^\mu) &= G_{\mu\nu}(x^\mu, \phi = 0). \end{aligned} \quad (2.31)$$

¹An n -dimensional anti-de Sitter space (AdS_n) is a maximally symmetric Lorentz manifold, that solves the Einstein equation with a negative curvature (negative cosmological constant).

2.3 Warped extra dimension

297 The classical action is given by:

$$\begin{aligned} S &= S_{\text{gravity}} + S_{\text{vis}} + S_{\text{hid}} \\ S_{\text{gravity}} &= \int d^4x \int_{-\pi}^{+\pi} d\phi \sqrt{-G} (-\Lambda + 2M^3 \mathcal{R}) \\ S_{\text{vis}} &= \int d^4x \sqrt{-g_{\text{vis}}} (\mathcal{L}_{\text{vis}} - V_{\text{vis}}) \\ S_{\text{hid}} &= \int d^4x \sqrt{-g_{\text{hid}}} (\mathcal{L}_{\text{hid}} - V_{\text{hid}}), \end{aligned} \quad (2.32)$$

298 where G (g) is the trace of the G_{MN} ($g_{\mu\nu}$) metric, Λ is the cosmological constant in the bulk, \mathcal{R} is
299 the 5-dimensional Ricci scalar, \mathcal{L} and V are the lagrangian and the vacuum energy of the hidden
300 and visible branes.

301 A 5-dimensional metric that preserves the 4-dimensional Poincaré invariance has the form:

$$ds^2 = e^{-2\sigma(\phi)} \eta_{\mu\nu} dx^\mu dx^\nu + r_c^2 d\phi^2. \quad (2.33)$$

302 The Poincaré invariance guarantees that r_c does not depend on x^μ . Given 2.33, the solution of the
303 5-dimensional Einstein's equations simplifies into:

$$\sigma = r_c |\phi| \sqrt{\frac{-\Lambda}{24M^3}}. \quad (2.34)$$

304 Furthermore, the Poincaré invariance imposes constraints to the vacuum energies and cosmologi-
305 cal constant:

$$\begin{aligned} V_{\text{hid}} &= -V_{\text{vis}} = 24M^3 k \\ \Lambda &= -24M^3 k^2. \end{aligned} \quad (2.35)$$

306 The final 5-dimensional metric is then:

$$ds^2 = e^{-2kr_c|\phi|} \eta_{\mu\nu} dx^\mu dx^\nu + r_c^2 d\phi^2. \quad (2.36)$$

307 A small r_c is considered, so the effects of the fifth dimension on 4-dimensional spacetime can't
308 be appreciated. A 4-dimensional effective field theory approach is therefore motivated, and its mass
309 parameters are related to the bulk parameters, M , k and r_c . In the Randall-Sundrum model, SM
310 matter fields are confined in the TeV brane.

311 The massless gravitons, the mediators of the gravitational interaction in the effective field theory, are
312 the zero modes ($h_{\mu\nu}$) of the quantum fluctuations of the classical solution (2.36):

$$ds^2 = e^{-2kT(x)|\phi|} (\eta_{\mu\nu} + h_{\mu\nu}(x)) dx^\mu dx^\nu + T^2(x) d\phi^2, \quad (2.37)$$

313 where the usual Minkowski metric has been replaced by $\bar{g}_{\mu\nu}(x) = \eta_{\mu\nu} + h_{\mu\nu}$; $h_{\mu\nu}$ are the tensor fluc-
314 tuations around the Minkowski space, and represent both the physical graviton in 4-dimensions
315 and the massless mode of the Kaluza-Klein decomposition of the bulk metric. r_c is the vacuum ex-
316 pectation value of $T(x)$.

317 By substituting eq. 2.37 in the classical action 2.32, an effective action can be extracted, and in par-
318 ticular the curvature term holds:

$$S_{\text{eff}} \sim \int d^4x \int_{-\pi}^{+\pi} d\phi 2M^3 r_c e^{-2kr_c|\phi|} \bar{\mathcal{R}} \sqrt{-\bar{g}}, \quad (2.38)$$

319 where \bar{g} is the trace of $\bar{g}_{\mu\nu}$ and $\bar{\mathcal{R}}$ is the 4-dimensional Ricci scalar of $\bar{g}_{\mu\nu}$ metric. In this effective
 320 4-dimensional action, the ϕ dependence can be integrated out, and the 4-dimensional Planck mass
 321 can be calculated:

$$\bar{M}_{PL}^2 = M^3 r_c \int_{-\pi}^{+\pi} d\phi e^{-2kr_c|\phi|} = \frac{M^3}{k} (1 - e^{-2kr_c\pi}). \quad (2.39)$$

322 It can be shown [29] that a field with a fundamental mass parameter m_0 in the bulk manifests in the
 323 visible three-brane with a physical mass m :

$$m = e^{-2kr_c\pi} m_0. \quad (2.40)$$

324 Scales $m \sim \text{TeV}$ are generated from $m_0 \sim \bar{M}_{PL}$ if $e^{kr_c\pi} \sim 10^{15}$. This relation stands still when Higgs
 325 field is introduced and confined in the visible three-brane:

$$v = e^{-2kr_c\pi} v_0, \quad (2.41)$$

326 where v is the Higgs vacuum expectation value in the TeV brane and v_0 is the 5-dimensional Higgs
 327 v.e.v.

328 The hierarchy problem is then solved by the exponential warp factor. The weakness of gravity in the
 329 TeV three-brane is motivated by the small overlap of the graviton wave function.

330 In order to calculate the mass spectrum of the graviton in the TeV brane, the tensor fluctuations of
 331 the Minkowski metric are expanded into a Kaluza-Klein (KK) tower $h_{\mu\nu}^{(n)}$:

$$h_{\mu\nu}(x, \phi) = \sum_{n=0}^{\infty} h_{\mu\nu}^{(n)}(x) \frac{\chi^{(n)}(\phi)}{\sqrt{r_c}}. \quad (2.42)$$

332 Once a suitable gauge is chosen, i.e. $\eta^{\mu\nu} \partial_\mu h_{\nu a}^{(n)} = \eta^{\mu\nu} h_{\mu\nu}^{(n)} = 0$, the equation of motion of $h_{\mu\nu}^{(n)}$ becomes
 333 the Klein-Gordon relation, where $m_n^G \geq 0$:

$$(\eta^{\mu\nu} \partial_\mu \partial_\nu - (m_n^G)^2) h_{\mu\nu}^{(n)}(x) = 0. \quad (2.43)$$

334 By substituting eq. 2.42 into Einstein's equation, the solutions for $\chi^{(n)}(\phi)$ (commonly called "pro-
 335 files") are [33, 34]:

$$\chi^{(n)}(\phi) = \frac{e^{2\sigma}}{N} [J_2(z_n^G) + \alpha_n Y_2(z_n^G)], \quad (2.44)$$

336 where J_2 and Y_2 are second order Bessel functions, N is the normalization of the wavefunction, α_n
 337 are coefficients and $z_n^G = m_n^G e^{\sigma(\phi)}/k$. m_n^G is the mass of the n -mode, and it depends on the roots
 338 of the Bessel functions $z_n^G = (3.83, 7.02, 10.17, 13.32, \dots)$. In the limit $m_n^G/k \ll 1$ and $e^{kr_c\pi} \gg 1$:

$$m_n^G = k z_n^G(\pi) e^{-kr_c\pi}. \quad (2.45)$$

339 The interactions between the graviton KK modes and the matter fields in the TeV brane can be de-
 340 rived from the 4-dimensional effective Lagrangian, once $h_{\mu\nu}$ is replaced by its KK decomposition:

$$\mathcal{L} = -\frac{1}{\bar{M}_{PL}} T^{\mu\nu}(x) h_{\mu\nu}^{(0)} - \frac{1}{e^{-kr_c\pi} \bar{M}_{PL}} T^{\mu\nu}(x) \sum_{n=1}^{\infty} h_{\mu\nu}^{(n)}(x); \quad (2.46)$$

342 $T^{\mu\nu}$ is the space energy-momentum tensor of the matter fields. The zero mode of the gravitons cou-
 343 pling is $1/\bar{M}_{PL}$, while higher order KK modes couplings to all SM fields are suppressed by $e^{-kr_c\pi} \bar{M}_{PL}$,
 344 that is of the order of the TeV scale. Spin-2 KK masses and couplings are hence determined by the
 345 TeV scale, or, equivalently, KK gravitons are close to the TeV brane. This implies that KK gravitons
 346 can be produced via $q\bar{q}$ or gluon fusion, and that a leptonic decay of the resonance could represent
 347 a very clear signal signature.

2.3 Warped extra dimension

2.3.2 Bulk extension of RS1: graviton production and decays

An extension of the original RS1 formulation has been proposed. It states that the usual SM fields are no longer confined in the TeV brane, but they are the zero modes of the corresponding 5-dimensional SM fields. If first and second generation fermions are close to the Planck brane, contribution to flavour changing neutral currents by higher-dimensional operators are suppressed. These contributions are excluded by electroweak precision tests, but they were not prevented in original RS1. The second motivation behind the choice is, as mentioned previously, the naturally arising flavour hierarchy: first and second generation quarks have small Yukawa couplings to the Higgs sector, confined in the TeV brane, while top quark and bosons have stronger Yukawa couplings.

In this picture, couplings between higher-order KK gravitons and light fermions are strongly suppressed, resulting into a negligible KK gravitons production via $q\bar{q}$, whilst gluon fusion production becomes dominant. KK gravitons decay into top quarks and Higgs bosons are dominant, given that both their profiles are near the TeV brane, while leptonic decays are negligible. Via the equivalence theorem, the Goldstone bosons are equivalent to the longitudinally polarized weak bosons, W_L^\pm and Z_L , that have profiles close to the TeV brane. Decays of KK gravitons into weak dibosons (and production in VBF) are comparable to di-top and di-Higgs decays.

The KK decomposition and the KK mass spectrum of the graviton have already been presented in sec. 2.3.1. The KK decomposition of a massless 5-dimensional gauge field $A_M(x, \phi)$ is similarly performed [35]:

$$A_\mu(x, \phi) = \sum_{n=0}^{\infty} A_\mu^{(n)}(x) \frac{\chi^{(n)_A}(\phi)}{\sqrt{r_c}}. \quad (2.47)$$

The profiles for the gauge fields are:

$$\chi_A^{(n)}(\phi) = \frac{e^\sigma}{N_A} [J_1(z_n^A) + \alpha_n^A Y_1(z_n^A)], \quad (2.48)$$

where J_1 and Y_1 are first order Bessel functions. Similarly to eq. 2.49, the mass spectrum of the gauge field is:

$$m_n^A = k z_n^A(\pi) e^{-k r_c \pi}; \quad (2.49)$$

the first roots of the Bessel functions are $z_n^A = (2.45, 5.57, 8.70, 11.84, \dots)$.

The Lagrangian expressing the interaction between the m and n modes of the bulk field F to the q KK gravitons mode G is [35]:

$$\mathcal{L}_{G-F} = \sum_{m,n,q} C_{mnq}^{FFG} \frac{1}{M_{PL}} \eta^{\mu\alpha} \eta^{\nu\beta} h_{\alpha\beta}^{(q)}(x) T_{\mu\nu}^{(m,n)}(x), \quad (2.50)$$

C_{mnq}^{FFG} is the overlap integral of the profiles:

$$C_{mnq}^{FFG} = \int \frac{d\phi}{\sqrt{k}} e^{t\sigma} \frac{\chi_F^{(m)} \chi_F^{(n)} \chi_G^{(q)}}{\sqrt{r_c}}; \quad (2.51)$$

t depends on the type of field considered.

The coupling between gluons and the q KK graviton mode is given by:

$$C_{00q}^{AAG} = e^{k\pi r_c} \frac{2[1 - J_0(x_n^G)]}{k\pi r_c (x_n^G)^2 |J_2(x_n^G)|}. \quad (2.52)$$

³⁷⁷ Once eq. 2.52 is put in eq. 2.50, the most significant partial decay widths into the q KK graviton mode
³⁷⁸ are:

$$\begin{aligned}\Gamma(G \rightarrow t_R \bar{t}_R) &\sim N_c \frac{\left[\tilde{k} x_q^G\right]^2 m_q^G}{320\pi} \\ \Gamma(G \rightarrow hh) &\sim \frac{\left[\tilde{k} x_q^G\right]^2 m_q^G}{960\pi} \\ \Gamma(G \rightarrow W_L^+ W_L^-) &\sim \frac{\left[\tilde{k} x_q^G\right]^2 m_q^G}{480\pi} \\ \Gamma(G \rightarrow Z_L Z_L) &\sim \frac{\left[\tilde{k} x_q^G\right]^2 m_q^G}{960\pi},\end{aligned}\tag{2.53}$$

³⁷⁹ where $\tilde{k} = k/\overline{M}_{PL}$; the total decay width is:

$$\Gamma_G = \frac{13 \left[\tilde{k} x_q^G\right]^2 m_q^G}{960\pi}.\tag{2.54}$$

³⁸⁰ Calculations, so far, have been performed considering $M \sim \overline{M}_{PL}$ and $k < M$, hypotheses under
³⁸¹ which the solution for the bulk metric (eq. 2.36) is valid. Hence, $\tilde{k} = k/\overline{M}_{PL} \leq 1$ is taken as a ref-
³⁸² erence interval. This has also phenomenological consequences on the width of the resonance, as
³⁸³ stated in eq. 2.54. The total decay width of the lightest KK graviton mode, compared to its mass,
³⁸⁴ is shown as a function of \tilde{k} in fig. 2.12 [36]. At $\tilde{k} = 1$, in the bulk scenario, the KK graviton width is
³⁸⁵ expected to be few % of its mass, up to 4 TeV (dotted red curve). The narrow width approximation
³⁸⁶ holds, hence the resonance properties can be probed at the peak, neglecting the effects in the tails
³⁸⁷ of the mass distribution.

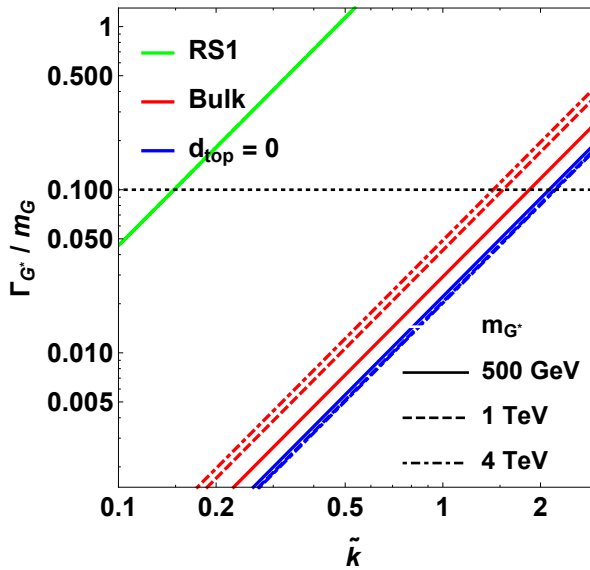


Figure 2.12: Width of the KK gravitons, in units of the mass of the resonance, as a function of the curvature parameter \tilde{k} . The red curves represent the bulk extension of RS1 original model for different mass hypotheses (from 500 GeV up to 4 TeV).

³⁸⁸ The total cross-section of a bulk graviton, produced at LHC in proton-proton interactions via
³⁸⁹ gluon fusion (displayed in fig. 2.13), decaying into a couple of vector bosons (for the purpose of this

2.3 Warped extra dimension

thesis, a final state with two longitudinally polarized Z bosons is considered) is expressed as a function of the parton level cross-section $\hat{\sigma}$, the gluon parton distribution functions f_g , the momentum transfer $Q^2 \sim (m_q^G)^2$ and the center-of-mass energy s :

$$\sigma(pp \rightarrow ZZ) = \int dx_1 dx_2 f_g(x_1, Q^2) f_g(x_2, Q^2) \hat{\sigma}(x_1 x_2 s). \quad (2.55)$$

The differential parton level cross-section, averaged over colors and initial spin states, is (hatted quantities are calculated in the center-of-mass frame):

$$\frac{d\hat{\sigma}(gg \rightarrow ZZ)}{d \cos \hat{\theta}} \approx \frac{|\mathcal{M}_{+00}|^2}{1024\pi \hat{s}}, \quad (2.56)$$

where $|\mathcal{M}_{+00}|$ is the matrix element of the dominant contribution in $gg \rightarrow VV$ process (Γ_G is defined in eq. 2.54, a, b are color factors):

$$\mathcal{M}_{+00}(g^a g^b \rightarrow VV) = -C_{00q}^{AAG} e^{-k\pi r_c} \left(\frac{x_n^G \tilde{k}}{m_n^G} \right)^2 \sum_n \frac{\delta_{ab} \mathcal{A}_{+00}}{\hat{s} - m_n^G + i\Gamma_G m_n^G}. \quad (2.57)$$

The relevant amplitudes taken account in the matrix element calculation are [31]:

$$\mathcal{A}_{+00} = \mathcal{A}_{-00} = \frac{(1 - 1/\beta_Z^2)(\beta_Z^2 - 2)[(\hat{t} - \hat{u})^2 - \beta_Z^2 \hat{s}^2]\hat{s}}{8M_Z^2}, \quad (2.58)$$

where $\beta_Z^2 = 1 - 4M_Z^2/\hat{s}$ and M_Z is the mass of the Z boson.

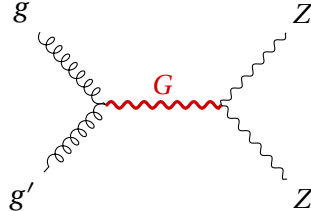


Figure 2.13: Gluon fusion production mechanism for a KK graviton that decays in a couple of Z bosons.

399 **2.3.3 Search for KK bulk gravitons at LHC**

400 No evidence of spin-2 bulk graviton resonances has been observed so far at LHC experiments. Data
 401 collected by ATLAS and CMS detectors are used to set limits on the graviton masses, generally con-
 402 sidering different curvature parameter \tilde{k} hypotheses, once assured the narrow width approximation
 403 is still valid (up to $\tilde{k} \sim 1$). The most stringent limits have been set with Run 2 data.

404 Many results of the diboson searches performed at CMS and already presented in sec. 2.2.6 are
 405 interpreted in the context of the bulk gravitons, together with the additional final states $WZ, ZZ \rightarrow$
 406 $\ell\bar{\ell}\nu\bar{\nu}$ [37] and $HH \rightarrow b\bar{b}b\bar{b}$ [38]. The most interesting limit is provided by [37], that, under the
 407 hypothesis $\tilde{k} = 0.5$, excludes a spin-2 bulk graviton with a mass lower than 800 GeV (fig. 2.14).

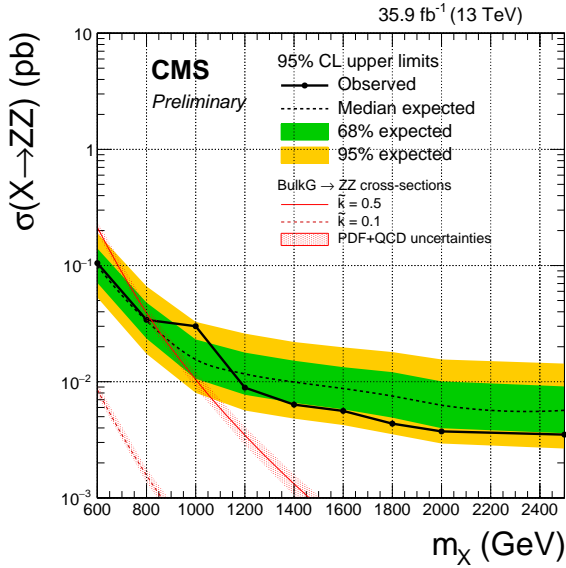


Figure 2.14: The observed and expected limits, with 68% and 95% uncertainty bands, on the product of the cross section and branching fraction $\sigma \mathcal{B}(G \rightarrow ZZ)$ for a spin-2 bulk graviton, as a function of the reconstructed mass of the diboson resonance. The colored lines show the theoretical predictions for $\tilde{k} = 0.1$ and 0.5 .

408 Similarly for ATLAS experiment, searches for diboson resonances in sec. 2.2.6 have been inter-
 409 preted in the graviton context. The most stringent limit is given by [25], where, under the assump-
 410 tion $\tilde{k} = 1$, a spin-2 bulk graviton with mass lower than 1.76 TeV is excluded (fig. 2.15).

2.3 Warped extra dimension

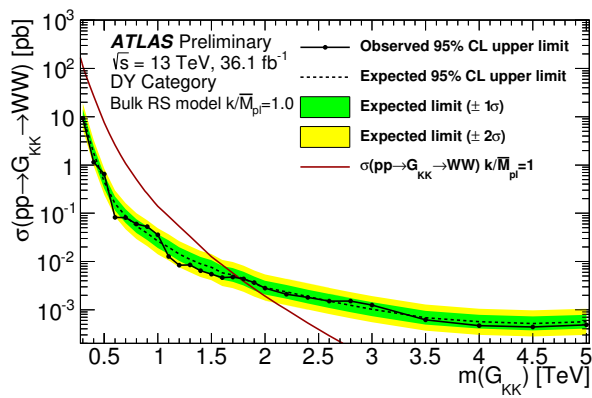


Figure 2.15: The observed and expected limits, with 68% and 95% uncertainty bands, on the product of the cross section and branching fraction $\sigma \mathcal{B}(G \rightarrow ZZ)$ for a spin-2 bulk graviton, as a function of the reconstructed mass of the diboson resonance. The colored lines show the theoretical predictions for $\tilde{k} = 1$.

The Large Hadron Collider and the CMS experiment

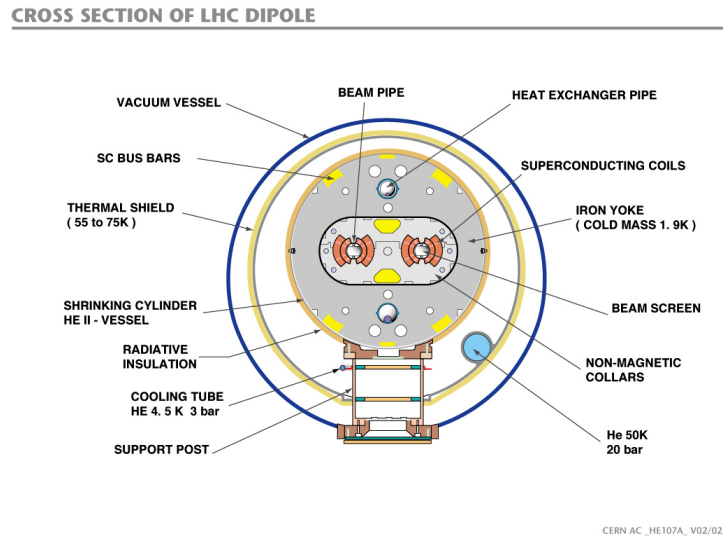
414 3.1 The Large Hadron Collider

415 The Large Hadron Collider (LHC) is a 27 km ring structure designed for the acceleration and collision
 416 of protons and heavy ions. It is situated approximately 100 m underground, between France and
 417 Switzerland, in the Geneva area, and it is the most important of the CERN (Conseil européen pour
 418 la recherche nucléaire) facilities. In order to reduce the cost of the project, definitively approved in
 419 1996, the LHC has been designed to fit the pre-existing underground tunnel of the Large Electron-
 420 Positron collider (LEP) [ref. 24 Jacopo], built to accelerate electrons and positrons and running until
 421 the year 2000.

422 Moving from an electron-positron collider to an hadron collider allowed to reach higher energies in
 423 the center-of-mass frame, since the synchrotron radiation loss is inversely proportional to the fourth
 424 power of the mass of the particle involved: hence, it is reduced by a factor $m_p/m_e \sim 10^3$. Furthermore,
 425 at a proton-proton collider it is possible to collect higher luminosities (and hence more
 426 statistics) with regards to, for example, a proton-antiproton collider, like Tevatron at Fermilab, in
 427 the USA.

428 In the LHC two identical beam pipes rings are designed to let protons circulate in opposite directions, in ultrahigh vacuum conditions (10^{-11} – 10^{-10} mbar) in order to avoid collisions with gas
 429 molecules. Given the reduced available diameter in the tunnel (4 m), the two proton beams are
 430 magnetically coupled. The collider is composed by 8 arc sections (48 km) driving protons around
 431 the ring, and straight sections (6 km) where beam control systems and detectors are inserted. Pro-
 432 ton beams collide in four interaction points, where the four main LHC experiments are installed:
 433 ALICE, ATLAS, CMS, LHCb.

435 In fig. 3.1, a slice of the arc section is displayed. Around the beam pipes, two superconducting mag-
 436 netic dipoles are located: they generate vertical magnetic fields in opposite directions. The super-
 437 conducting coils are made of niobium-titanium, materials that are superconducting at very low
 438 temperature. At the LHC, they are kept at a temperature of 1.9 K (-271.3°C) by a closed liquid helium
 439 circuit. A current of 11850 A flows through the magnets, without any energy loss due to electrical
 440 resistance, generating a magnetic field of 8.33 T. Magnets of higher order in multipole expansion
 441 (quadrupoles, sextupoles, octupoles, ...) are used to optimize the proton trajectories; in particular,



CERN AC _HE107A_ V02/02/98

Figure 3.1: Section of the LHC dipole magnet structure.

- 442 quadrupoles allow to focus and squeeze the beams. Along the LHC ring here are 9593 magnets; 1232
443 are dipoles, 392 are quadrupoles.

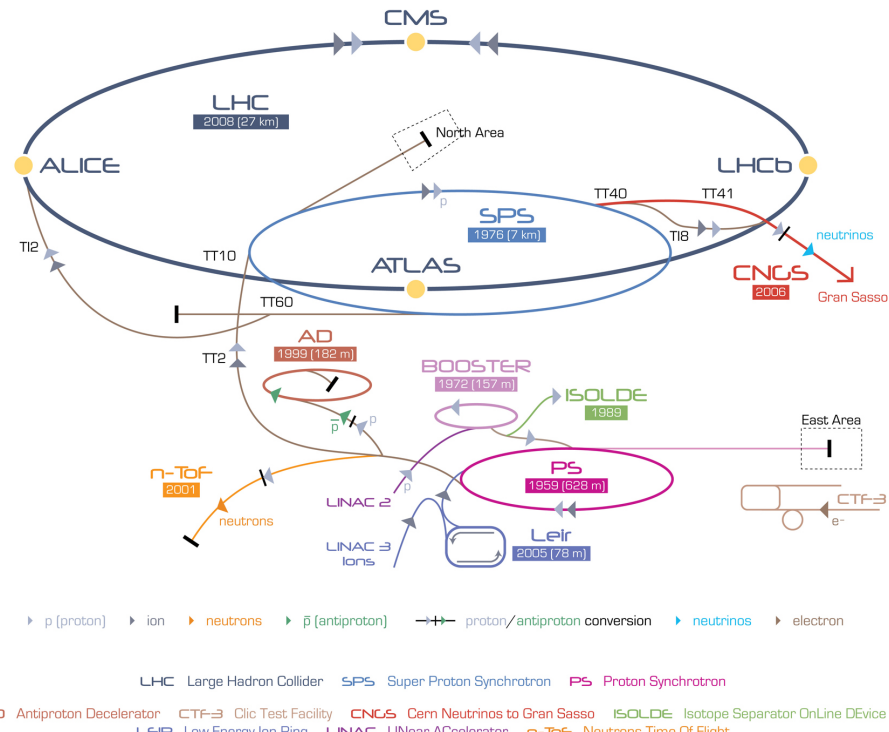


Figure 3.2: The CERN accelerator complex.

- 444 The LHC represents the final step of the CERN accelerator complex, showed in fig. 3.2. Protons are
445 extracted from hydrogen atoms and inserted in the linear accelerator Linac2, that brings them to an
446 energy of 50 MeV. They circulate around a little synchrotron, Proton Synchrotron Booster, reaching
447 an energy of 1.4 GeV, and then in the Proton Synchrotron (PS), where their energy is increased to 25

3.1 The Large Hadron Collider

448 GeV. The second to last step is the Super Proton Synchrtotron, SPS, accelerating protons up to 450
449 GeV. They are finally injected in the Large Hadron Collider, where sixteen radiofrequency cavities
450 (RF) accelerate protons inside each beam up to an energy of 6.5 TeV, providing a center-of-mass en-
451 ergy of 13 TeV when colliding. The RF cavities provide an accelerating electromagnetic field up to 5
452 MV/m (maximum voltage of 2 MV), that oscillates with a frequency of 400 MHz. Like the magnets,
453 the cavities are kept at low temperature (4.5 K, or -268.7°C) in order to allow superconducting con-
454 ditions. The maximum beam energy can be reached in 15 minutes. After several hours of collisions
455 (~ 10 hours), the quality of the beams deteriorates and they are extracted from the machine and
456 dumped.

457
458 Protons circulate inside the LHC ring in bunches of $\sim 10^{11}$ particles each, 80 mm long. Focusing
459 magnets allow to reduce the bunch diameter down to 16 μm . Different bunches are separated by 25
460 ns (or, ~ 7.5 m), corresponding to a frequency of 40 MHz and an instantaneous (peak) luminosity
461 (defined in eq. 3.1) of $1.2 \times 10^{34} \text{ cm}^{-2}\text{s}^{-1}$. Given the structure of the beams, at every bunch crossing
462 many protons interact simultaneously: this phenomenon is called pile-up. The designed maximum
463 number of bunches is 2808.

464
465 The main parameters that describes an hadronic collider are the center-of-mass energy, correspond-
466 ing to the sum of the energies of the beams, and the instantaneous luminosity, that describes the
467 frequency of the interactions among the bunches in the beams. If the bunches in the first beam
468 contain n_1 protons, and the bunches in the second beam contain n_2 protons, and if the colliding
469 area is Σ , the frequency of complete turns around the ring is f , the instantaneous luminosity $\mathcal{L}_{\text{inst}}$
470 is:

$$\mathcal{L}_{\text{inst}} = f \frac{n_1 n_2}{\Sigma}. \quad (3.1)$$

471 If a generic physics procces i has a cross-section of σ_i , the interaction rate R_i is:

$$R_i = \frac{dN_i}{dt} = \sigma_i \mathcal{L}_{\text{inst}}, \quad (3.2)$$

472 and the number of events recorded in the time interval $(0, \tau)$ is obtained by the integrated luminosity
473 $\mathcal{L} = \int_0^\tau \mathcal{L}_{\text{inst}} dt$:

$$N_i = \sigma_i \int_0^\tau \mathcal{L}_{\text{inst}} dt. \quad (3.3)$$

474 In fig. 3.3, a summary of the luminosity measurement in 2016 data is presented. The luminosity
475 delivered by LHC is represented in blue, the recorded by CMS is in orange. The mean number of
476 interaction per bunch crossing (pile-up) is presented as well. The average number of interactions
477 per collision is 27, the maximum is around 50.

478 3.1.1 Proton-proton interactions

479 Proton-proton collisions allow to reach higher energies and luminosities, but the drawback is the
480 complexity of the events when compared to electron-positron collisions: not only because of the in-
481 creasing backgrounds due to strong interactions among partons, but also because the momenta of
482 the proton partons taking part in the interaction are unknown; not to mention the problem of disen-
483 tangling the tracks of the particles coming from the interesting hard interactions from the spectator
484 pile-up interactions (in fig. 3.4, 78 proton collisions were happening at the same bunch crossing).
485 The majority of the LHC events is represented by soft interactions, with low transverse momen-
486 tum transfer, namely elastic and diffractive scatterings. In the so-called hard interactions, on the

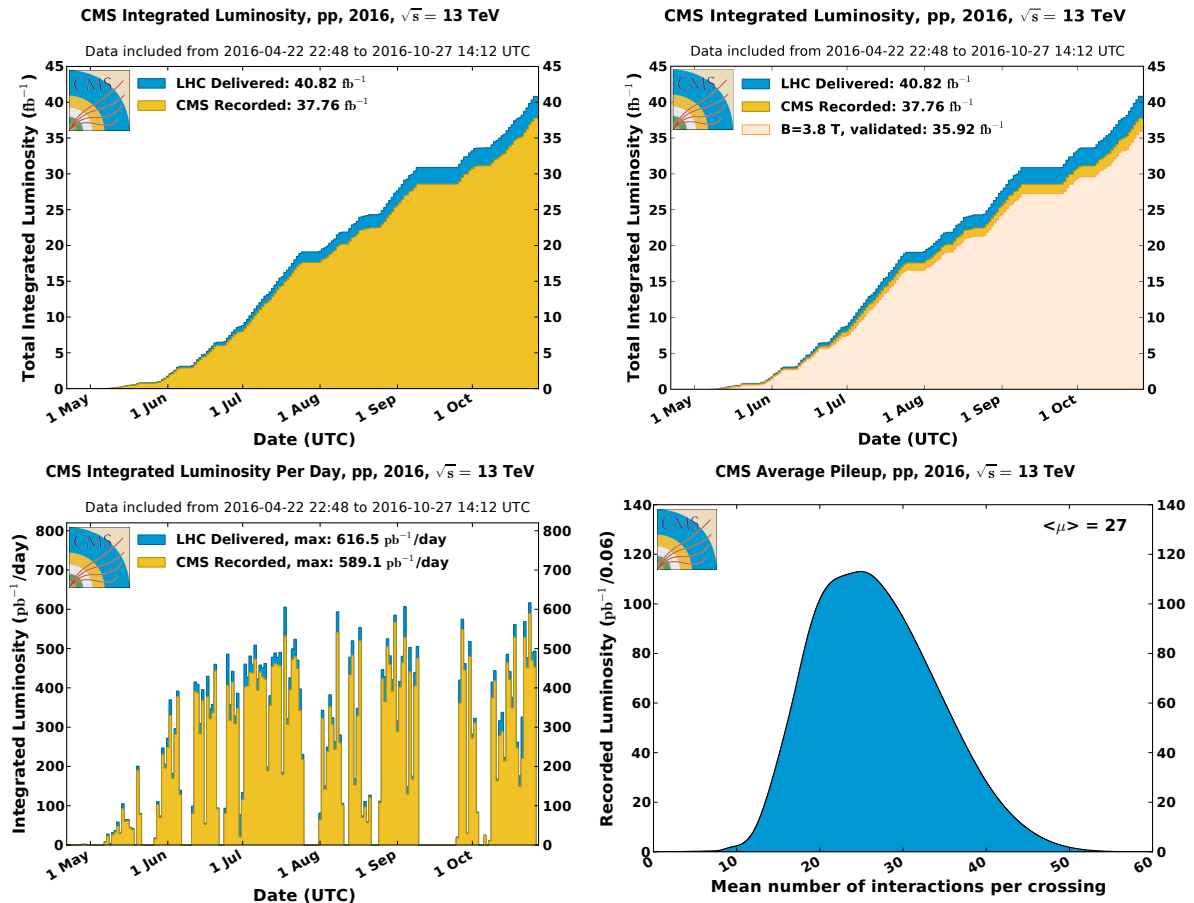


Figure 3.3: Luminosity in 2016 LHC data. Top-left plot: the cumulative integrated luminosity delivered by LHC (in blue) and recorded by CMS (in orange), as a function of the data taken period. Top-right plot: data recorded by CMS and declared as optimal for the physics analyses (in light orange), corresponding to a total integrated luminosity of 35.9 fb^{-1} . Bottom-left plot: maximum integrated luminosity per day. Bottom-right plot: number of proton interactions per bunch crossing (pile-up).

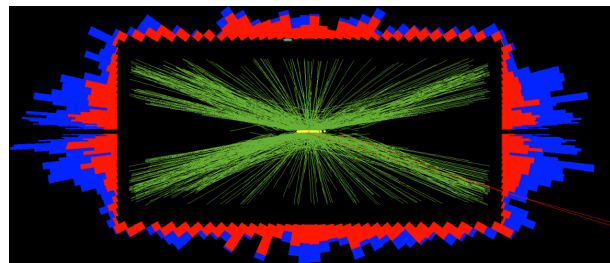


Figure 3.4: CMS collision event, where a record of 78 interactions per single bunch crossing were taking place simultaneously.

other hand, the transferred momentum among particles is high, allowing to produce massive resonant phenomena. These events manifest in peculiar final state signatures that can be distinguished from the soft interaction background.

At high momentum transfer (perturbative regime), a proton can be described as a collection of partons, each bringing a fraction x of the initial beam momentum, whose distribution is described by

3.2 CMS detector

492 the parton distribution functions (PDF), $f(x, Q^2)$, as a function of the Bjorken's variable and of the
 493 momentum transfer Q^2 . At very high center-of-mass energies (13 TeV), the proton masses can be
 494 neglected; the available energy in the parton 1 and parton 2 scattering is unknown, $\sqrt{x_1 x_2 s}$. The
 495 total cross-section is given by:

$$\sigma = \int dx_1 f_1(x_1, Q^2) \int dx_2 f_2(x_2, Q^2) \sigma_{12}(x_1 p_1, x_2 p_2, Q^2), \quad (3.4)$$

496 where σ_{12} is the cross-section at parton level, and f_1, f_2 are the parton PDFs. In fig. 3.5, parton
 497 cross-sections are displayed as a function of the center-of-mass energy.

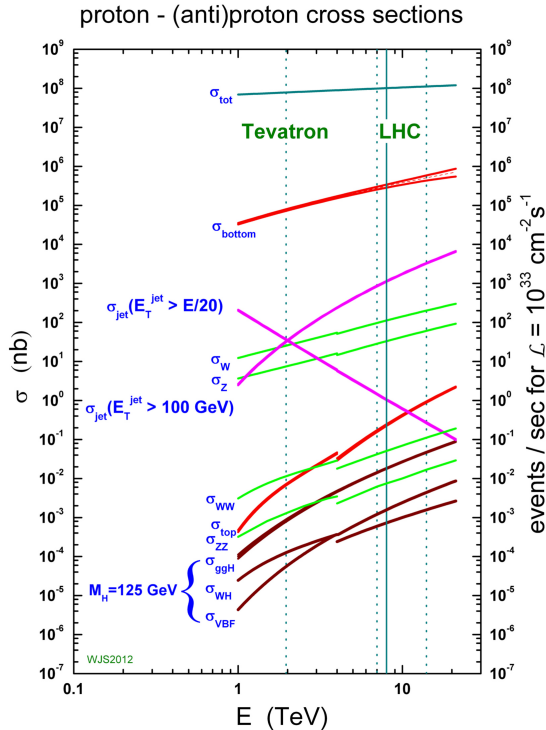


Figure 3.5: Cross-sections and number of expected events in proton-proton collisions, as a function of the center-of-mass energy. Rare phenomena, such as the Higgs boson production, can be observed at the LHC.

498 3.2 CMS detector

499 The Compact Muon Solenoid (CMS) is a multi-purpose detector built in the LHC ring. It is situated
 500 in a cavern 100 m underground, near Cessy, in France. It is a cylinder 22 m long, with a diameter of
 501 15 m, and a weight of 12500 tons. Its physics programme includes the search for the Higgs boson
 502 (discovered in 2012), precision measurements of the Standard Model parameters and rare decays
 503 (physics of beauty quark), and search for new physics beyond the standard model (SUSY, exotic
 504 phenomena, dark matter, extra dimensions).

505 The CMS detector is structured in many layers of sub-detectors, giving different responses depending
 506 on the nature and the momentum of the particle passing through. The inner detectors have
 507 been finely segmented in order to afford the high radiation levels and particle multiplicity at the

508 interaction point, so that the reduced occupancy of each layer allows to measure and distinguish
 509 precisely the primary vertices of the hard interactions from the pile-up events. A very precise time
 510 resolution is vital in order to synchronize all the subsystems together.

511

CMS Detector

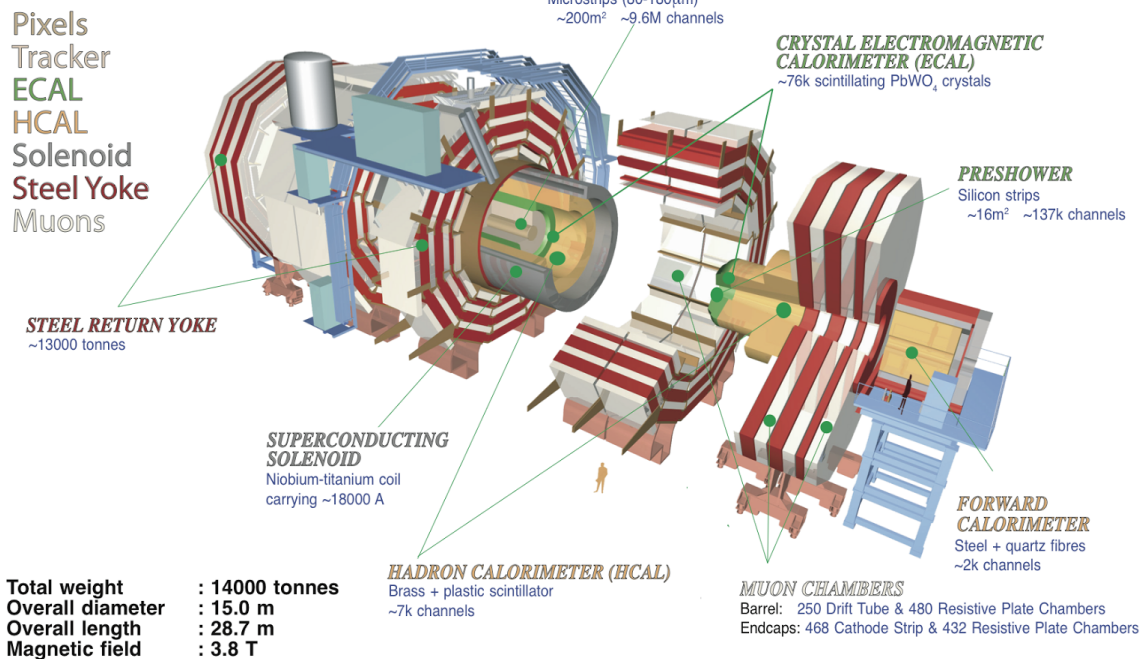


Figure 3.6: The CMS experiment.

512 Fig. 3.6 shows a sketch of the CMS detector. It is longitudinally segmented in the barrel region and
 513 two endcaps. In the forward region (over the endcaps), where the beam radiation is very intense,
 514 additional calorimeters have been placed. In fig. 3.7, the mean path of a specific particle through
 515 the sub-detectors is represented, depending on its flavour.
 516 A detailed description of the CMS detector can be found in [39].

517 3.2.1 The coordinate system

518 The CMS coordinate system is depicted in fig. 3.8. x and y are the coordinates in the transverse
 519 plane, z is the longitudinal coordinate. The x axis points at the center of the LHC ring, the y axis
 520 points upward, the z axis is along the beam direction. The azimuthal angle ϕ lies in the transverse
 521 plane, and it is measured starting from the x axis; the radial coordinate is r . The polar
 522 angle θ lies in the plane rz . The transverse component of the 3-momentum, \vec{p}_T , is orthogonal to
 523 the beam axis and lies in the plane xy . The transverse energy is defined as the magnitude of \vec{p}_T :
 524 $E_T = E \sin \theta$.

525 Two other commonly used variables are the rapidity, y , and pseudorapidity, η , defined as functions
 526 of the particle energy E , the longitudinal component of the momentum p_z and the 3-momentum

3.2 CMS detector

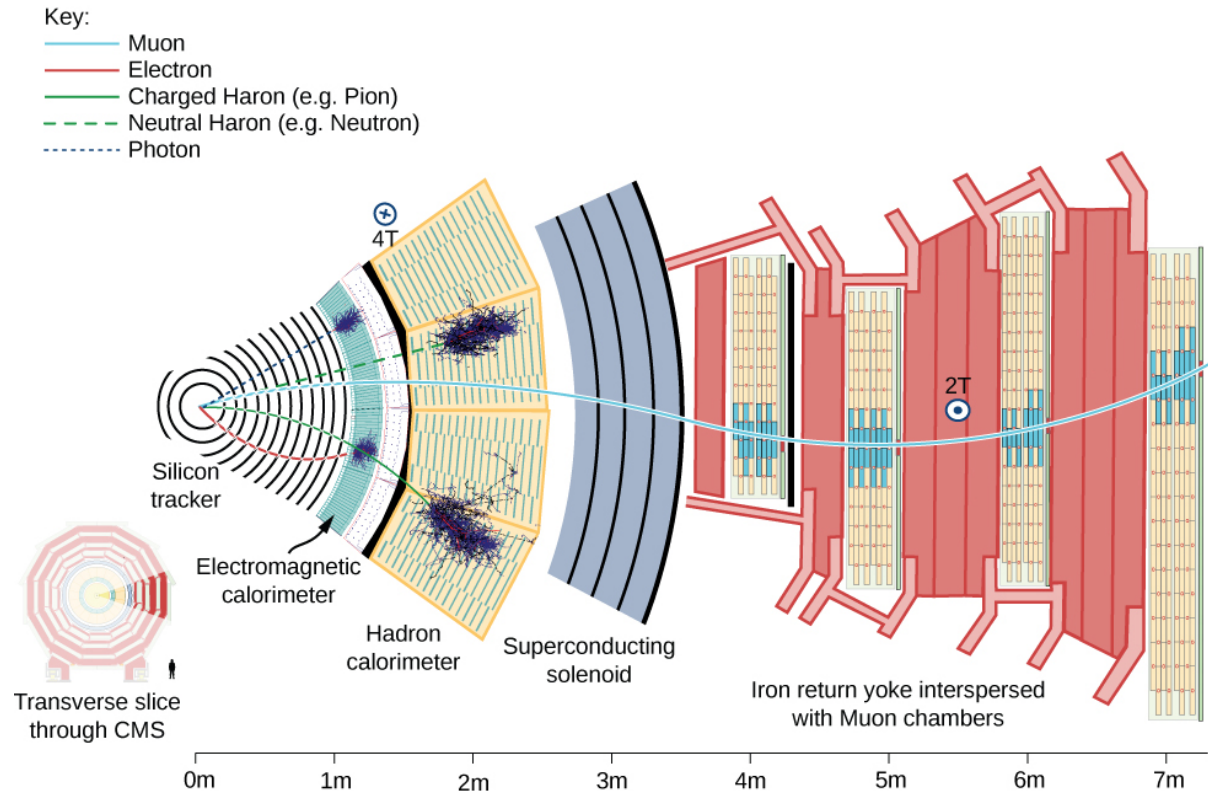


Figure 3.7: Mean path of a particle through the CMS detector. A muon, in light blue, passes through with a bended trajectory, depending on its momentum and charge, triggering signals in all the subsystems. An electron, in red, leaves a track in the silicon tracker and is absorbed by the electromagnetic calorimeter. A neutral or charged hadron, in green, stops inside the hadronic calorimeter. A photon, dotted blue line, showers in the electromagnetic calorimeter, without leaving any track in the silicon detector.

527 modulus:

$$y = \frac{1}{2} \log \frac{E + p_z}{E - p_z}$$

$$\eta = \frac{1}{2} \log \frac{|\vec{p}| + p_z}{|\vec{p}| - p_z} = -\log \tan \frac{\theta}{2}. \quad (3.5)$$

528 When the considered particle is produced in the forward region, hence at $\theta = 0$, $\eta \rightarrow \infty$. When
 529 the particle is produced in the transverse plane, hence $\theta = \pi/2$, $\eta = 0$. At high energies, when the
 530 masses can be neglected, rapidity and pseudorapidity coincide; these variables are largely used at
 531 colliders because they are invariant under Lorentz boosts along the beam direction.

532 3.2.2 The magnet

533 The CMS superconducting magnet is an hollow cylinder (13 m long, 6 m of diameter, showed in
 534 fig. 3.9). In the niobium and titanium fibers that constitute the solenoid, an electrical current of
 535 19 kA flows, providing a maximum magnetic field of 3.8 T and storing a maximum energy of 2.6 GJ.
 536 Superconductiong conditions are allowed by a liquid helium cooling system, keeping the solenoid at
 537 4.5 K. In order to avoid stray fields, the magnetic field lines are closed by the return yoke, composed
 538 by 10 ktons of magnetized iron blocks, located in the outer part of CMS and alternated to the muon

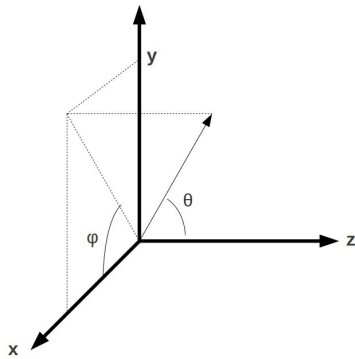


Figure 3.8: CMS coordinate system.

539 chambers. The homogeneous magnetic field inside the detector bends the trajectories of the charged
 540 particles, allowing the measurement of their momenta p , given the relation with the magnetic field
 541 strength B and the radial coordinate R of the trajectory:

$$p[\text{GeV}] = 0.3 \times B[\text{T}] \times R[\text{m}]. \quad (3.6)$$

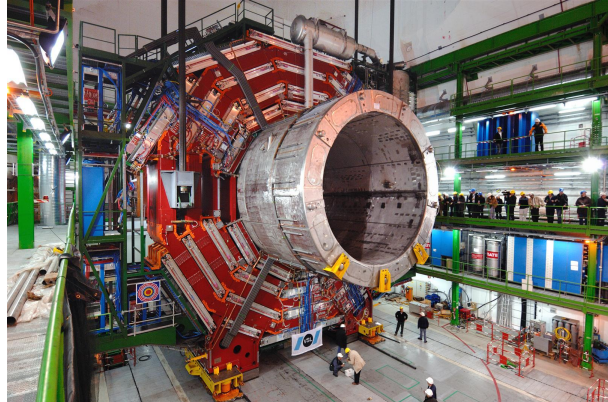


Figure 3.9: Installation of the superconducting solenoid in the CMS cavern.

542 3.2.3 The tracking system

543 The CMS tracking system [40, 41] is composed by a cylinder of silicon detectors (2.5 m of diameter
 544 and 5.8 m length). Their design allows a precise reconstruction of the tracks left by charged particles
 545 and of the interaction vertices, a fundamental tool to identify heavy quarks (charm, beauty) and
 546 leptons (taus). Tracker detectors cover a pseudorapidity region of $|\eta| < 2.5$ and have an active area of
 547 210 m^2 . The two sub-detectors of the tracking system are the pixel detector, closer to the interaction
 548 point, and the strip detector, covering a radius of 0.2 – 1.2 m. The high granularity of the pixels
 549 and micro strips allows to keep the occupancy at acceptable levels, given the high multiplicity of
 550 the tracks ($\sim 1 \text{ MHz/mm}^2$). The silicon detectors and the electronic cables are cooled down to a
 551 temperature of $\sim 10^\circ \text{ C}$. The structure of the tracking system is showed in fig. 3.10.

3.2 CMS detector

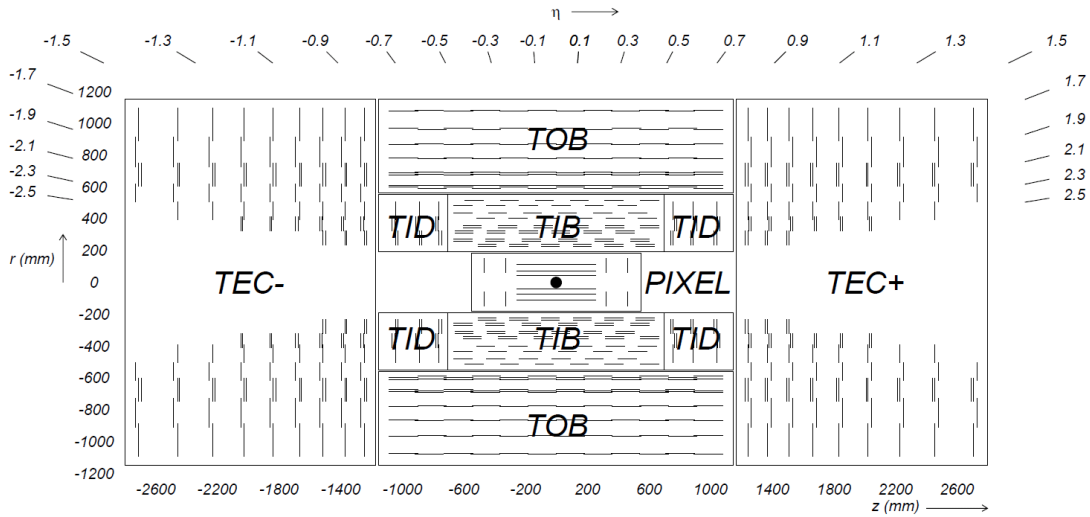


Figure 3.10: The CMS tracking system: the inner pixel detector, close to the interaction point, and the outer strip detector.

552 **3.2.3.1 The pixel detector**

553 The pixel detector is composed by 66 millions of silicon cells, whose dimensions are $100 \times 150 \mu\text{m}^2$,
 554 285 μm of thickness, placed in 1440 modules. Silicon cells are set in three layers in the barrel re-
 555 gion and in two disks at each endcap. Barrel modules are disposed parallel to the magnetic field,
 556 whilst at the endcap they are tilted by about 20°. Pixels allow a spatial resolution of 10 μm in the
 557 transverse plane, and of $\sim 20 \mu\text{m}$ along the longitudinal coordinate. Their reduced size guarantees
 558 an occupancy of 10^{-4} per pixel at each bunch crossing, in high luminosity regime.

559 **3.2.3.2 The strip detector**

560 The strip system is divided in the four-layered tracker inner barrel (TIB), covering a region $20 < r <$
 561 55 cm with respect to the interaction point, the six-layered tracker outer barrel (TOB), located at
 562 $55 < r < 110$ cm, the three tracker inner disks (TID) and the nine tracker endcaps (TEC) at each
 563 cylinder base. Given the lower radiation level at higher radii (and hence a lower occupancy, around
 564 few percent), micro strips are bigger than the pixels. Silicon strips in TIB and TID are 320 μm thick,
 565 10 cm long, and with a pitch ranging from 80 to 120 μm ; strips in TOB and TEC are 25 cm long, with
 566 a different thickness (320 μm for TID, 500 μm for TEC) and pitch (97–184 μm). There are 15148 strip
 567 modules, and 9.3 million readout channels. The strip spatial resolution is about 20 – 50 μm in the
 568 transverse plane and about 200 – 500 μm along the longitudinal coordinate.

569 **3.2.4 The electromagnetic calorimeter**

570 The CMS electromagnetic calorimeter (ECAL, shown in fig. 3.11) [42] is a homogeneous detector
 571 composed by lead tungstate (PbWO_4) scintillating crystals, designed to measure the energy de-
 572 posits of photons and electrons through their electromagnetic showers. PbWO_4 is transparent and
 573 dense (8.3 gr/cm³); it has a fast time response (the 85% of the scintillating light is emitted at every
 574 bunch crossing, namely 24 ns), high scintillating efficiency and radiation resistance; it has a radia-
 575 tion length is $X_0 = 0.89$ cm and a Molière radius of 2.19 cm. The ECAL is divided in the barrel region
 576 ($\eta < 1.479$, at a radius of 1.3 m) and the endcaps ($1.479 < \eta < 3$). The 61200 crystals employed in
 577 the barrel region, whose size is $(22 \times 22) \text{ mm}^2 \times 23$ cm, have a radiation length of $25.8X_0$; the 7324

578 crystals in the endcaps, $28.6 \times 28.6 \text{ mm}^2 \times 22 \text{ cm}$, have a radiation length of $24.7 X_0$. Before the end-
 579 caps, on each side, a pre-shower detector is installed: it is composed by two disks of lead absorber
 580 and two layers of silicon strips, up to a radiation length of $3 X_0$. It has been designed to distinguish
 581 the photons coming from the π^0 decay from the rare Higgs decay $H \rightarrow \gamma\gamma$. The readout and ampli-
 582 fication of the scintillating light, performed by avalanche photodiodes in the barrel and by vacuum
 583 phototriodes in the endcaps, requires a stable temperature of 18° C , mantained by a water cooling
 584 system.

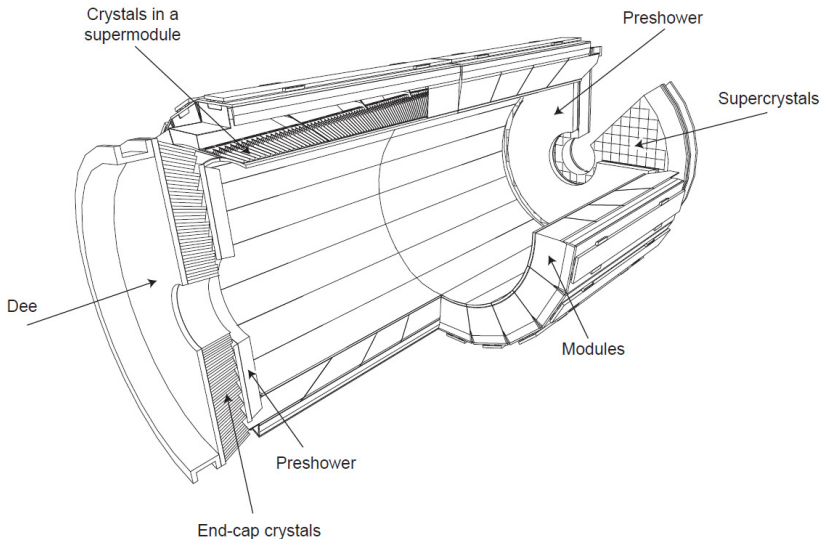


Figure 3.11: The CMS electromagnetic calorimeter.

585 The energy resolution of the calorimeter is parametrized as:

$$\left(\frac{\sigma}{E}\right)^2 = \left(\frac{S}{\sqrt{E}}\right)^2 + \left(\frac{N}{E}\right)^2 + C^2, \quad (3.7)$$

586 where $S = 0.018 \text{ GeV}^{\frac{1}{2}}$ is the stochastic term, $N = 0.04 \text{ GeV}$ is related to noise contribution, and
 587 $C = 0.005$ is a constant term depending on the calibration.

588 3.2.5 The hadronic calorimeter

589 The hadronic calorimeter (HCAL, displayed in fig. 3.12) [43] is a sampling calorimeter, composed by
 590 brass and plastic scintillator layers. It has been designed in order to guarantee a good hermeticity,
 591 allowing to perform a precise measurement of the missing transverse energy. It is located within
 592 the electromagnetic calorimeter and the solenoid, covering a region of $|\eta| < 1.3$ in the barrel, and
 593 $1.3 < |\eta| < 3$ in the endcaps. Brass is non-magnetic and has short interaction length (16.4 cm):
 594 the 60 mm thick absorber layers used in the barrel allow to reach 5.6 interaction lengths at $\eta = 0$
 595 and 10.8 interaction lenghts at $\eta = 1.3$; the 80 mm thick layers in the endcaps reach 11 interaction
 596 lenghts. An additional calorimetric layer has been installed out of the solenoid, in order to reach 11.8
 597 interaction lenghts in the barrel region. The scintillation light, typically in the blue-violet region of
 598 the electromagnetic spectrum, is collected by wavelenght-shifter fibers, translated and amplified
 599 by multi-channel hybrid photodiodes, proportionally to the magnitude of the energy deposits. An
 600 additional hadronic calorimeter has been placed in the forward region, $3 < |\eta| < 5.2$, at 11.2 m from
 601 the interaction point. It has beeen designed to afford the high levels of radiations: it is composed

3.2 CMS detector

602 by 55 mm thick absorber layers of stainless-steel, and quartz fibers, able to detect the Cherenkov
603 scintillating light of the charged particles of the hadronic showering. A longitudinally segmentation
604 allow to distinguish hadronic particles from electromagnetic components. The energy resolution
605 of the hadronic calorimeter is:

$$\left(\frac{\sigma}{E}\right) \approx \frac{a}{\sqrt{E}} + b\%, \quad (3.8)$$

606 where $a = 65\%$ in the barrel region, 85% in the endcaps, 100% in the forward region, and $b = 5\%$.

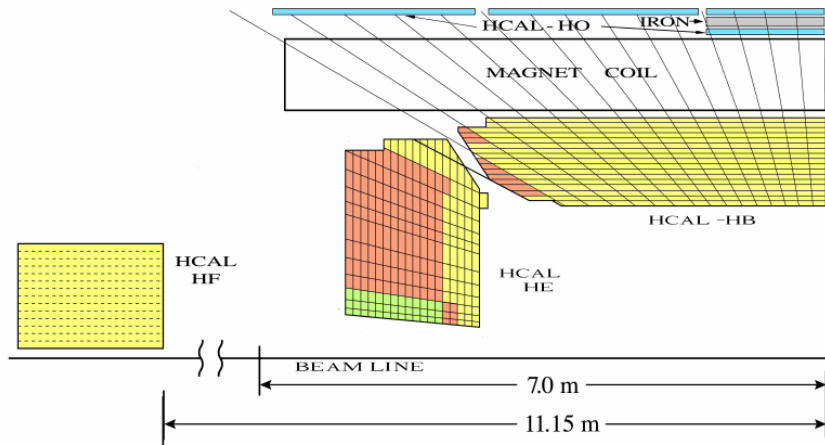


Figure 3.12: The CMS hadronic calorimeter.

607 3.2.6 The muon system

608 The outer system of the CMS experiment consists into gas detectors for identifying muons [44], that
609 are located between the iron return yokes, designed to close the magnetic field generated by the
610 solenoid. In the barrel region, where a smaller number of muons is expected and the magnetic field
611 is less strong, Drift Tubes (DT) detectors are installed. In the endcaps, where the flux of particles is
612 larger, Cathod Strip Chambers (CSC) are used, and disposed in three disks. CSCs are designed to
613 allow faster responses, higher granulatit and radiation resistance. Resistive Plate Chambers (RPC)
614 are installed both in the barrel and in the endcaps as additional triggering system. The geometry of
615 the muon system is showed in fig. 3.13; it consists of 250 DTs, 530 CSCs, 610 RPCs, and it covers a
616 region $|\eta| < 2.4$.

617 3.2.6.1 The Drift Tubes

618 Drift Tube detectors cover a region of $|\eta| < 1.2$ and are arranged in four stations, segmented along
619 the beam line in five wheels. The basic element of the detector is the cell, that has a size $42 \times 13 \text{ mm}^2$.
620 Each cell is filled with a gas mixture (85% argon, 15% CO_2), in which the process of ionization takes
621 places; the ionization electrons drift from the $50 \mu\text{m}$ thick steel anodic wire, in the center of the cell,
622 towards the aluminium cathodic strips, located at its edge. Additional electrodes on the surface of
623 the cells allows to shape the electric field, in order to make the drift speed of the electrons uniform:
624 the muon position is then extrapolated from the measurement of the drift time. Every station is
625 composed by three cells superlayers. In the inner and the outer superlayers, the cells are oriented
626 such in a way that the anodic wire is located along the z axis, in order to measure the ϕ coordinate.
627 In the intermediate superlayer, wires are parallel to the radial coordinate, hence they can measure

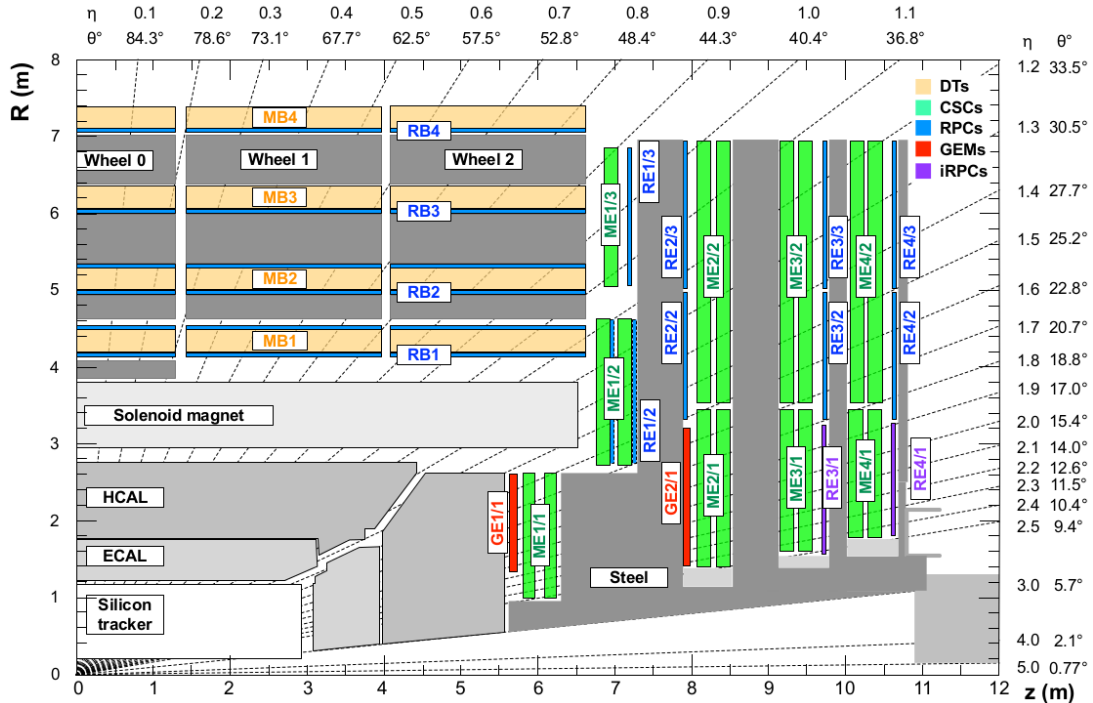


Figure 3.13: Section of CMS detector, in the plane rz , parallel to the beamline, that emphasizes the location of the muon detectors, in particular: Drift Tubes (DT, in yellow); Cathode Strip Chambers (CSC, in green); Resistive Plate Chambers (RPC, in blue).

the z position. The spatial resolution of the system is $100\ \mu\text{m}$ in the $r\phi$ plane, 1 mrad in the ϕ coordinate, and $150\ \mu\text{m}$ in the longitudinal z coordinate.

3.2.6.2 The Cathode Strip Chambers

Cathode Strip Chambers cover a region of $0.9 < |\eta| < 2.4$, overlapping with the DT in the pseudorapidity range $0.9 < |\eta| < 1.2$. The anodic wires inside each CSC are located into six planes, with the aim of measuring the radial coordinate; the wire planes are perpendicularly crossed by cathodic strips, disposed along the radial direction to measure the ϕ coordinate. Ionization electrons produced by muons passing through the gas mixture in the chambers migrate towards the anode, inducing a charge distribution on the cathodes, from which the azimuthal coordinate can be reconstructed. The spatial resolution in the r coordinate is $200\ \mu\text{m}$, and it is $75 - 150\ \mu\text{m}$ in the $r\phi$ plane. CSCs are arranged in four disks and in three concentric rings.

3.2.6.3 The Resistive Plate Chambers

Resistive Plate Chambers (RPC) are located both in the barrel (disposed in six layers) and in the endcap region (three layers), up to a pseudorapidity of $|\eta| < 1.6$. These gas detectors are charged at very high voltages, in order to work in the avalanche ionization mode. The plastic resistive plates are equipped with readout strips. The spatial resolution of the detector is low (1-2 cm), but the fast timing response (2-3 ns) and good time resolution (1 ns) allow to employ RPCs as an additional triggering system and to profit of a precise measurement of the bunch-crossing time.

646 3.2.7 The trigger system and data acquisition

647 The CMS trigger system [45] has been designed considering the high instantaneous luminosity, such
648 that it can provide a fast response and it allows to reduce the nominal event rate of 40 MHz in proton
649 proton collision. The complexity of the CMS detector and the very high number of readout channels
650 result into a huge amount of data per event, approaching the order of few MB per bunch crossing,
651 hence 40 TB per second. The handling and the recording of data is currently limited at the order of
652 ~ 100 Hz; hence, applying online selections to skim the events that are going to be written on tape,
653 without rejecting interesting signals of hard processes and rare phenomena becomes a crucial and
654 challenging point for every data analysis. Events are filtered by trigger selections at different levels:
655 the Level-1 (L1) trigger is an hardware device, that allows to reduce the event rate from 40 MHz to
656 the order of 100 kHz; the High Level Trigger (HLT) is a set of software algorithms that skims the event
657 rate down to few hundred Hz. Once the trigger decisions are taken, the final events are handled by
658 the Data Acquisition System (DAQ), that collects the informations coming from the subdetectors
659 and sends them to the storage devices.

660 3.2.7.1 The Level-1 trigger

661 The L1 trigger is an hardware device composed by customized electronics, and it accesses the in-
662 formations coming from the calorimeters and the muon system, while the tracker is not considered
663 given the excessively large bandwidth needed by its readout channels. The L1 trigger perform a
664 first raw local reconstruction of each object, called “trigger primitive”. The L1 trigger is composed
665 by three subsystems: the calorimeter trigger, the muon trigger (divided in three independent sub-
666 subsystems for each muon subdetector, namely DTs, RPCs and CSCs), and the global trigger, that
667 combines the informations of the former subsystems. The best quality trigger primitives recon-
668 structed by the calorimeter and muon detectors (namely, roughly reconstructed electrons, photons,
669 muons, jets, jets coming from the hadronic decays of tau leptons, and missing energy) are handled
670 by the global trigger, who takes the decision of discarding or keeping the event every $3.2 \mu\text{s}$. The
671 simplest trigger selections require the presence of a single object, whose energy or transverse mo-
672 mentum is higher than a certain threshold; more complicated triggers involve multiple objects or
673 geometrical selections, that can be performed in parallel up to 128 simultaneous requirements.

674 3.2.7.2 The High Level Trigger

675 The HLT skims the L1 output rate down to few hundreds of Hz by applying a set of algorithms imple-
676 mented in the same software used for the offline analysis, consisting in the event reconstructions
677 exploiting the whole informations coming from all subdetectors. The computing time is still a cru-
678 cial factor, hence selections applied to HLT physics objects are generally less accurate than those of
679 the offline analysis; furthermore, HLT can discard the event even before its full reconstruction (*i.e.*
680 by looking only at certain region of the detectors). Events filtered by the HLT decisions are assigned
681 to precise trigger paths and recorded in precise categories of datasets.

682 3.2.7.3 Data acquisition, computing and storage

683 The DAQ system deals with the storage, transfer and handling of the data collected by CMS; it also
684 supports and stores the data simulations and calibrations of the subdetectors. The CMS computa-
685 tional resources are located in worldwide distributed data nodes, called Tiers. The CMS software
686 (CMSSW) is based on an object oriented architecture (mainly C++). The basic unity of every data,
687 both real and simulated ones, is the Event, that could contain very rough informations (RAW data
688 format) or higher level refined objects (AOD, Analysis Object Data) where all the calibrations and

689 corrections needed to properly deal with the final physics objects are already in place. Data are
 690 handled by C++ or python modules, and the outputs are written in ROOT [46] files.

691 **3.2.8 Particle Flow event reconstruction**

692 The particle flow (PF) algorithm [47] aims at identifying and reconstructing each particle produced
 693 by the proton-proton collisions, combining the informations coming from all the CMS subdetec-
 694 tors. It is particularly suitable to improve the reconstruction of jets, missing transverse momentum
 695 (used to identify neutrinos) and hadronically decaying tau leptons.
 696 The association of the informations is performed at different stages. The reconstruction of the
 697 charged particles in the silicon detector is performed with an iterative algorithm, and the recon-
 698 structed object is called a tracker track. Then, a clustering algorithm is performed to collect and
 699 combine the energy deposits in the calorimeters, in such a way to distinguish neutral from charged
 700 particles, reconstruct their directions, improve the energy measurement of the very energetic charged
 701 particles, whose tracks are less bended by the magnet and hence less precisely determined. The last
 702 informations are provided by the hits collected in the muon system. The three sets of reconstruc-
 703 tions are then combined with a link algorithm, that aims at associating tracker tracks to calorime-
 704 ter clusters and muon hits with geometrical criteria. A track in the silicon detector is linked to a
 705 calorimeter cluster if the extrapolated position lies in the cluster itself. Similarly, clusters in differ-
 706 ent calorimeters are linked when the position in the more granular calorimeter (*i.e.* ECAL) lies in
 707 the envelope of the clusters in the less granular calorimeter (*i.e.* HCAL). The decision of linking a
 708 tracker track to a muon track is based on the χ^2 of a global fit between the two tracks.
 709 The particle flow algorithm then interprets the collected and linked informations as different par-
 710 ticles. Muons are identified by the combination of a track in the silicon detectors and a track in the
 711 muon chambers. Photons are determined directly by ECAL clusters. Electrons energies and posi-
 712 tions are measured by ECAL clusters, linked to a corresponding tracker track, and considering all
 713 the energy clusters produced by the bremsstrahlung photons radiated while interacting with the
 714 material. The hadrons are identified by the tracks (if charged) linked to the corresponding ECAL
 715 and HCAL clusters. The hadron energy resolution, 10% at 100 GeV combining ECAL and HCAL, is
 716 such that neutral hadrons can be distinguished as an energy calorimetric excess when overlapped
 717 by a charged hadron occupying the same calorimetric towers. Finally, the missing transverse mo-
 718 mentum is defined as the negative sum of the transverse momenta of all the particles identified by
 719 the PF algorithm.

720

721 **3.2.9 Physics objects**

722 **3.2.9.1 Track reconstruction**

723 The reconstruction of the trajectories of the charged particles passing through the CMS detector is
 724 performed by multiple iterations of the Combined Track Finder algorithm, that is based on a Kalman
 725 filter approach [48]; given the high multiplicity of particles produced at each bunch crossing and the
 726 multiple scatterings throughout the detector materials, this represents a challenging task. The CTF
 727 algorithm builds a track starting from the so-called seeds, namely triplets of hits collected in the
 728 pixel detector inner layers, or couples of hits if the track originates from the interaction point. The
 729 initial guess of the track given by the seeds is then extrapolated to the outer layers: if other hits are
 730 found to be compatible with the trajectory hypothesis (χ^2 -based hypothesis test), they are added to
 731 the track. Once the outer layers are reached, another reconstruction is performed backward, in or-
 732 der to clean the track from spurious hits and enhance the tracking efficiency. The final collected hits

3.2 CMS detector

733 are re-fitted with Kalman Filter and more precise algorithms, in order to improve the quality of the
734 measurement. If two tracks share more than a half of their hits, the worst quality track is rejected.
735 The track reconstruction efficiency for particles with $p_T > 0.9$ GeV is 94% in the barrel and 85% of
736 the endcap region [41].

737

738 3.2.9.2 Vertices reconstruction

739 The reconstruction of the vertices at each bunch crossing is performed in two steps. Primary ver-
740 tices are originating from the proton proton collisions, whilst secondary vertices are due to long-
741 lived particles (heavy quarks). The starting point of the procedure is clustering the reconstructed
742 tracks originating from the primary vertex; the decision is taken by the deterministic annealing al-
743 gorithm [49], taking as input the longitudinal impact parameter. The algorithm allows to distinguish
744 vertices separated down to 1 mm. The second step is run by the adaptive vertex fitter [50], that mea-
745 sures the position of the vertex for the set of tracks selected. The algorithm is based on an iterative
746 re-weighted Kalman filter, that down-weights the wrongly associated tracks not compatible with
747 the considered vertex. The primary vertex is selected as the vertex where the sum of the p_T^2 of the
748 associated tracks is the highest. The resolution is 10-40 μm in the (r, ϕ) plane, and 15-50 μm in the
749 longitudinal coordinate.

750 3.2.9.3 Electrons and photons reconstruction

751 Electrons are reconstructed [51] combining a track with the energy deposits clustered in the ECAL,
752 due to the showering of the electron through the detector and the emission of bremsstrahlung pho-
753 tons. The combination can proceed both from the silicon detector in the outgoing direction and in
754 the opposite way: the tracker seeding as starting point is suitable for low energy electrons, whose
755 trajectories are less bended and hence more accurately measured by the tracker system; the group-
756 ing of ECAL clusters (called superclusters) followed by a consecutive track extrapolation, performed
757 by taking into account the electron interaction with the detector material, is more efficient in case of
758 high energetic electrons, due to the higher resolution of the ECAL scintillating crystals. A Gaussian-
759 sum filter algorithm (GSF) [52] allows to properly take into account the effects of the bremsstrahlung
760 radiation, that is distributed not as a single Gaussian (standard Kalman filters) but rather as a sum
761 of Gaussian functions.

762 The identification of an electron relies on three groups of variables: observables combining mea-
763 surement performed in the silicon detectors and in the calorimeter; purely calorimetric observ-
764 ables; purely tracking informations. Different selections are used for electron candidates found in
765 the barrel and in the endcaps, and they can vary from loose criteria (high detection efficiency but
766 less purity, namely more contamination from object misidentified as electrons) to tight criteria.
767 Data and Monte Carlo simulations reproducing Z , ν and J/Ψ decays in e^+e^- are used to study the
768 optimal working points, each one targeting at a different purity.

769 The electron energy is determined correcting the raw energy measurement of the ECAL superclus-
770 ters by taking into account the effects of the losses due to radiation or gaps between the calorimeter
771 modules, and the pile-up contribution. The electron momentum resolution has been measured in
772 $Z \rightarrow e^+e^-$ decays in Run 1 LHC data, and it varies from 1.7 to 4.5% depending on the pseudora-
773 pidity range [53]. The electron isolation variable is defined as the p_T sum of the charged and neutral
774 particles laying in a cone of $\Delta R = 0.3$ around the electron trajectory, divided by the transverse mo-

775 momentum of the electron:

$$I_{\Delta R=0.3}^e = \frac{\sum_{\text{char. hadrons}} p_T + \max[0, \sum_{\text{neut. hadrons}} p_T + \sum_{\text{photons}} p_T - 0.5 \sum_{\text{pile-up char. hadrons}} p_T]}{p_T^e}; \quad (3.9)$$

776 the contribution of the pile-up charged particles is removed. The isolation variable is used to dis-
 777 tinguish electrons coming from the leptonic decays of electroweak bosons (low $I_{\Delta R=0.3}^e$) from elec-
 778 trons coming from the decays of heavy fermions, when they are more likely produced in association
 779 with light flavour jets and hence topologically close to calorimetric deposits due to hadrons (high
 780 $I_{\Delta R=0.3}^e$).

781 Photons are reconstructed with the ECAL clusters only. Given their importance in the discovery of
 782 the Higgs boson, dedicated studies have been performed both in data and in Monte Carlo simula-
 783 tions reproducing the $H \rightarrow \gamma\gamma$ process. Particular care has been taken in the treatment of the photon
 784 conversions into electron-positron pairs while interacting with the tracker detector. Dedicated se-
 785 lections allow to define different photon identification working points. Similarly to the case of the
 786 electrons, the photon isolation variable can be defined. The photon energy resolution varies from
 787 1% to 3%, depending on the η range [54].

788 3.2.9.4 Muon reconstruction

789 A muon candidate can be built exploiting the hits collected in the silicon tracker (track) and in the
 790 muon system (standalone muon) [55]. Each muon subdetector (DTs, RPCs and CSCs) performs a
 791 local reconstruction of the candidate; the informations from the three muon chambers are com-
 792 bined with a Kalman filter approach.

793 Three different strategies are adopted to define a muon candidate in the CMS detector. A stan-
 794 dalone muon is reconstructed by only using the local reconstruction in the muon chambers. A
 795 tracker muon is built starting from a track in the silicon detector, that is extrapolated up to the muon
 796 chambers, taking into account the multiple scattering and the energy loss through the material.
 797 The tracker muon is defined if at least one segment, *i.e.* a short track built with CSCs or DTs hits,
 798 is matched to the starting track. This technique is the most efficient for the reconstruction of low
 799 energetic muons. A global muon is built starting from a standalone muon, and then its trajectory is
 800 extrapolated towards the inner layer of the silicon detector and eventually matched to a track; this
 801 approach is suitable for highly energetic muons ($p_T > 200$ GeV).

802 Different algorithms are used to assign the momentum to the muon candidate, in order to mitigate
 803 the effects of bremsstrahlung, that becomes significant when the muon approaches an energy of the
 804 order of 1 TeV. The radiated photons generate spurious hits in the chambers and larger occupancy,
 805 significantly deteriorating the momentum measurement.

806 Starting from 2016 Run, the muon reconstruction takes into account the Alignment Position Er-
 807 rors, namely the uncertainties due to the position of the muon chambers with respect to the sil-
 808 icon detectors. The final resolution on the muon momentum measurement depends on the p_T
 809 and η of the candidate, and ranges from 1% for very low momenta, up to $\sim 7\%$ ($|\eta| < 0.9$) – 10%
 810 ($1.2 < |\eta| < 2.4$) [56].

811 The muon isolation $I_{\Delta R=0.4}^\mu$ is defined similarly to the electron isolation, but by taking into account
 812 a larger cone $\Delta R = 0.4$ around the muon direction.

813 3.2.9.5 Jet reconstruction

814 The nature of the strong interaction is such that coloured partons, namely quarks and gluons, are
 815 forced to aggregate to form a color-neutral hadron, in the process called hadronization. Therefore,

3.2 CMS detector

816 partons cannot be observed as free particles in a detector, but rather as collimated jets of hadronic
817 particles.

818 Jets are reconstructed starting by the PF candidates in the event. The charged hadron subtraction
819 algorithm (CHS) removes candidates not associated to the primary vertex in order to remove con-
820 tributions from pileup [57]. The remaining particles are used as input to jet clustering algorithms to
821 reconstruct particle-flow jets. The jets are clustered using the FASTJET package [?] with the anti- k_T
822 jet sequential clustering algorithm [58]. A sequential clustering algorithm is designed in order to be
823 infrared and collinear safe, namely, if the final state particles undergo a soft emission or a collinear
824 gluon splitting, the number and shapes of the jets should not change. The stating point of a sequen-
825 tial clustering algorithm is the definition of the distances bewtween two particles i and j , and the
826 distance of a given particle i from the beam-spot B :

$$d_{ij} = \min(p_{T,i}^{2a} p_{T,j}^{2a}) \frac{R_{ij}^2}{R^2}, \quad (3.10)$$
$$d_{iB} = p_{T,i}^{2a}$$

827 where $p_{T(i,j)}$ are the transverse momenta of the particles, $R_{ij}^2 = (y_i - y_j)^2 + (\phi_i - \phi_j)^2$ is the angular
828 distance between the particles, a is an exponent depending on the clustering algorithm chosen,
829 and R is the clustering parameter. The algorithm then operates as follows:

- 830 • it computes all the possible combination of distances d_{ij} and d_{iB} and it finds the minimum;
- 831 • if the minimum is d_{ij} , the four-momenta of the particles i and j are summed up in one can-
832 didate $i\bar{j}$; i and j are removed from the list of candidates, the distances are updated, and the
833 algorithm proceeds to re-calculate all the possible remaining d_{ij} ;
- 834 • the clustering stops when the smallest quantity is d_{iB} : i particle is defined as one jet, and it
835 is removed from the list of particles;
- 836 • this process is repeated until all the particles are assigned to a jet, that must be separated from
837 another jet at least by a distance $R_{ij} > R$.

838 In case of the anti- k_T algorithm, $a = -1$. It tends to cluster high p_T particles first, since the hard
839 term dominates d_{ij} in equation 3.10. Since the soft particles have lower impacts, the shape of the
840 jet is not sensitive to the soft radiation and rather stable against the softer pile-up contributions.
841 In this analysis, clustering parameters of $R = 0.8$ and $R = 0.4$ will be used to define the “fat”-jets or
842 AK8 jets, and the “standard”-jets or AK4 jets). In order to avoid double-counting of PF candidates,
843 AK4 jets are considered only if the angular separation from the leading AK8 jet is larger than $\Delta R >$
844 0.8.

845 Since the detector response to different particles is not linear, particular care should be taken in the
846 assignement of the measured momentum of the clustered jet to the corresponding true value of the
847 original parton [59]. A set of jet energy corrections (JECs) are applied sequentially and with a fixed
848 order. Each correction constists in a rescaling of the jet four-momentum, and it takes into account
849 different effects that are factorizes.

- 850 • The L1 JECs remove the effect of the pile-up; they consist into an offset correction of the jet
851 p_T . They are determined from Monte Carlo (MC) simulations of dijet events produced by
852 strong interaction with and without pile-up events on top, and parametrized as a function of
853 kinematical parameters (jet area, pseudorapidity and p_T) and of the average p_T density per
854 unit area ρ . Residual difference between data and the detector simulation are evaluated in
855 data collected with a random trigger, called zero bias, applying the only requirement of the

beam crossing happening. Pile-up offset corrections are displayed in fig. 3.14 (top left), as a function of the jet pseudorapidity.

- The simulated response of the detector is not uniform over jet p_T and η . This effect is mitigated by the L2L3 MC-truth corrections. They are calculated in MC simulations of dijet events by taking into account the discrepancy between the reconstructed p_T of the jet and the true p_T at particle level, as a function of jet p_T and η . L2L3 scale factors describing the simulated jet response are reported in fig. 3.14 (top right), as a function of the jet pseudorapidity.
- The small data-MC discrepancies ($\sim 1\%$) left after applying the previous set of JECs are corrected by the L2 and L3 residual corrections. The L2Residuals are calculated in dijet events, as a function of p_T . The L3Residuals are calculated in $Z \rightarrow (\mu\mu, ee) + \text{jet}$ events, photon + jet events and multijet events, as a function of η and p_T , with the p_T -balancing method [59]. Data-MC scale factors for L2L3Residuals are displayed in fig. 3.14 (bottom), as a function of the jet η and p_T .
- An optional correction, not used in this analysis, is the L5 flavor-dependent correction, that is extracted from MC simulations.

Each jet energy correction is determined with an uncertainty, and reported in fig. 3.15 for 2015 data, as a function of p_T and η of the jet. The total uncertainty for jets with p_T larger than 30 GeV (100 GeV) is smaller than 3% (1%) in the barrel, and up to 5% (3%) in the endcaps.

An additional effect that must be taken in account is the discrepancy in the jet energy resolution (JER) observed in data and in Monte Carlo samples. A smearing procedure is applied in MC simulations (described in detail in sec. 4.2.6), in order to restore a better agreement. Jet energy resolutions in Monte Carlo simulations are displayed in fig. 3.16 (top), as a function of the jet p_T and the average number μ of reconstructed primary vertices, considering central (left) and forward (right) jets. The resolution is stable against the pile-up for jet $p_T > 100$ GeV, and it ranges from 10% at 100 GeV, down to 4% at 1 TeV. In fig. 3.16 (top). In fig. 3.16 (bottom), data-MC smearing scale factors are reported as a function of η .

3.2.9.6 Tau reconstruction

Tau leptons have a very small lifetime ($\sim 3 \times 10^{-13}$ s), hence they decay before reaching the pixel detector and they can only be reconstructed through their decay products. Approximatively 60% of the times, τ leptons decay in hadrons, hence they are reconstructed as small collimated jets in the CMS detector. The main decay modes of the hadronic tau, τ_h , are one or three charged mesons (mainly π^\pm), also in association with a π^0 decaying in a couple of photons, and a τ neutrino. Hence, photons and charged hadrons are the main ingredients of dedicated algorithms to perform the τ_h reconstruction and identification, in order to distinguish them from quark and gluon-initiated jets. The main CMS τ_h reconstruction algorithm, Hadron Plus Strips (HPS) [60], is particle-flow based. HPS builds the tau candidate from a PF jet, clustered with the anti- k_T algorithm with $R = 0.5$, and it reconstructs the $\pi^0 \rightarrow \gamma\gamma$ decays within the jet cone, by taking into account the photon conversions in the silicon detector. The exploitation of the PF informations is such that the HPS algorithm shows stable performances in the reconstruction of the τ_h energy as a function of the energy itself. The τ_h candidate is required to be isolated, namely no energy deposits other than the τ decay products should be present in the tau cone. Depending on the low threshold set to consider the surrounding particles as included in the cone, different isolation working points can be defined. With the looser working point, the probability of misidentifying a quark or gluon jet as a tau is around 1% [60].

3.2 CMS detector

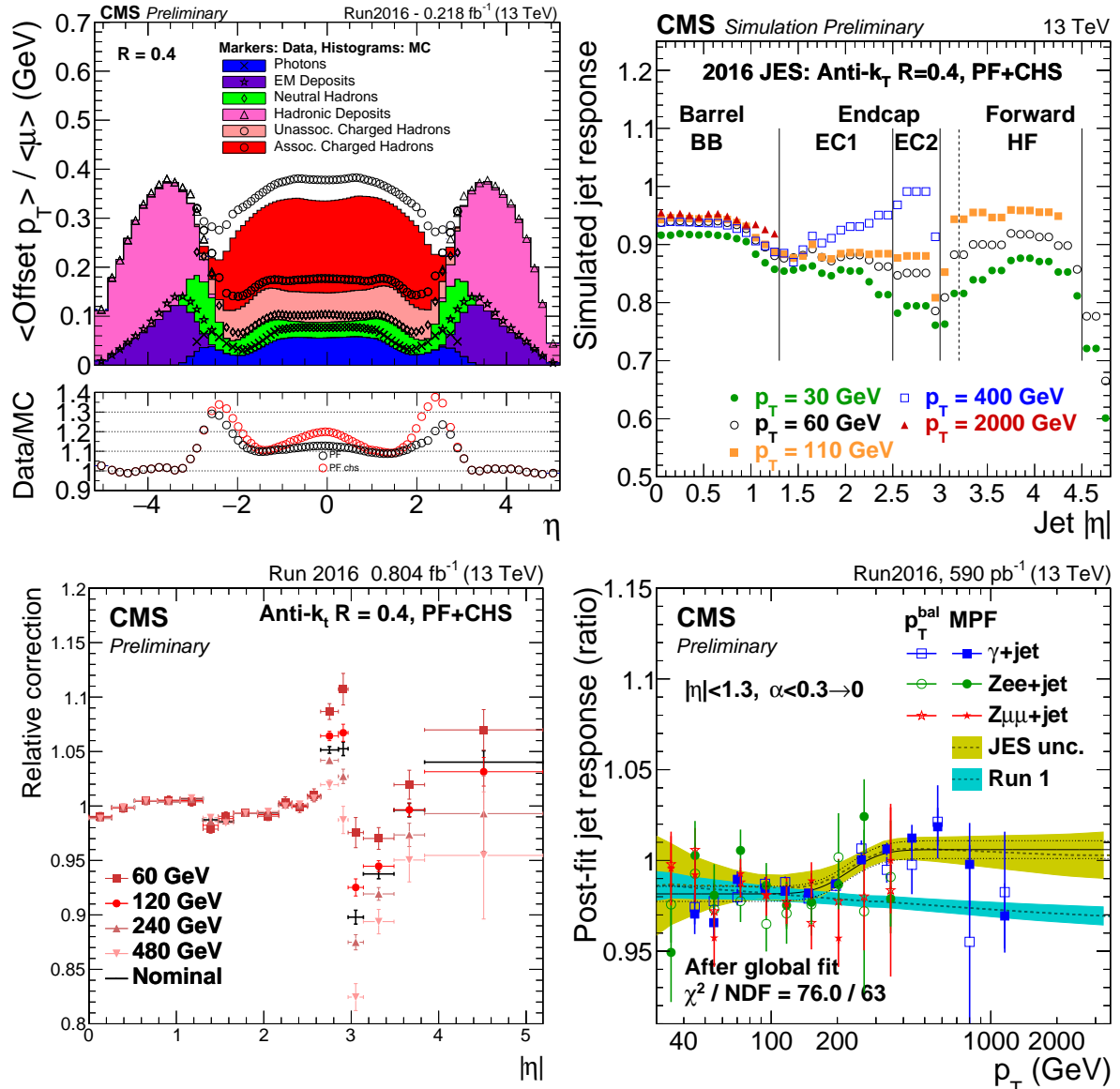


Figure 3.14: Top left: average p_T offset due to additional pile-up events, measured both in data and in MC simulations, as a function of the jet pseudorapidity. Top right: simulated jet response (L2L3 MC-truth corrections), as a function of the jet pseudorapidity. Bottom left: L2L3 residual data-MC corrections, evaluated on dijet events, as a function of the jet η . Bottom right: L2L3 residual data-MC corrections, evaluated on dijet and $Z/\gamma + \text{jet}$ events, as a function of the jet p_T .

3.2.9.7 b-jets tagging

The bottom quark plays a fundamental role in numerous standard model processes, *i.e.* the physics related to the top quark (whose decay into a W and a b-quark with a branching fraction of 100%) and the Higgs boson (decaying into $b\bar{b}$ with a branching fraction $\sim 60\%$). Many algorithms have been exploited by the CMS collaboration, with the aim of distinguishing a b-quark initiated jet and jets originating from light quarks or gluons [61]. The most remarkable feature of the b-quark is the long lifetime (~ 1.5 ps), that has the experimental consequence of a displaced decays (few mm) with respect to the primary vertex. The direct leptonic decays of the b-quark (into μ and e) or the cascade

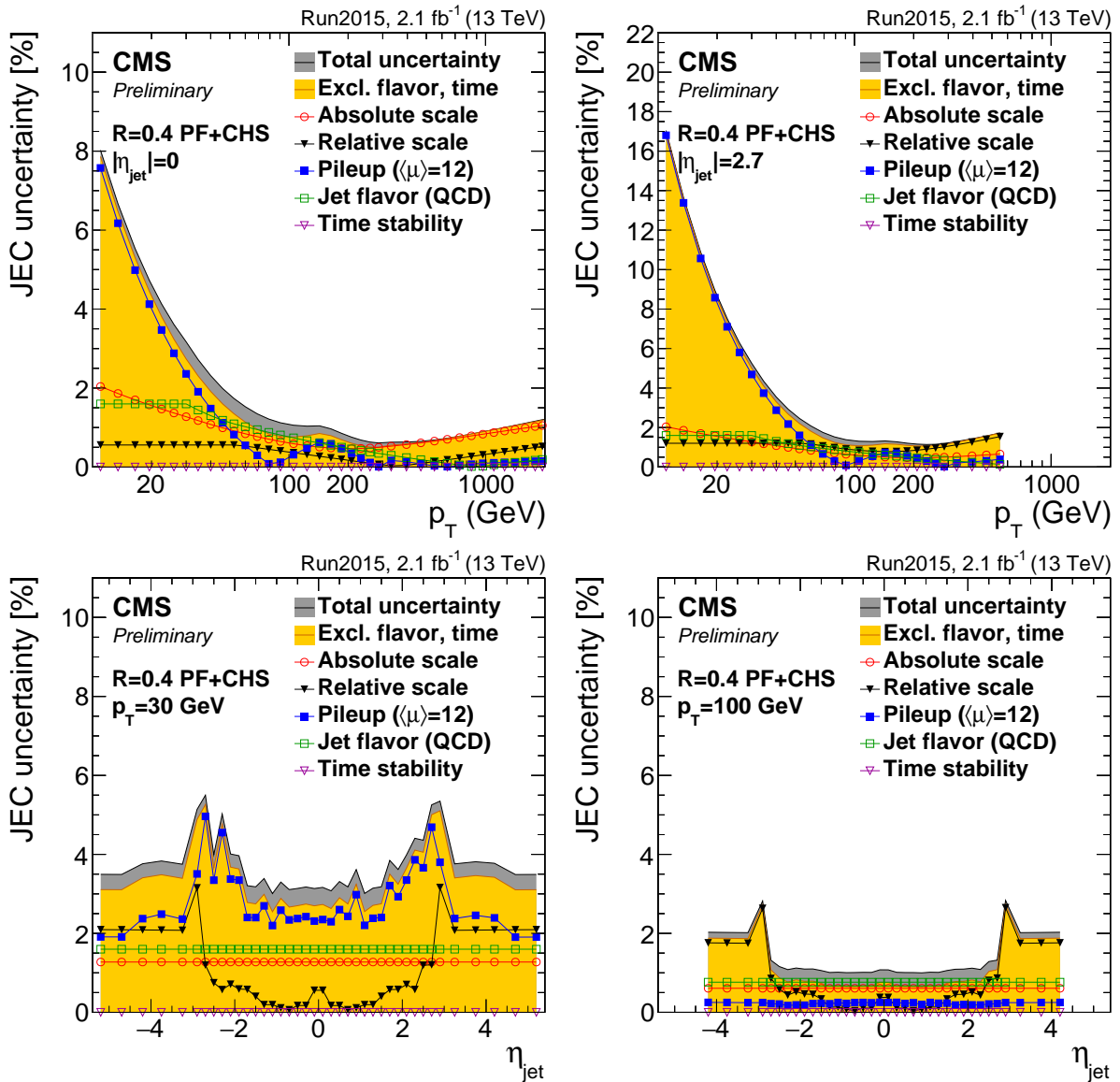


Figure 3.15: Jet energy corrections uncertainties, as a function of jet p_T (top) and η (bottom), calculated in 2015 data. The yellow histograms report the convolution of the uncertainties applied in the analysis.

907 leptonic decays involving c-quarks give an additional handle to its identification.
 908 Given the high spatial resolution of the silicon detector, track reconstruction is a key point of the
 909 b-tagging procedure. Tracks inside a jet candidate must satisfy criteria related not only to their
 910 quality but also on their distance from the interaction point. The track impact parameter is the dis-
 911 tance between the primary vertex and the coordinate of closest approach. Tracks that are too far
 912 from the interaction point are discarded, in order to suppress the pile-up contributions. The Com-
 913 bine Secondary Vertex (CSV) algorithm [62] sorts jet candidates in categories, based on the number
 914 of reconstructed secondary vertices (one reconstructed secondary vertex, no vertex but two tracks
 915 with high impact parameters, and the remaining cases). A multivariate approach allows to train the
 916 algorithm over the categories, considering as discriminating variables both tracking informations
 917 (numbers and properties of the tracks) and their relations with the secondary vertex reconstruction

3.2 CMS detector

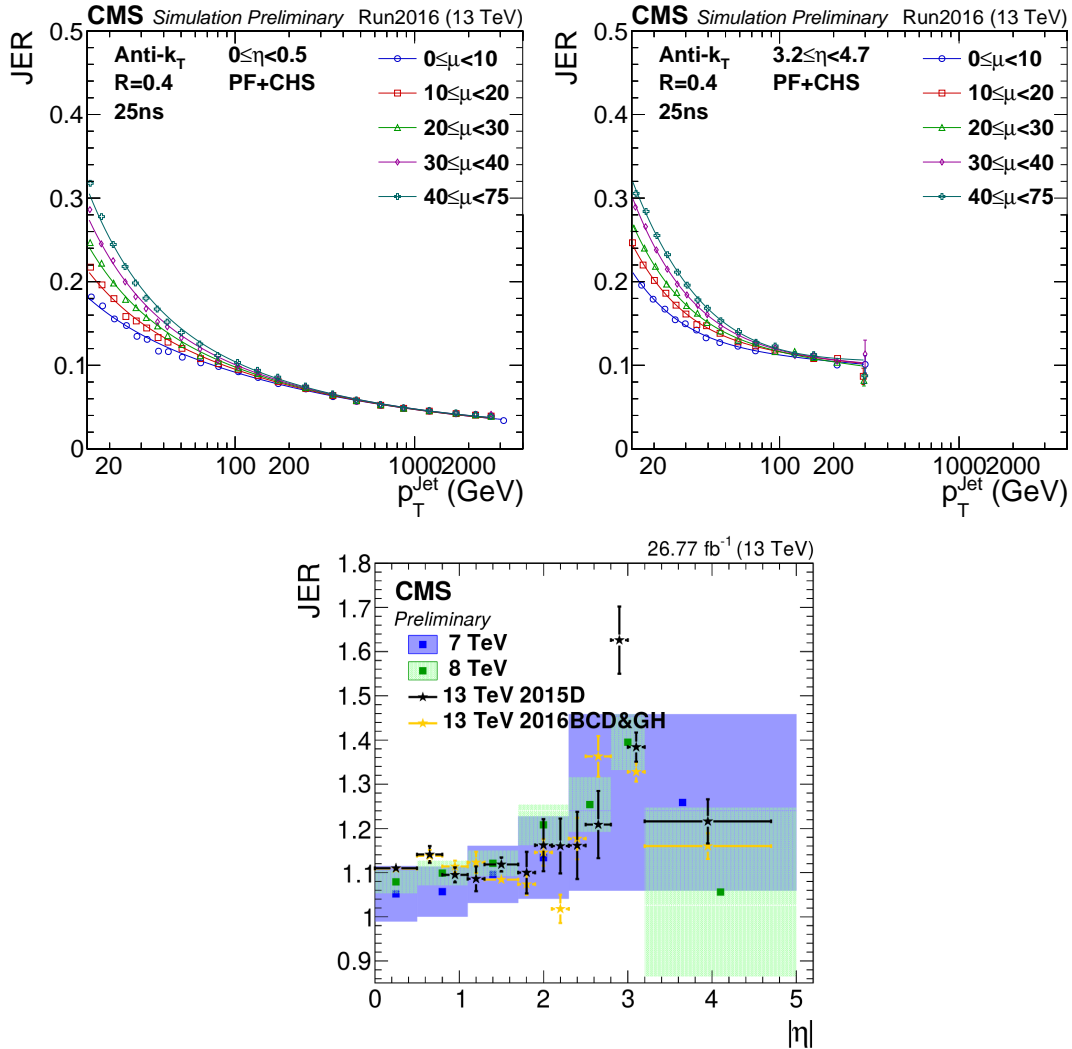


Figure 3.16: Top: jet energy resolution in MC simulations, as a function of the jet p_T . Different curves represent a different average number of primary vertices per event (μ). Bottom: data-MC scale factors, as a function of the jet η , measured in 2016 data (yellow dots).

918 (impact parameters; angular, linear, 2D and 3D distances of the vertex from the tracks and the jet
919 axis, and the invariant mass of the charged particles associated to the secondary vertex).
920 By tuning the different selections, working points with different efficiencies have been set. The loose
921 working point, used in this analysis, has a 90% signal efficiency and a 40% misidentification rate.
922 The b-tagging efficiency is different in data and in simulations. Multiplicative scale factors are cal-
923 culated in events enriched in b-quark jets.

924

925 3.2.9.8 Missing transverse energy reconstruction

926 Neutrinos can interact with the other particles only via the electroweak interactions; hence, when a
927 neutrino is produced in the proton-proton collisions, it passes through the CMS experiment, unde-
928 tected. Its only experimental signature is the momentum imbalance (\vec{p}_T^{miss}) in the transverse plane
929 $r\phi$. The magnitude of \vec{p}_T^{miss} vector is also called missing transverse energy, E_T^{miss} . Given its defi-

930 nition, it is evident that E_T^{miss} is a delicate variable to deal with, since it depends on all the other
 931 objects, on their imperfect measurements, on the detector noise and the pile-up events.

932 The PF E_T^{miss} is the negative sum of the transverse momenta of the PF candidates reconstructed in
 933 the event. Inefficiencies in the tracker reconstruction and non-linear responses of the calorimeters
 934 can be corrected by propagating the jet energy corrections to \vec{p}_T^{miss} [63]:

$$\vec{p}_T^{\text{miss,corr}} = \vec{p}_T^{\text{miss}} - \sum_{j \in \text{jets}} (\vec{p}_{T,j}^{\text{corr}} - \vec{p}_{T,j}^{\text{raw}}), \quad (3.11)$$

935 where "corr" ("raw") is related to corrected (raw) p_T of the considered jet. This correction is known
 936 as the "Type-I" correction to E_T^{miss} . Jets included in the calculation are AK4 with CHS algorithm ap-
 937 plied to remove the pile-up contribution, they must have $p_T > 15$ GeV and less than 90% of their
 938 energy deposited in the electromagnetic calorimeter. If a muon lies in the jet cone, it is subtracted
 939 from the jet and added after the p_T correction. A similar correction is performed to correct \vec{p}_T^{miss} at
 940 trigger level; in this case, a jet p_T threshold of 35 GeV is chosen.

941 The E_T^{miss} uncertainty depends on the topology of the final state. It is calculated per-event by fac-
 942 torizing \vec{p}_T^{miss} in components: electrons, photons, muons, taus, jets, jets with $p_T < 10$ GeV and all
 943 the remaining PF candidates that are not clustered inside jets, called unclustered energy. The mo-
 944 mentum of every object is varied within its unvertainties (namely, the energy scale and resolution),
 945 and the effects are propagated to \vec{p}_T^{miss} . The most significant contributions in the unclustered en-
 946 ergy is due to neutral PF hadrons and hadrons reconstructed in HF. The effects related to jet energy
 947 scale and unclustered energy scale are measured on simulation, in events with a top and an anti-top
 948 quarks, and amounts to 5% and 30% [63].

949

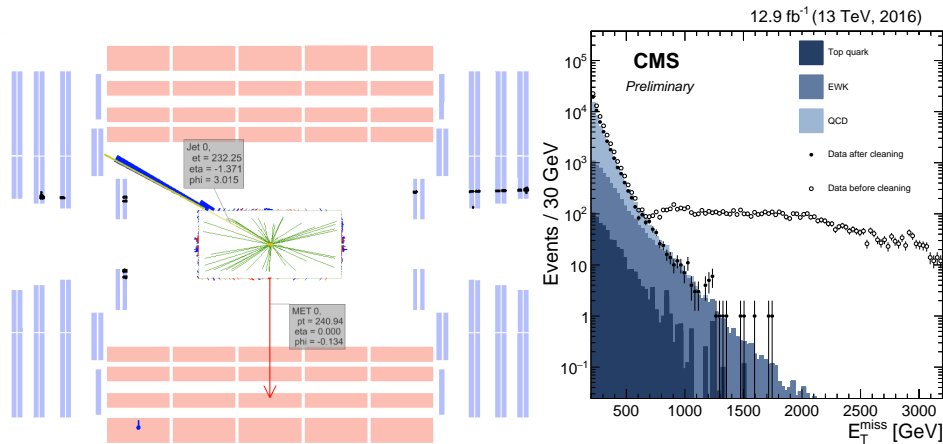


Figure 3.17: Top: event display of beam halo particles hitting the CSC detector. Bottom: comparison of data and simulations (histograms) when di-jet events are selected, before (open markers) and after (filled markers) anomalous E_T^{miss} cleaning algorithms have been applied on data.

950 Many instrumental effects can give rise to anomalous E_T^{miss} determination: they have been studied
 951 in detail during Run1 [64,65] and Run2 [63], and they are mainly caused by ECAL and HCAL. In ECAL,
 952 anomalous \vec{p}_T^{miss} is caused by particles hitting the sensors of the photodetectors, or by beam halo
 953 particles (namely, particles produced in spurious proton interactions before reaching the interac-
 954 tion point in the detector) showering inside the calorimeter, or by losses due to ECAL dead cells. An
 955 event display representing beam halo muons hitting the CSC detector is showed in fig. 3.17 (top).
 956 In HCAL, spurious \vec{p}_T^{miss} can be related to noise in the hybrid photodiodes and readout frontend. In

3.2 CMS detector

HF missing p_T can be related to particles lost in the light guides and photomultipliers. Anomalous E_T^{miss} can be produced by low quality muon tracks, that are not linked to segments reconstructed in the muon chambers by the PF algorithm. These tracks are then classified as charged hadrons, taken into account in the \vec{p}_T^{miss} calculation, and result into a large amount of fake E_T^{miss} . Dedicated algorithms have been designed to identify and reject events with anomalous E_T^{miss} , and they are consistently applied on data and simulations. In fig. 3.17 (bottom), Monte Carlo simulations (coloured histograms) are compared to data after the algorithms removing the anomalous E_T^{miss} have been applied (filled markers) and before the cleaning (open markers). The spurious high- \vec{p}_T^{miss} tail has been suppressed.

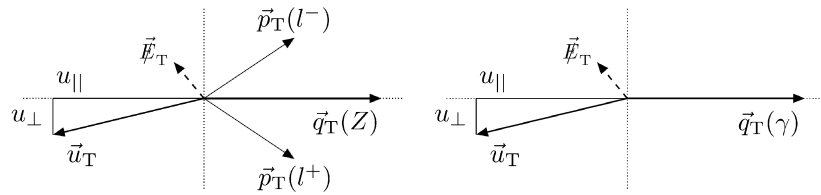


Figure 3.18: Left (Right): kinematics of $Z \rightarrow \ell\ell$ (photon) events in the (r, ϕ) plane; \vec{u}_T is the hadronic recoil, \vec{q}_T is the transverse momentum of the considered boson.

Performance of E_T^{miss} reconstruction are studied in events with a leptonic decay of a Z boson (in two muons or in two electrons) or an isolated photon. The distributions of E_T^{miss} are showed in top fig. 3.19, separately for the three event categories. The hadronic recoil \vec{u}_T is defined as the vectorial sum of all the particles, except the momentum \vec{q}_T of the vector boson considered (Z or γ). From the momentum conservations, the following relation holds:

$$\vec{q}_T + \vec{p}_T^{\text{miss}} + \vec{u}_T = 0. \quad (3.12)$$

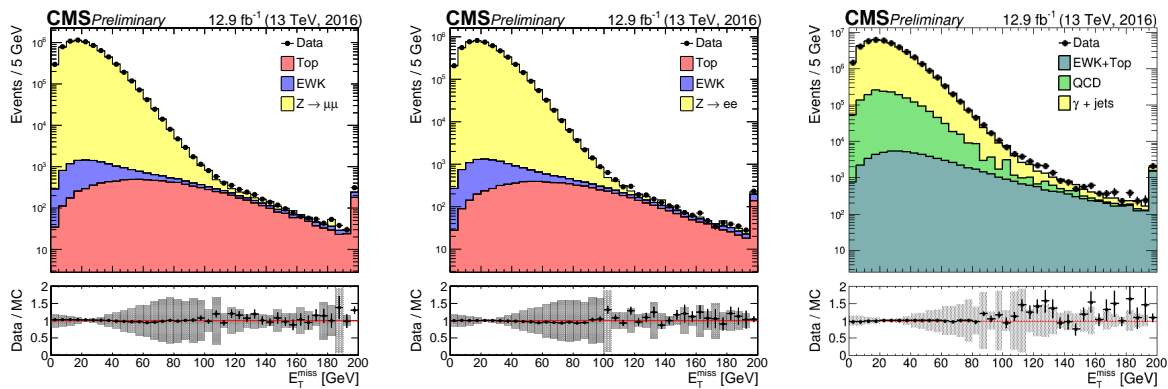


Figure 3.19: Data (black markers) and Monte Carlo (histograms) distributions of E_T^{miss} variable, in events reconstructing respectively a $Z \rightarrow \mu\mu$ decay (left), a $Z \rightarrow ee$ decay (center), an isolated photon (right).

The two components of the hadronic recoil, $u_{||}$ and u_{\perp} , along with the vectors described in eq.3.12, are schematically represented in fig. 3.18.

973 The E_T^{miss} response, defined as $-\langle u_{||} \rangle / \langle q_T \rangle$, is calculated as a function of q_T in data and simulations
 974 (fig. 3.20, left). The distributions of the two components of the hadronic recoil, $u_{||} + q_T$ and u_{\perp} ,
 975 are modelled as Voigtian functions (the convolution of a Gaussian with a Breit-Wigner). The E_T^{miss}
 976 resolution of each component is calculated as the full width at half maximum of the corresponding
 977 Voigtian, and it is displayed in fig. 3.20 (center and right plots), as a function of q_T .

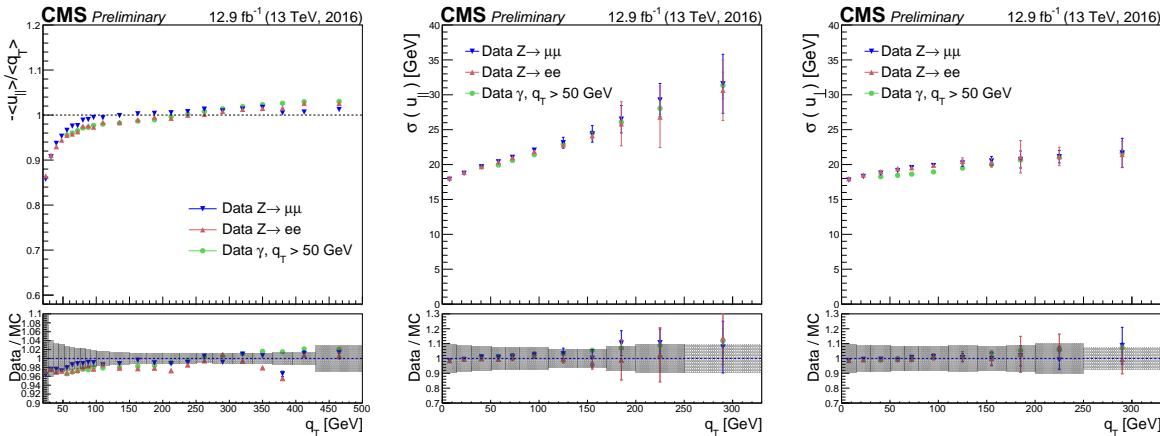


Figure 3.20: Top plots – Left: E_T^{miss} response, as a function of the transverse momentum q_T of the vector boson considered in the event (Z decaying in $\mu\mu$, Z in ee or a photon), measured on data. Center and right: resolution on the measurement of the parallel and perpendicular hadronic recoil in data, as a function of q_T . Bottom plots: data and simulation ratio of the corresponding measured variables.

978 3.3 ATLAS, ALICE, LHCb detectors

979 3.3.1 ATLAS

980 ATLAS (A Toroidal LHC ApparatuS) is a multi-purpose experiment, that shares the same scientifical
 981 aims of CMS. The simultaneous observation of an Higgs boson-like particle at the two experimental
 982 facilities represented an irrefutable proof of the discovery of the Higgs boson.
 983 ATLAS has a cylindrical shape (diameter of 25 m, length of 46 m) and weights 7000 tons. Like CMS,
 984 ATLAS is composed by many sub-detectors: trackers, calorimeters and muon system. The ATLAS
 985 magnetic field is provided by a solenoid, located inside the cylinder, and a big toroid, located outside
 986 the sub-detectors, able to reach a magnetic field of 2 T at the interaction point. The main differences
 987 among the two experiments are listed below.

- *Tracker* – the CMS tracker has a better p_T resolution (mainly due to the higher magnetic field): $\sigma_{p_T} / p_T \approx 5 \cdot 10^{-4} p_T + 0.01$ at ATLAS; $\sigma_{p_T} / p_T \approx 1.5 \cdot 10^{-4} p_T + 0.005$ at CMS.
- *Electromagnetic calorimeter* – the CMS electromagnetic calorimeter is completely enclosed inside the solenoid, whilst ATLAS calorimeter is outside of the solenoid. The particles going through the solenoid suffer an energy loss and a consequent deterioration of the energy resolution. The CMS ECAL has an energy resolution of $\sigma_E / E \approx 3\% / \sqrt{E}$; the ATLAS calorimeter has a sandwich structure (liquid argon and lead layers) and a resolution of $\sigma_E / E \approx 10\% / \sqrt{E}$.
- *Hadronic calorimeter* – the CMS HCAL is partly inside the solenoid, partly outside, degrading the resolution. The ATLAS hadronic calorimeter (made of iron and plastic scintillator

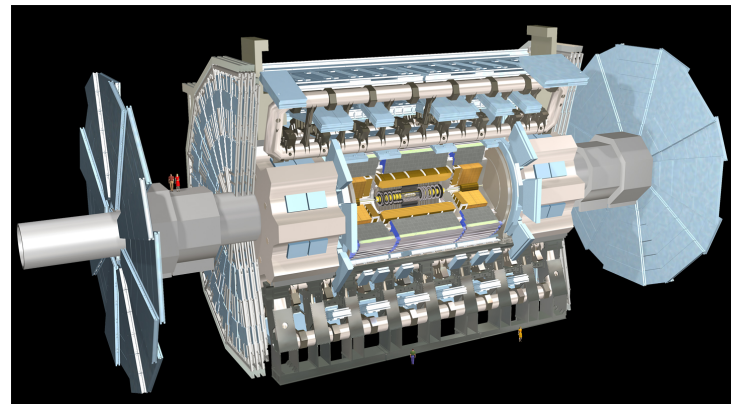


Figure 3.21: The ATLAS experiment.

997 tiles) has an energy resolution $\sigma_E/E \approx 50\%/\sqrt{E} + 0.03$ GeV; CMS HCAL has a resolution of
998 $\sigma_E/E \approx 100\%/\sqrt{E} + 0.05$ GeV.

- 999 • *Muon system* – the peculiar geometry of the ATLAS muon system allows a better resolution of
1000 the standalone measurement of the muon momenta (*i.e.*, without using tracker and calorime-
1001 ters), that is around 10% at 1 TeV. CMS has better performance when combining the informa-
1002 tions coming from the inner detectors (7% at 1 TeV against the 35% for the standalone mea-
1003 surement).

1004 3.3.2 ALICE

1005 ALICE (A Large Ion Collider Experiment) studies the heavy ion collisions (lead-lead) or proton-ion
1006 in order to explore the physics of the hadrons in high density (or temperature) regimes, when a new
1007 state of matter appears, the so-called quark-gluon plasma (QGP). The QGP played a crucial role in
1008 the very first instants of life of the universe.

1009 3.3.3 LHCb

1010 LHCb (Large Hadron Collider beauty) is a detector designed to study the b quark properties, in par-
1011 ticular the CP violation and other rare phenomena involved in b hadrons. The final aim of these
1012 measurements is trying to solve the matter-antimatter asymmetry problem.

1013 The three detectors are depicted in fig. 3.21–3.23.

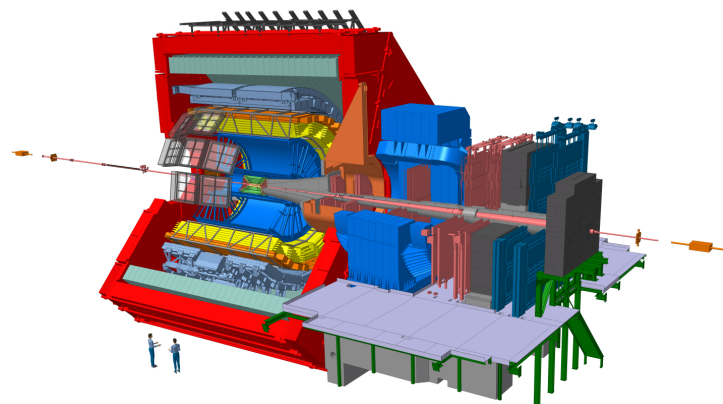


Figure 3.22: The ALICE experiment.

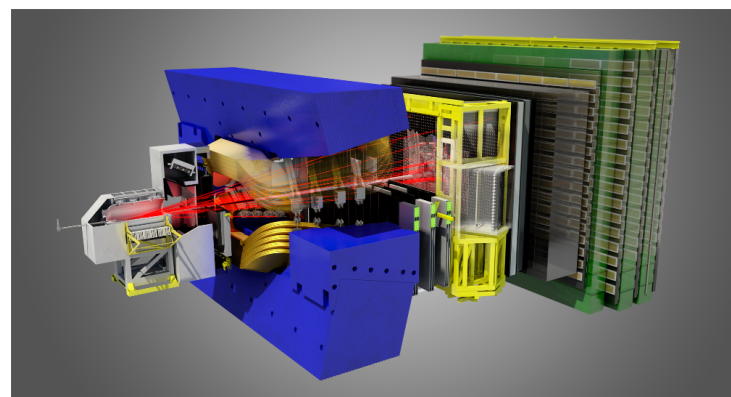


Figure 3.23: The LHCb experiment.

Search for diboson resonances in the $ZV \rightarrow \nu\bar{\nu}q\bar{q}$ final state

1015

1016

1017 Brief intro to the analysis

1018 **4.1 Data and Monte Carlo samples**

4.2 Event selection

4.2 Event selection

In this section, a list of the physics objects used in the analysis is presented, together with performance and validation plots.

The objects are selected according to the standard Run2 recommendations provided by the various POGs for the Summer16 (25ns) MiniAOD-v2 (Moriond recommendations).

The version of CMSSW used for the analysis is CMSSW_8_0_25.

4.2.1 Vertex and Pile-up

How the vertices and pile-up are reconstructed

Due to pileup several primary vertices are typically reconstructed in an event. The primary vertex of the event is defined as the one with the highest sum of transverse momenta $\sum p_T^2$ of clustered physics objects associated to it, which passes the following selections:

- number of degrees of freedom $N_{DoF} > 4$
- vertex position along the beampipe $|z_{vtx}| < 24\text{cm}$
- vertex distance with respect the beam pipe $d_0 < 2\text{cm}$

where z_{vtx} and d_0 are the distance along and perpendicular to the beam line of the vertex with respect the nominal interaction point $(0, 0, 0)$.

The data sample contains a significant number of additional interactions per bunch crossing, an effect known as pileup (PU).

The Summer16 v2 MINIAOD Monte Carlo samples are generated simulating the PU conditions, using the 25ns asymptotic PU scenario. Nevertheless, the MC PU description does not match exactly the conditions in data, and there is therefore the need to reweight the simulated events in order to improve the agreement with the data.

The MC samples are reweighted using the standard CMS PU reweighting technique [66, 67] assuming a total inelastic cross section of $\sigma_{in} = 69\,200\mu b$.

The comparison between the distributions of primary vertices in data and MC after the PU reweighting is applied is shown in Figure 4.1 for an event selection (called inclusive selection) requiring large amount of \vec{p}_T^{miss} recoiling against an AK8 fat jet (Tab. ??).

Figure 4.1: Primary vertices distributions after reweighting with the official recipe and $\sigma_{in} = 69\,200\mu b$.

4.2.2 Electrons

How the electrons are reconstructed: The electron identification variables that have been found to be the most powerful, and are used in the selection, are: the energy-momentum match between the seed cluster and the trackE seed/pin, the variables measuring spatial matching between the track and the supercluster, in and in, the supercluster width, i i(as taken from the covariance matrix using logarithmic weights), and the hadronic leakage variable H/E. The supercluster width is to a very good approximation unaffected by the spreading due to the magnetic field of the showering in the tracker material.

Isolation variables are computed in three sub-detectors: the tracker, the ECAL, and the HCAL. Transverse energy/momentun sums are evaluated in regions of $R < 0.3$. As electrons undergo bremsstrahlung

1056 energy loss in the tracker material, care is taken to remove from the isolation sums the contributions
 1057 from bremsstrahlung photons and possible resulting conversion electrons.

1058 Electrons are reconstructed from energy deposits in the ECAL matched to tracks reconstructed
 1059 in the silicon tracker. The electron trajectories are reconstructed using a dedicated modeling of the
 1060 electron energy loss and fitted with a Gaussian sum filter. Electrons used in this analysis are required
 1061 to pass the Particle Flow criteria, and to fall in the ECAL pseudorapidity fiducial range ($|\eta| < 2.5$).

1062 The electron identification used in this analysis is based on the “cut-based” Id defined by the
 1063 EGamma POG for the Summer16 25ns [68], and suggested also for the usage in 80X for the so-called
 1064 Moriond dataset. Isolation cuts are already applied within the cut-based Id definitions, therefore
 1065 no additional Isolation cut is required. In the isolation definition the effect of PU is considered by
 1066 taking into account the energy deposits in the calorimeter, estimated through the so-called ρ -area
 1067 method, by subtracting the median energy density in the event ρ multiplied by electron effective
 1068 area. The isolation value is computed in a ΔR cone of 0.3 centered along the lepton direction.

1069 Since in this analysis we are aiming at a final state without any lepton, every electron identified
 1070 with *veto* cut-based Id, transverse momentum $p_T > 10$ GeV is vetoed. The detailed set of cuts to
 1071 define a *veto* cut-based Id electron are reported in the Table 4.1.

	Electrons	Veto	
		EB	EE
$\sigma_{i\eta i\eta}$	<	0.0115	0.037
$\Delta\eta_{in}^{seed}$	<	0.00749	0.00895
$\Delta\varphi_{in}$	<	0.228	0.213
H/E	<	0.356	0.211
relIso (EA)	<	0.175	0.159
$ 1/E - 1/p $	<	0.299	0.15
$ d_0 $	<	0.05	0.10
$ d_z $	<	0.10	0.20
missing hits	\leq	2	3
conversion veto	yes	yes	yes

Table 4.1: Summer16 cut-based selection for 25ns conditions. EB: barrel cuts ($|\eta_{supercluster}| \leq 1.479$); EE: endcap cuts ($|\eta_{supercluster}| > 1.479$)

1072 Scale factors for electron identification (including isolation) are provided by Egamma POG, de-
 1073 rived for 80X (Moriond 17 recommendation), that can be found in [69].

1074 4.2.3 Muons

1075 How the muons are reconstructed

1076 In the standard CMS reconstruction for pp collisions, muon tracks are first reconstructed in-
 1077 dependently in the inner tracker (tracker track) and in the muon system (standalone-muon track).
 1078 Based on these objects, two reconstruction approaches are used [70]: *Global Muon* (outside-in) and
 1079 *Tracker Muon* (inside-out).

1080 *reconstruction (outside-in)*: for each standalone-muon track, a matching tracker track is found by comparing parame-
 1081 ters of the two tracks propagated onto a common surface, and a global-muon track is fitted
 1082 combining hits from the tracker track and standalone-muon track, using the Kalman-filter
 1083 technique [71]. At large transverse momenta, $p_T > 200$ GeV, the global-muon fit can improve
 1084 the momentum resolution compared to the tracker-only fit.

4.2 Event selection

reconstruction (*inside-out*): in this approach, all tracker tracks with $p_T > 0.5\text{GeV}$ and the total momentum $p > 2.5\text{GeV}$ are considered as possible muon candidates and are extrapolated to the muon system taking into account the magnetic field, the average expected energy losses, and multiple scattering in the detector material. If at least one muon segment (i.e., a short track stub made of DT or CSC hits) matches the extrapolated track, the corresponding tracker track qualifies as a Tracker Muon.

Tracker Muon reconstruction is more efficient than the Global Muon reconstruction at low momenta, $p_T \lesssim 5\text{GeV}$, because it requires only a single muon segment in the muon system, whereas Global Muon reconstruction is designed to have high efficiency for muons penetrating through more than one muon station and typically requires segments in at least two muon stations. Thanks to the high tracker-track efficiency and a very high efficiency of reconstructing segments in the muon system, about 99% of muons produced in pp collisions and having sufficiently high momentum are reconstructed either as a Global Muon or a Tracker Muon, and very often as both. Muons reconstructed only as standalone-muon tracks have worse momentum resolution and less favorable collision muon to cosmic-ray muon ratio than the Global and Tracker Muons and are usually not used in physics analyses.

Muons are usually based on the *Particle Flow Muon* selection, considering Global Muon or a Tracker Muon candidates and by applying minimal requirements on the track components in the muon system and taking into account a matching with small energy deposits in the calorimeters.

For muons reconstructed using the PF algorithm, the standard muon isolation is defined as the ratio of the p_T sum of all charged and neutral particle-flow candidates in the event within a cone with a radius of $\Delta R = 0.4$ centered along the lepton direction. Corrections in order to reduce the PU contamination are also applied, using the $\Delta\beta$ method. Charged candidates falling into the cone that are not compatible with the primary vertex are removed from the sum. Additionally, the neutral contribution from PU is estimated to be half the one coming from charged candidates, and this quantity is also subtracted from the total. Eventually, the scalar sum is divided by the lepton p_T itself. The general formula for the standard *particle-flow* isolation is then:

$$I_{rel} = \left[\sum p_T^{\text{ch had}} + \max\left(\sum p_T^{\text{neu had}} + \sum p_T^\gamma - 0.5 \cdot \sum p_T^{\text{pu ch had}}, 0\right) \right] / p_T^\ell$$

where $\sum p_T^{\text{ch had}}$ is the sum of the transverse momenta of the charged hadrons, $\sum p_T^{\text{neu had}}$ is the sum of transverse energies of the neutral hadrons, p_T^γ is the sum of the transverse energy of particle flow photons and $\sum p_T^{\text{pu ch had}}$ is the sum of transverse momenta of the charged particles in the cone of interest but with particles not originating from the primary vertex (for pileup corrections).

In the VZ event selection, all muons identified with the Loose standard id, p_T over 10 GeV, PF isolation below 0.25, $\eta < |\mathbf{2.4}|$ are vetoed.

Scale factors for muon identification and isolation are centrally provided as a function of the muon p_T and η by the Muon POG [72], and are applied consistently in the analysis.

4.2.4 Taus

How the taus are reconstructed

The presence of hadronically-decaying taus only act as veto for the events both in the signal and in the control regions to suppress electroweak backgrounds. The selection criteria for taus are $p_T > 18\text{ GeV}$ and $|\eta| < 2.3$. The Run2 TauPOG recommended identification criteria [73] (`decayModeFinding_byLooseCombinedIsolationDeltaBetaCorr3Hits`) are required and applied in order to identify possible tau candidates.

4.2.5 Photons

How the photons are reconstructed

As in the case of tau leptons, a photon veto is applied in the analysis both for the signal and the control regions. Events are rejected if they contains one (or more) photon with $p_T > 15$ GeV, $|\eta| < 2.5$, passing the Loose cut-based photon ID. The Loose photon Id is applied as in the EGamma POG recommandations for Run2 analyses [74] (tuned on Spring16 25 ns samples). The isolation cuts (using the rho-area method for the mitigation of the pileup) and conversion safe electron veto are applied. The isolation value is computed in a ΔR cone of 0.3 and is corrected for pileup by subtracting the event-by-event energy density (ρ) times an effective area. The applied cut-based definition of the Loose photon Id is reported in Table 4.2.

Photons	Loose	
	EB	EE
H/E	<	0.0597
$\sigma_{i\eta i\eta}$	<	0.01031
PF ch.had.iso.(ρ -corr)	<	1.295
PF neu.had.iso.(ρ -corr)	<	$10.910 + 0.0148p_T + 0.000017p_T^2$
PF photon iso.(ρ -corr)	<	$5.931 + 0.0163p_T + 0.000014p_T^2$
conversion veto	yes	$3.630 + 0.0047p_T$
		$6.641 + 0.0034p_T$
		yes

Table 4.2: Photon cut-based Id for Spring16 25ns conditions. EB: barrel cuts ($|\eta_{\text{supercluster}}| \leq 1.479$); EE: endcap cuts ($|\eta_{\text{supercluster}}| > 1.479$)

Scale factors for photon identification (including isolation) are provided by Egamma POG, derived for 80X (Moriond 17 recommendation), that can be found in [69].

4.2 Event selection

4.2.6 Jets

How the jets are reconstructed

The latest jet energy corrections are applied to AK4 and AK8 CHS jets, and the tags are Summer16 23Sep2016V3.

In this analysis, jets are considered if the corrected p_T is larger than 30 GeV for AK4 jets and 200GeV for AK8 jets, and lie in the tracker acceptance ($|\eta| < 2.4$). Additionally, AK4 are required to pass *loose* jet identification requirements, AK8 are required to pass *tight* jet identification requirements defined by the JETMET POG for Run2 analyses [75], listed in Table 4.3. AK8 jets are used to reconstruct the hadronically decaying electroweak boson candidate, whilst AK4 jets are used to suppress the contribution of top and QCD background events.

EFFICIENZA di TIGHT ID?

Figure 4.2- 4.4 show the data/simulation comparison after the analysis selections (Tab. ?? without Top cleaning and Event cleaning).

PF Jet ID	loose	tight
Neutral Hadron Fraction	< 0.99	< 0.90
Neutral EM Fraction	< 0.99	< 0.90
Number of Constituents	> 1	> 1
Muon Fraction	-	-
Additionally, for $ \eta < 2.4$		
Charged Hadron Fraction	> 0	> 0
Charged Multiplicity	> 0	> 0
Charged EM Fraction	< 0.99	< 0.99

Table 4.3: *Loose* and *Tight* jet identification requirements for Run2 (Spring16) 25ns conditions.

Figure 4.2: Number of reconstructed AK8 jets after selections.

Figure 4.3: Leading AK8 jet p_T spectra after selections.

Figure 4.4: Leading AK8 jet η spectra after selections.

Since it has been measured that the jet energy resolution (JER) is not the same in data and MC, an additional smearing is applied in simulation, in order to get a better agreement, as suggested by JETMET POG [76].

There are two independent ways to get the smearing. With the scaling method, corrected four-momentum of a reconstructed jet is rescaled with a factor

$$c_{\text{JER}} = 1 + (s_{\text{JER}} - 1) \frac{p_T - p_T^{\text{ptcl}}}{p_T},$$

where p_T is its transverse momentum, p_T^{ptcl} is the transverse momentum of the corresponding jet clustered from generator-level particles, and s_{JER} is the data-to-simulation core resolution scale factor. Factor c_{JER} is truncated at zero, i.e. if it is negative, it is set to zero. This method only works if a well-matched particle-level jet is present and can result in a large shift of the response otherwise. The following requirements are imposed for the matching:

$$\Delta R < R_{\text{cone}}/2, |p_T - p_T^{\text{ptcl}}| < 3\sigma_{\text{JER}}p_T.$$

- 1149 Here R_{cone} is the jet cone size parameter (for instance, 0.4 for AK4 jets) and σ_{JER} is the relative p_T
1150 resolution as measured in simulation.

An alternative approach, which does not require the presence of a matching particle-level jet, is the stochastic smearing. In this case corrected jet four-momentum is rescaled with a factor

$$c_{\text{JER}} = 1 + \mathcal{N}(0, \sigma_{\text{JER}})\sqrt{\max(s_{\text{JER}}^2 - 1, 0)},$$

- 1151 where σ_{JER} and s_{JER} are the relative p_T resolution in simulation and data-to-simulation scale factors,
1152 and $\mathcal{N}(0, \sigma)$ denotes a random number sampled from a normal distribution with a zero mean and
1153 variance σ^2 . As before, scaling factor c_{JER} is truncated at zero. This method only allows to degrade
1154 the resolution.

- 1155 The smearing procedure adopted in this analysis is the hybrid method: when matching particle-
1156 level jet is found, the scaling method is used; otherwise the stochastic smearing is applied. The
1157 smearing coefficients and their errors, provided by JETMET POG, are reported in Tab. 4.4 for 2016
1158 data (tag: Spring1625nsV10).

Jet η	SF
0.0–0.5	1.109 ± 0.008
0.5–0.8	1.138 ± 0.013
0.8–1.1	1.114 ± 0.013
1.1–1.3	1.123 ± 0.024
1.3–1.7	1.084 ± 0.011
1.7–1.9	1.084 ± 0.011
1.9–2.1	1.140 ± 0.047
2.1–2.3	1.067 ± 0.053
2.3–2.5	1.177 ± 0.041
2.5–2.8	1.364 ± 0.039
2.8–3.0	1.857 ± 0.071
3.0–3.2	1.328 ± 0.022
3.2–5.0	1.16 ± 0.029

Table 4.4: Smearing coefficients and JER uncertainties.

4.2 Event selection

4.2.7 Jet mass

The jet mass is the main observable in distinguishing a V-jet from a QCD jet. Jet grooming consists in the suppression of uncorrelated UE/PU (underlying event and pile-up) radiation from the target jet and improves the discrimination pushing the jet mass for QCD jets towards lower values while maintaining the jet mass for V-jets around the boson-mass.

The grooming algorithm considered in this analysis is the following:

Soft-drop: The “soft drop declustering” is a jet substructure technique which recursively removes soft wide-angle radiation from a jet [77]. The soft drop algorithm depends on two parameters: a soft threshold z_{cut} and an angular exponent β . Like any grooming method, soft drop declustering removes wide-angle soft radiation from a jet in order to mitigate the effects of contamination from initial state radiation (ISR), underlying event (UE), and multiple hadron scattering (pileup). Given a jet of radius R_0 with only two constituents, the soft drop procedure removes the softer constituent unless:

$$\frac{\min(p_T^1, p_T^2)}{p_T^1 + p_T^2} > z_{cut} \left(\frac{\Delta R_{12}}{R_0} \right)^\beta$$

By construction, this condition fail for wide-angle soft radiation. The degree of jet grooming is controlled by z_{cut} and β , with $\beta \rightarrow \infty$ returning back an ungroomed jet. The $\beta = 0$ limit of the energy loss is particularly interesting, since it is largely insensitive to the value of the strong coupling constant. The default parameters used by CMS are $\beta = 0$ and $z_{cut} = 0.1$.

The grooming algorithm, **soft-drop**, is used in association with **PUPPI** in order to remove soft and wide-angle radiations and the pile-up contribution. It is a shared choice among all the diboson analyses, praised by theoreticians.

Unfortunately, the default soft-drop + PUPPI jet mass suffers from a systematic shift from the expected value of about $\sim 10\%$, and some residual dependence on the jet p_T . Further corrections to the jet mass have been applied:

Gen: a p_T -dependent correction to account for a small shift in the generated vector boson mass, applied only on simulated samples

Reco: a p_T -dependent correction to the reconstructed jet mass, applied separately for jets in the barrel and endcaps regions

These corrections are evaluated centrally by JMAR and documented in [78], and applied accordingly within the analysis.

Figure 4.6- 4.7 show the jet mass for W or Z bosons before and after the correction, without applying any cut on this variable.

Figure 4.5: Softdrop + PUPPI mass of AK8 jet reconstructed for different bulk graviton signal samples; left: before corrections. right: after corrections.

Furthermore, in order to obtain a better data-Monte Carlo agreement, a smearing procedure has been applied to the puppi softdrop mass, by using the stochastic method, with a constant smearing coefficient provided by JETMET POG (1.00 ± 0.20), that does not depend on jet pseudorapidity if it is restricted to $|\eta| < 2.5$.

Figure 4.6: Softdrop + PUPPI mass of AK8 jet reconstructed for different W' signal samples; left: before corrections. right: after corrections.

Figure 4.7: Softdrop + PUPPI mass of AK8 jet; left: before corrections. right: after corrections.

1187 4.2.8 Jet substructure

In order to further discriminate signal from background, it is useful to investigate the inner structure of the jet. Studying the distribution of the jet constituents with respect to the jet axis allows us to test the hypothesis of the existence of multiple substructures, that could be evidence of jets originated by more than one parton. This procedure proceeds as follows: the constituents of the jet are clustered again with the k_T algorithm, however the procedure is stopped when one obtains N subjets. Then, a new variable, the N-subjettiness, is introduced. It is defined as:

$$\tau_N = \frac{1}{d_0} \sum_k p_{T,k} \min(\Delta R_{1,k}^\beta, \Delta R_{2,k}^\beta, \dots, \Delta R_{N,k}^\beta)$$

1188 where β is an arbitrary parameter, the index k runs over the jet constituents and the distances $\Delta R_{N,k}$
 1189 are calculated with respect to the axis of the N-th subjet, obtained by one iteration of τ minimization
 1190 by varying the subjet axes around the k_T subjet axes.

The normalization factor d_0 is calculated as $d_0 = \sum_k p_{T,k} R_0^\beta$, setting R_0 to the radius of the original jet. The N-subjettiness is always included in the interval from 0 to 1 and represents the compatibility of the jet structure with an N-subjet hypothesis: small values correspond to high compatibility. Indeed, τ_N weights the transverse momentum of the jet constituents by their angular distance to the closest subjet. In this analysis the N-subjettiness is calculated from the ungroomed jet with the parameter $\beta = 1$. The subjettiness related to the one and two subjet hypothesis is thus:

$$\tau_1 = \frac{1}{d_0} \sum_k p_{T,k} \Delta R_{1,k}$$

and

$$\tau_2 = \frac{1}{d_0} \sum_k p_{T,k} \min(\Delta R_{1,k}, \Delta R_{2,k})$$

1191 In principle, these two quantities should allow us to distinguish the dipole-like nature of the showering of the Higgs decay from the classic monopole structure of QCD jets. In particular, the variable
 1192 that best discriminates between V-jets and QCD jets is the ratio of 2-subjettiness and 1-subjettiness,
 1193 $\tau_{21} = \tau_2 / \tau_1$.

1194 Figure 4.8 shows the τ_{21} distributions for the PUPPI algorithm.

Figure 4.8: τ_{21} subjettiness of PUPPI AK8 jet after inclusive selections.

1196 4.2.9 b-tagging

1197 B-tagging algorithms are applied to both the fat-jet and the sub-jets, independently. For subjets,
 1198 run-II taggers are by default applied on the same charged particle-flow candidate list that is used

4.2 Event selection

1199 in the jet clustering (*explicit jet-to-track association*). Thanks to the explicit jet-to-track association,
1200 the two sub-jets do not share any PF-constituent, avoiding unintended correlations.

1201 The jet or sub-jet is considered as tagged if the discriminator value is above some threshold
1202 value, often referred to as the cut value, and the efficiency is defined as the number of jets which
1203 have a discriminator value that is above that cut divided by the total number of jets (of the same
1204 flavor).

1205 The b-tagging algorithm used to set the analysis strategy is the Combined Secondary Vertex
1206 (CSV) [79] discriminator (full name `pfCombinedInclusiveSecondaryVertexV2BJetTags`). Dif-
1207 ferent working points are provided by the POG for Run2 analyses [80], as shown in table 4.2.9, but
1208 the only one used in this analysis is the *loose* working point.

Working point	CSV cut	mis-tag probability
CSVL (Loose)	> 0.5426	≈ 10%
CSVM (Medium)	> 0.8484	≈ 1%
CSVT (Tight)	> 0.9535	≈ 0.1%

Table 4.5: Working point for CSV b-tagging algorithm.

1209 B-tagging efficiency is not the same in data and MC. In order to take into account this difference,
1210 the BTV POG provides collections of b-tagging scale factors for b-jets and mistagged light jets, mea-
1211 sured for different physics processes, for the supported tagging algorithms and the three standard
1212 working points [79]. A weight is calculated on a per-event basis as a function of the b-tagging status
1213 of the jets and their kinematic variables [81].

1214 In this analysis, b-tagging is used in order to reject events where a top quark is involved, by
1215 asking to the AK4 jets not laying in the AK8 jet cone to be anti b-tagged (in practice, the maximum
1216 CSV value allowed is the loose working point, CSVL).

1217 4.2.10 Missing Energy

1218 How the MET is reconstructed

1219 The E_T^{miss} is the imbalance in the transverse momentum of all visible particles, and it is recon-
1220 structed with the particle flow algorithm [82]. The *raw* E_T^{miss} is defined as the inverse vectorial sum
1221 of the transverse momentum of all the reconstructed charged and neutral particle flow candidates:
1222 $E_T^{\text{miss}} = -\sum_{i=0}^{\text{all}} \vec{p}_{T,i}$. The raw E_T^{miss} is systematically different from true E_T^{miss} , for many reasons in-
1223 cluding the non-compensating nature of the calorimeters and detector misalignment. To better
1224 estimate the true E_T^{miss} , corrections can be applied:

1225 *Type-0*: a mitigation for the degradation of the E_T^{miss} reconstruction due to the pileup interactions, by
1226 applying the CHS algorithm. However, the E_T^{miss} contribution from pileup neutral particles
1227 cannot be easily subtracted; the assumption is that the E_T^{miss} contribution term of charged and
1228 neutral pileup particles are the same, and cancellation at the true level is exact: $\sum_{\text{neuPU}} \vec{p}_{T,i}^{\text{true}} +$
1229 $\sum_{\text{chPU}} \vec{p}_{T,i}^{\text{true}} = 0$. An additional E_T^{miss} term is then added to the raw E_T^{miss} to take into ac-
1230 count the neutral PU contribution, which is equal to the charged one with a multiplicative
1231 scale factor taking into account calorimeter mismeasurements of low- p_T energy deposits.

1232 *Type-1*: propagation of the jet energy corrections (JEC) to MET. The Type-I correction replaces the
1233 vector sum of transverse momenta of particles which can be clustered as jets with the vector
1234 sum of the transverse momenta of the jets to which JEC is applied.

1235 Particle flow E_T^{miss} with type-1 corrections applied is currently the default one used by CMS physics
1236 analyses. Additionally, some E_T^{miss} filters have been recommended by JETMET POG for Run2 analy-

1237 ses [75], in order to remove events with spurious E_T^{miss} related to detector noise and bad reconstructions,
 1238 and they are listed in sec. ??.

1239 Since the E_T^{miss} corrections and uncertainties depend on the JEC applied, they are re-computed
 1240 accordingly following the JETMETPOG recommendation:

```
1241 from PhysicsTools.PatUtils.tools.runMETCorrectionsAndUncertainties import
1242 runMetCorAndUncFromMiniAOD
1243 # If you only want to re-correct and get the proper uncertainties
1244 runMetCorAndUncFromMiniAOD(process,
1245                         isData=True (or False),
1246                         )
1247 process.p = cms.Path(process.fullPatMetSequence *
1248                     process.yourAnalyzer)
1249
1250 cms.InputTag("slimmedMETS","","YourProcessName")
```

1251 Figure 4.9 show the E_T^{miss} distribution for data and Monte Carlo after the corrections and filters.

Figure 4.9: Type-1 corrected E_T^{miss} distribution after inclusive selections.

1252 **4.3 Diboson candidate reconstruction**

₁₂₅₃ **4.4 Background estimation**

4.5 Systematic uncertainties

1254 4.5 Systematic uncertainties

₁₂₅₅ **4.6 Results**

Combination of diboson searches in semileptonic final states

Conclusions

1260

1261

1262

Bibliography

1263

1264

- 1265 [1] ATLAS Collaboration, “Observation of a new particle in the search for the Standard Model Higgs
1266 boson with the ATLAS detector at the LHC,” *Phys. Lett. B*, vol. 716, p. 1, 2012.
- 1267 [2] CMS Collaboration, “Observation of a new boson at a mass of 125 GeV with the CMS experi-
1268 ment at the LHC,” *Phys. Lett. B*, vol. 716, p. 30, 2012.
- 1269 [3] CMS Collaboration, “Observation of a new boson with mass near 125 GeV in pp collisions at
1270 $\sqrt{s} = 7$ and 8 TeV,” *JHEP*, vol. 06, p. 081, 2013.
- 1271 [4] ATLAS Collaboration, “Evidence for the spin-0 nature of the Higgs boson using ATLAS data,”
1272 *Phys. Lett. B*, vol. 726, p. 120, 2013.
- 1273 [5] CMS Collaboration, “Precise determination of the mass of the Higgs boson and tests of com-
1274 patibility of its couplings with the standard model predictions using proton collisions at 7 and
1275 8 TeV,” *Eur. Phys. J. C*, vol. 75, p. 212, 2015.
- 1276 [6] ATLAS Collaboration, “Measurement of the Higgs boson mass from the $H \rightarrow \gamma\gamma$ and $H \rightarrow$
1277 $ZZ^* \rightarrow 4\ell$ channels in pp collisions at center-of-mass energies of 7 and 8 TeV with the ATLAS
1278 detector,” *Phys. Rev. D*, vol. 90, p. 052004, 2014.
- 1279 [7] CMS and ATLAS Collaborations, “Combined Measurement of the Higgs Boson Mass in pp Col-
1280 lisions at $\sqrt{s} = 7$ and 8 TeV with the ATLAS and CMS Experiments.” Submitted to *Phys. Rev. Lett.*,
1281 2015.
- 1282 [8] G. Degrassi, S. Di Vita, J. Elias-Miro, J. R. Espinosa, G. F. Giudice, G. Isidori, and A. Strumia,
1283 “Higgs mass and vacuum stability in the Standard Model at NNLO,” *JHEP*, vol. 08, p. 098, 2012.
- 1284 [9] D. Pappadopulo, A. Thamm, R. Torre, and A. Wulzer, “Heavy vector triplets: bridging theory
1285 and data,” *Journal of High Energy Physics*, vol. 2014, no. 9, pp. 1–50, 2014.
- 1286 [10] V. D. Barger, W.-Y. Keung, and E. Ma, “A Gauge Model With Light W and Z Bosons,” *Phys. Rev.*,
1287 vol. D22, p. 727, 1980.
- 1288 [11] C. Grojean, E. Salvioni, and R. Torre, “A weakly constrained W' at the early LHC,” *JHEP*, vol. 07,
1289 p. 002, 2011.

- 1290 [12] R. Contino, D. Pappadopulo, D. Marzocca, and R. Rattazzi, “On the effect of resonances in com-
1291 posite higgs phenomenology,” *Journal of High Energy Physics*, vol. 2011, no. 10, pp. 1–50, 2011.
- 1292 [13] B. Bellazzini, C. Csáki, and J. Serra, “Composite Higgses,” *Eur. Phys. J.*, vol. C74, no. 5, p. 2766,
1293 2014.
- 1294 [14] G. F. Giudice, C. Grojean, A. Pomarol, and R. Rattazzi, “The Strongly-Interacting Light Higgs,”
1295 *JHEP*, vol. 06, p. 045, 2007.
- 1296 [15] A. Wulzer, “An Equivalent Gauge and the Equivalence Theorem,” *Nucl. Phys.*, vol. B885,
1297 pp. 97–126, 2014.
- 1298 [16] A. M. Sirunyan *et al.*, “Search for massive resonances decaying into WW, WZ, ZZ, qW, and qZ
1299 with dijet final states at $\sqrt{s} = 13$ TeV,” 2017.
- 1300 [17] CMS Collaboration, “Search for massive resonances decaying into WW, WZ, ZZ, qW and qZ in
1301 the dijet final state at $\sqrt{s} = 13$ TeV,” CMS Physics Analysis Summary CMS-PAS-B2G-17-001,
1302 CERN, Geneva, 2017.
- 1303 [18] CMS Collaboration, “Search for heavy resonances decaying into a vector boson and a Higgs
1304 boson in hadronic final states with 2016 data,” 2017.
- 1305 [19] CMS Collaboration, “Search for heavy resonances decaying into a vector boson and a Higgs bo-
1306 son in hadronic final states with 2016 data,” CMS Physics Analysis Summary CMS-PAS-B2G-17-
1307 002, CERN, Geneva, 2017.
- 1308 [20] CMS Collaboration, “Search for heavy resonances decaying into a Z boson and a W boson in
1309 the $\ell^+\ell^-q\bar{q}$ final state,” CMS Physics Analysis Summary CMS-PAS-B2G-16-022, CERN, Geneva,
1310 2017.
- 1311 [21] V. Khachatryan *et al.*, “Search for heavy resonances decaying into a vector boson and a Higgs
1312 boson in final states with charged leptons, neutrinos, and b quarks,” *Phys. Lett.*, vol. B768,
1313 pp. 137–162, 2017.
- 1314 [22] CMS Collaboration, “Search for new resonances decaying to $WW/WZ \rightarrow \ell\nu qq$,” CMS Physics
1315 Analysis Summary CMS-PAS-B2G-16-020, CERN, Geneva, 2016.
- 1316 [23] CMS Collaboration, “Search for heavy resonances decaying into a Z boson and a vector bo-
1317 son in the $\nu\nu q\bar{q}$ final state,” CMS Physics Analysis Summary CMS-PAS-B2G-17-005, CERN,
1318 Geneva, 2017.
- 1319 [24] M. Aaboud *et al.*, “Search for diboson resonances with boson-tagged jets in pp collisions at
1320 $\sqrt{s} = 13$ TeV with the ATLAS detector,” 2017.
- 1321 [25] ATLAS Collaboration, “Search for WW/WZ resonance production in $\ell\nu qq$ final states in pp
1322 collisions at $\sqrt{s} = 13$ TeV with the ATLAS detector,” ATLAS Conference Note ATLAS-CONF-
1323 2017-051, CERN, Geneva, Jul 2017.
- 1324 [26] ATLAS Collaboration, “Searches for heavy ZZ and ZW resonances in the llqq and vvqq final
1325 states in pp collisions at $\sqrt{s} = 13$ TeV with the ATLAS detector,” ATLAS Conference Note
1326 ATLAS-CONF-2016-082, CERN, Geneva, Aug 2016.
- 1327 [27] M. Aaboud *et al.*, “Search for heavy resonances decaying to a W or Z boson and a Higgs boson
1328 in the $q\bar{q}^{(\prime)}b\bar{b}$ final state in pp collisions at $\sqrt{s} = 13$ TeV with the ATLAS detector,” 2017.

BIBLIOGRAPHY

- 1329 [28] ATLAS Collaboration, “Search for heavy resonances decaying to a W or Z boson and a Higgs
1330 boson in final states with leptons and b -jets in 36.1 fb^{-1} of $p p$ collision data at $\sqrt{s} = 13 \text{ TeV}$
1331 with the ATLAS detector,” ATLAS Conference Note ATLAS-CONF-2017-055, CERN, Geneva, Jul
1332 2017.
- 1333 [29] L. Randall and R. Sundrum, “A Large mass hierarchy from a small extra dimension,” *Phys. Rev.*
1334 *Lett.*, vol. 83, pp. 3370–3373, 1999.
- 1335 [30] L. Randall and R. Sundrum, “An Alternative to compactification,” *Phys. Rev. Lett.*, vol. 83,
1336 pp. 4690–4693, 1999.
- 1337 [31] K. Agashe, H. Davoudiasl, G. Perez, and A. Soni, “Warped Gravitons at the LHC and Beyond,”
1338 *Phys. Rev.*, vol. D76, p. 036006, 2007.
- 1339 [32] A. L. Fitzpatrick, J. Kaplan, L. Randall, and L.-T. Wang, “Searching for the Kaluza-Klein Graviton
1340 in Bulk RS Models,” *JHEP*, vol. 09, p. 013, 2007.
- 1341 [33] H. Davoudiasl, J. L. Hewett, and T. G. Rizzo, “Phenomenology of the Randall-Sundrum Gauge
1342 Hierarchy Model,” *Phys. Rev. Lett.*, vol. 84, p. 2080, 2000.
- 1343 [34] T. Gherghetta and A. Pomarol, “Bulk fields and supersymmetry in a slice of AdS,” *Nucl. Phys.*,
1344 vol. B586, pp. 141–162, 2000.
- 1345 [35] H. Davoudiasl, J. L. Hewett, and T. G. Rizzo, “Experimental probes of localized gravity: On and
1346 off the wall,” *Phys. Rev.*, vol. D63, p. 075004, 2001.
- 1347 [36] A. Oliveira, “Gravity particles from Warped Extra Dimensions, predictions for LHC,” 2014.
- 1348 [37] CMS Collaboration, “Search for diboson resonances in the $2l2\nu$ final state,” CMS Physics Anal-
1349ysis Summary CMS-PAS-B2G-16-023, CERN, Geneva, 2017.
- 1350 [38] CMS Collaboration, “Search for heavy resonances decaying to a pair of Higgs bosons in the four
1351 b quark final state in proton-proton collisions at $\sqrt{s} = 13 \text{ TeV}$,” CMS Physics Analysis Summary
1352 CMS-PAS-B2G-16-026, CERN, Geneva, 2017.
- 1353 [39] S. Chatrchyan *et al.*, “The CMS experiment at the CERN LHC,” *JINST*, vol. 3, p. S08004, 2008.
- 1354 [40] V. Karimäki, M. Mannelli, P. Siegrist, H. Breuker, A. Caner, R. Castaldi, K. Freudenreich, G. Hall,
1355 R. Horisberger, M. Huhtinen, and A. Cattai, *The CMS tracker system project: Technical Design*
1356 *Report*. Technical Design Report CMS, Geneva: CERN, 1997.
- 1357 [41] S. Chatrchyan *et al.*, “Description and performance of track and primary-vertex reconstruction
1358 with the CMS tracker,” *JINST*, vol. 9, no. 10, p. P10009, 2014.
- 1359 [42] CMS Collaboration, *The CMS electromagnetic calorimeter project: Technical Design Report*.
1360 Technical Design Report CMS, Geneva: CERN, 1997.
- 1361 [43] CMS Collaboration, *The CMS hadron calorimeter project: Technical Design Report*. Technical
1362 Design Report CMS, Geneva: CERN, 1997. The following files are from <a href=.
- 1363 [44] CMS Collaboration, *The CMS muon project: Technical Design Report*. Technical Design Report
1364 CMS, Geneva: CERN, 1997.

- 1365 [45] CMS Collaboration, *CMS The TriDAS Project: Technical Design Report, Volume 2: Data Acquisition and High-Level Trigger. CMS trigger and data-acquisition project*. Technical Design Report
1366 CMS, Geneva: CERN, 2002.
- 1368 [46] R. Brun and F. Rademakers, “ROOT: An object oriented data analysis framework,” *Nucl. Instrum. Meth.*, vol. A389, pp. 81–86, 1997.
- 1370 [47] A. M. Sirunyan *et al.*, “Particle-flow reconstruction and global event description with the CMS
1371 detector.” Submitted to *JINST*, 2017.
- 1372 [48] R. Fruhwirth, “Application of Kalman filtering to track and vertex fitting,” *Nucl. Instrum. Meth.*,
1373 vol. A262, pp. 444–450, 1987.
- 1374 [49] K. Rose, “Deterministic annealing for clustering, compression, classification, regression, and
1375 related optimization problems,” vol. 86, pp. 2210 – 2239, 12 1998.
- 1376 [50] R. Fruhwirth, W. Waltenberger, and P. Vanlaer, “Adaptive vertex fitting,” *J. Phys.*, vol. G34,
1377 p. N343, 2007.
- 1378 [51] CMS Collaboration, “Energy Calibration and Resolution of the CMS Electromagnetic Calorimeter
1379 in $p\bar{p}$ Collisions at $\sqrt{s} = 7$ TeV,” *JINST*, vol. 8, p. P09009, 2013. [*JINST*8,9009(2013)].
- 1380 [52] W. Adam, R. Frühwirth, A. Strandlie, and T. Todor, “Reconstruction of Electrons with the
1381 Gaussian-Sum Filter in the CMS Tracker at the LHC,” 2005.
- 1382 [53] CMS Collaboration, “Performance of Electron Reconstruction and Selection with the CMS De-
1383 tector in Proton-Proton Collisions at $s = 8$ TeV,” *JINST*, vol. 10, no. 06, p. P06005, 2015.
- 1384 [54] CMS Collaboration, “Performance of Photon Reconstruction and Identification with the CMS
1385 Detector in Proton-Proton Collisions at $\text{sqrt}(s) = 8$ TeV,” *JINST*, vol. 10, no. 08, p. P08010, 2015.
- 1386 [55] S. Chatrchyan *et al.*, “Performance of CMS muon reconstruction in $p\bar{p}$ collision events at $\sqrt{s} =$
1387 7 TeV,” *JINST*, vol. 7, p. P10002, 2012.
- 1388 [56] “Performance of muon reconstruction including Alignment Position Errors for 2016 Collision
1389 Data,” Nov 2016.
- 1390 [57] CMS Collaboration, “Pileup Removal Algorithms,” Tech. Rep. CMS-PAS-JME-14-001, CERN,
1391 Geneva, 2014.
- 1392 [58] M. Cacciari, G. P. Salam, and G. Soyez, “The anti- k_t jet clustering algorithm,” *JHEP*, vol. 04,
1393 p. 063, 2008.
- 1394 [59] CMS Collaboration, “Determination of jet energy calibration and transverse momentum reso-
1395 lution in cms,” *Journal of Instrumentation*, vol. 6, no. 11, p. P11002, 2011.
- 1396 [60] S. Chatrchyan *et al.*, “Performance of tau-lepton reconstruction and identification in CMS,”
1397 *JINST*, vol. 7, p. P01001, 2012.
- 1398 [61] CMS Collaboration, “Identification of b quark jets at the CMS Experiment in the LHC Run 2,”
1399 CMS Physics Analysis Summary CMS-PAS-BTV-15-001, CERN, Geneva, 2016.
- 1400 [62] S. Chatrchyan *et al.*, “Identification of b-quark jets with the CMS experiment,” *JINST*, vol. 8,
1401 p. P04013, 2013.

BIBLIOGRAPHY

- 1402 [63] CMS Collaboration, “Performance of missing energy reconstruction in 13 TeV pp collision data
1403 using the CMS detector,” 2016.
- 1404 [64] S. Chatrchyan *et al.*, “Missing transverse energy performance of the CMS detector,” *JINST*,
1405 vol. 6, p. P09001, 2011.
- 1406 [65] CMS Collaboration, “Performance of Missing Transverse Momentum Reconstruction Algo-
1407 rithms in Proton-Proton Collisions at $p\ s = 8$ TeV with the CMS Detector,” 2012.
- 1408 [66] “Pileup Reweighting Procedure - <https://twiki.cern.ch/twiki/bin/viewauth/CMS/Pile->
1409 [upReweighting](#),”
- 1410 [67] “Utilities for Accessing Pileup Information for Data - <https://twiki.cern.ch/twik->
1411 [i/bin/view/CMS/PileupJSONFileforData](#),”
- 1412 [68] “EGamma POG - Cut based electron ID for Run2 - <https://twiki.cern.ch/twiki/bin/view/CM->
1413 [S/CutBasedElectronIdentificationRun2](#),”
- 1414 [69] “EGamma POG - Electron ID recipes for Run2 - <https://twiki.cern.ch/twiki/bin/view/CM->
1415 [S/EgammaIDRecipesRun2](#),”
- 1416 [70] CMS Collaboration, “Performance of cms muon reconstruction in pp collision events at $\sqrt{s} =$
1417 7TeV.” Submitted to *J. Inst.*, 2012.
- 1418 [71] R. Fruhwirth, “Application of kalman filtering to track and vertex fitting,” *Nuclear Instruments
1419 and Methods in Physics Research Section A: Accelerators, Spectrometers, Detectors and Associ-
1420 ated Equipment*, vol. 262, no. 23, pp. 444 – 450, 1987.
- 1421 [72] “Reference muon id, isolation and trigger efficiencies for Run-II - <https://twiki.cern.ch/twik->
1422 [i/bin/view/CMS/MuonReferenceEffsRun2](#),”
- 1423 [73] “Tau POG - Tau ID for Run2 - <https://twiki.cern.ch/twiki/bin/viewauth/CMS/TauIDRecom->
1424 [mendation13TeV](#),”
- 1425 [74] “EGamma POG - Cut based photon ID for Run2 - <https://twiki.cern.ch/twiki/bin/view/CM->
1426 [S/CutBasedPhotonIdentificationRun2](#),”
- 1427 [75] “JetMET POG - Jet ID for Run2 - <https://twiki.cern.ch/twiki/bin/view/CMS/JetID>,”
- 1428 [76] “Jetmet pog - jet energy resolution smearing - <https://twiki.cern.ch/twiki/bin/view/cms/jet->
1429 [resolution](#),”
- 1430 [77] A. J. Larkoski, S. Marzani, G. Soyez, and J. Thaler, “Soft Drop,” *JHEP*, vol. 05, p. 146, 2014.
- 1431 [78] T. K. Arrestad et al., “Identification and calibration of boosted hadronic W/Z bosons at 13 TeV,”
1432 tech. rep., AN-2016/215, 2016.
- 1433 [79] S. Chatrchyan *et al.*, “Identification of b-quark jets with the CMS experiment,” *JINST*, vol. 8,
1434 p. P04013, 2013.
- 1435 [80] “BTV POG - B-tagging for Run2 - <https://twiki.cern.ch/twiki/bin/view/CMS/BtagRecommen->
1436 [dation80X](#),”
- 1437 [81] “Methods to apply b-tagging efficiency scale factors,” 2013.
- 1438 [82] CMS Collaboration, “Particle-flow event reconstruction in CMS and performance for jets, taus,
1439 and E_T^{miss} ,” no. CMS-PAS-PFT-09-001, 2009.